

Isabela Quintela Matos

**Solvation Free Energy Calculations of  
Molecules Mimicking Asphaltenes Using The  
SAFT- $\gamma$  Mie Force Field**

Rio de Janeiro

2018

Isabela Quintela Matos

# **Solvation Free Energy Calculations of Molecules Mimicking Asphaltenes Using The SAFT- $\gamma$ Mie Force Field**

Master's thesis presented to Engenharia de Processos Químicos e Bioquímicos graduate program, Escola de Química, Universidade Federal do Rio de Janeiro, as required for obtaining a Master's degree in Chemical Engineering.

Universidade Federal do Rio de Janeiro

Escola de Química

Engenharia de Processos Químicos e Bioquímicos Graduate Program

Supervisor: Charles Rubber de Almeida Abreu

Co-supervisor: Papa Matar Ndiaye

Rio de Janeiro

2018

Isabela Quintela Matos

Solvation Free Energy Calculations of Molecules Mimicking Asphaltenes Using The SAFT- $\gamma$  Mie Force Field/ Isabela Quintela Matos. – Rio de Janeiro, 2018-

116

Supervisor: Charles Rubber de Almeida Abreu

Dissertation (Master) – Universidade Federal do Rio de Janeiro  
Escola de Química

Engenharia de Processos Químicos e Bioquímicos Graduate Program, 2018.

1. Solvation free energy. 2. Asphaltenes. 3. SAFT- $\gamma$  Mie force field.

Isabela Quintela Matos

# **Solvation Free Energy Calculations of Molecules Mimicking Asphaltenes Using The SAFT- $\gamma$ Mie Force Field**

Master's thesis presented to Engenharia de Processos Químicos e Bioquímicos graduate program, Escola de Química, Universidade Federal do Rio de Janeiro, as required for obtaining a Master's degree in Chemical Engineering.

Approved dissertation. Rio de Janeiro, February 9, 2018:

---

**Charles Rubber de Almeida Abreu**  
Supervisor

---

**Professor**  
Guest 1

---

**Professor**  
Guest 2

---

**Professor**  
Guest 3

Rio de Janeiro  
2018

# Acknowledgements

I would like to give some words of thanks to my parents for the support during the movie from Aracaju to Rio de Janeiro, and for supporting my decisions. I also would like to thank my advisers. Charles Rubber de Almeida Abreu for the elucidative meetings and for taking the time to explain in such clearly way the concepts of molecular dynamics and free energy calculations. To my co adviser Papa Matar Ndiaye, I would like to thank him for presenting the ATOMS group to me and for accepting my participation in his project about asphaltenes. I also would like to thank all the ATOMS group members, specially Ana Jorgelina Silveira for helping me with any theoretical and software doubts I had. Finally, I would like to thank Petrobras for the financial support.

# Abstract

This dissertation studied the solvation free energy differences of molecules mimicking asphaltenes in different solvents with the SAFT- $\gamma$  Mie force field. Solvation free energy differences were obtained by carrying out molecular dynamics simulations at the expanded ensemble. The output from these simulations was then used to estimate the differences with the MBAR method. The results with solvents other than water had low absolute deviations in relation to the experimental data. Meanwhile, the hydration free energy calculations required a binary interaction parameter estimated with output data from molecular dynamics in order to obtain accurate free energy differences. These results indicated some problems on the SAFT- $\gamma$  Mie model for water, but, generally, proved that a coarse grained model can represent the free energy differences of the studied sets of solute-solvent.

**Keywords:** solvation free energy. asphaltenes. SAFT- $\gamma$  Mie force field.

# List of Figures

2.2.1	Schematic representation for the two different approaches of coarse graining. . . . .	18
3.1.1	Periodic boundary condition representation. Taken from Frenkel and Smit (2001) . . . . .	36
3.1.2	Lennard Jones potential representation. . . . .	38
3.2.1	Values for parameter $\chi$ according to the ring geometry. Adapted from Müller and Mejía (2017). . . . .	42
3.3.1	Thermodynamic cycle for solvation free energy calculations with molecular dynamics (Adapted from Klimovich, Shirts and Mobley (2015)) . .	49
3.3.2	Soft-core potential in reduced units. . . . .	51
4.1.1	Geometry for $m_s = 5$ . . . . .	61
4.1.2	Geometry for $m_s = 3$ . . . . .	62
5.1.1	Cumulative probability . . . . .	66
5.1.2	Overlapping matrix for hexane+benzene. . . . .	68
5.1.3	Solvation free energy profiles of different solutes in hexane. . . . .	69
5.1.4	Solvation free energy profiles of different solutes in 1-octanol. . . . .	70
5.1.5	Solvation free energy profiles of different solutes in toluene. . . . .	70
5.1.6	Solvation free energy profiles of phenanthrene in toluene+ $CO_2$ . . . . .	72
5.2.1	Hydration free energy profiles for different solutes. . . . .	75
B.0.1	Overlapping matrix for hexane+pyrene. . . . .	91
B.0.2	Overlapping matrix for hexane+phenanthrene. . . . .	92
B.0.3	Overlapping matrix for 1-octanol+propane. . . . .	93
B.0.4	Overlapping matrix for 1-octanol+anthracene. . . . .	94
B.0.5	Overlapping matrix for 1-octanol+phenanthrene. . . . .	95
B.0.6	Overlapping matrix for toluene+pyrene. . . . .	96
B.0.7	Overlapping matrix for toluene+anthracene. . . . .	97
B.0.8	Overlapping matrix for toluene+phenanthrene. . . . .	98
B.0.9	Overlapping matrix for toluene+ $CO_2$ (0.087)+phenanthrene. . . . .	99
B.0.10	Overlapping matrix for toluene+ $CO_2$ (0.119)+phenanthrene. . . . .	100
B.0.11	Overlapping matrix for toluene+ $CO_2$ (0.169)+phenanthrene. . . . .	101
B.0.12	Overlapping matrix for toluene+ $CO_2$ (0.289)+phenanthrene. . . . .	102
B.0.13	Overlapping matrix for water+propane. . . . .	103
B.0.14	Overlapping matrix for water+benzene. . . . .	104
B.0.15	Overlapping matrix for water+toluene. . . . .	105
B.0.16	Overlapping matrix for water+phenanthrene. . . . .	106

# List of Tables

Table 1 – Estimated SAFT- $\gamma$ Mie Force Field parameters for phenanthrene . . . .	65
Table 2 – SAFT- $\gamma$ Mie Force Field for each substance used in this work . . . . .	66
Table 3 – Optimized values of $\lambda$ and $\eta$ for the pair benzene + hexane . . . . .	67
Table 4 – Calculated and experimental values for the solvation free energy differences (kcal/mol) of solutes in non aqueous solvents . . . . .	68
Table 5 – Calculated values for the solvation free energy differences (kcal/mol) of phenanthrene in toluene+ $CO_2$ . . . . .	71
Table 6 – Calculated values for the hydration free energy differences (kcal/mol) of solutes in water for $k_{ij} = 0$ . . . . .	72
Table 7 – Binary interaction parameters employed. . . . .	73
Table 8 – Calculated and experimental values for the hydration free energy differences (kcal/mol) of solutes in water. . . . .	74
Table 9 – Partition Coefficient Calculated from MD simulations and from experimental data. . . . .	76
Table 10 – Optimized values of $\lambda$ and $\eta$ for the solutes in hexane . . . . .	88
Table 11 – Optimized values of $\lambda$ and $\eta$ for the solutes in 1-octanol . . . . .	89
Table 12 – Optimized values of $\lambda$ and $\eta$ for the solutes in toluene . . . . .	89
Table 13 – Optimized values of $\lambda$ and $\eta$ for the phenanthrene in different mass fractions of $CO_2$ in toluene . . . . .	90
Table 14 – Optimized values of $\lambda$ and $\eta$ for the solutes in water . . . . .	90



# List of symbols

$T$	Temperature
$P$	Pressure
$V$	Volume
$t$	Time
$p$	Momentum
$r$	Coordinates
$U, u$	Potential Energy
$m$	mass
$v$	velocity
$P$	Pressure
$\mathcal{H}$	Hamiltonian
$q$	Generalized Coordinates
$K$	Kinetic Energy
$N$	Number of atoms/molecules
$h$	Planck Constant
$S$	Entropy
$k_b$	Boltzmann Constant
$\beta$	$1/k_bT$
$\mu$	Chemical Potential
$A$	Helmholtz Free Energy
$G$	Gibbs Free Energy
$f$	Free Energy
$F$	Forces

$\epsilon$	Depth of the potential well
$\sigma$	Distance correspondent to a zero intermolecular potential
$\lambda_r$	Repulsive exponent
$\lambda_a$	Attractive exponent
$x_i$	Molar fraction
$w_i$	Weight fraction
$\rho$	Density
$\lambda$	Coupling Parameter
$\eta$	Arbitrary Weight
$k_{ij}$	Binary Interaction Parameter

# Contents

<b>1</b>	<b>INTRODUCTION</b>	<b>12</b>
<b>2</b>	<b>LITERATURE REVIEW</b>	<b>15</b>
2.1	Molecular Simulations of Molecules Mimicking Asphaltenes	15
2.2	Coarse Grained (CG) Force Fields	16
2.3	Solvation Free Energies	20
2.4	Solvation Free Energy Calculation Methods	22
2.4.1	Thermodynamic integration	22
2.4.2	Histograms	23
2.4.3	Free Energy of Perturbation (FEP)	24
2.4.3.1	Bennet Acceptance Ratio (BAR)	25
2.4.3.2	Multistate Bennet Acceptance Ratio (MBAR)	26
<b>3</b>	<b>FUNDAMENTALS OF THE COMPUTATIONAL METHODS</b>	<b>28</b>
<b>3.1</b>	<b>Molecular Dynamics</b>	<b>28</b>
3.1.1	Background and Formalution	28
3.1.2	Statistical Ensembles	29
3.1.3	Thermostats and Barostats	31
3.1.4	Integration of the motion's equations	34
3.1.5	Initial Configuration	35
3.1.6	Force Fields	36
<b>3.2</b>	<b>SAFT-<math>\gamma</math> Mie Force Field</b>	<b>39</b>
3.2.1	SAFT-VR Mie EoS	39
3.2.1.1	Ideal Contribution	39
3.2.1.2	Monomer Contribution	40
3.2.1.3	Chain Contribution	41
3.2.1.4	Ring Contribution	41
3.2.1.5	Combining rules for the intermolecular potential parameters	42
3.2.2	Parameter Estimation for the SAFT- $\gamma$ Mie Force Field	43
<b>3.3</b>	<b>Solvation Free Energy Simulations Based on Molecular Dynamics</b>	<b>47</b>
<b>3.4</b>	<b>Multistate Bennet Acceptance Ratio (MBAR)</b>	<b>52</b>
<b>3.5</b>	<b>Expanded Ensemble Method</b>	<b>54</b>
<b>3.6</b>	<b>Gibbs Ensemble Monte Carlo (GEMC)</b>	<b>57</b>
<b>4</b>	<b>METHODOLOGY</b>	<b>61</b>
4.1	Phenanthrene Parameterization	61

4.2	Solvation Free Energy Calculations . . . . .	62
5	RESULTS AND DISCUSSION . . . . .	65
5.1	Solvation free energies . . . . .	65
5.2	Hydration free energies . . . . .	72
5.3	Partition Coefficients . . . . .	75
6	CONCLUSIONS . . . . .	77
	BIBLIOGRAPHY . . . . .	79
	APPENDIX A – OPTIMIZED VALUES OF $\lambda$ AND $\eta$ . . . . .	88
	APPENDIX B – OVERLAPPING MATRICES . . . . .	91
	APPENDIX C – WORK PUBLISHED IN SCIENTIFIC CONFERENCE	107
	APPENDIX D – PAPER FOR PUBLICATION IN SCIENTIFIC JOURNAL . . . . .	116

# 1 Introduction

Solvation free energy calculations with molecular dynamics (MD) have a variety of applications ranging from drug design in the pharmaceutical industry to development of separation technologies in the chemical industry. Solvation free energy is, more specifically, the difference in free energy related to the process of transferring the solute from the ideal gas phase condition to the liquid solvent phase condition (SHIRTS *et al.*, 2003). Through the study of the solvation phenomenon, it is possible to obtain information about the behavior of the solvent in different chemical environments and the influence of the solute's molecular geometry. It is also possible to calculate other important properties with the solvation free energy, namely the activity coefficient at infinite dilution, Henry constant and partition coefficients. Additionally, solvation free energy calculations can be part of the process of calculating solubility with molecular dynamics.

The solvation phenomenon described above is intrinsically complex. There are many competing forces interfering in the behavior of the solute-solvent interaction, and free energy simulations are susceptible to sampling problems in low energy regions. Various simulation methodologies were developed to enable estimations of the energy differences such as the expanded ensemble (LYUBARTSEV *et al.*, 1992), thermodynamic integration (KIRKWOOD, 1935), free energy perturbation (ZWANZIG, 1954; BENNETT, 1976; SHIRTS; CHODERA, 2008) and umbrella sampling (TORRIE; VALLEAU, 1977).

Another influencing factor in the output of these calculations is the choice of force field used to model the solvent and solute molecules. Force field is the name given for the group of parameters and equations used to represent the potential energy function of a system in molecular simulations. They have different levels of description, such as quantum mechanics, atomistic and coarse grained. The quantum mechanics approach describes the motion of electrons and requires the solution of the Schrodinger equation during the simulation. While, in the atomistic description, only the atomic motions

are described, and this is done by solving the newton's motion equations. Finally, in the coarse grained description, atoms are grouped in pseudo atoms or beads and the motion's equations are solved for them. Coarse grained models generally reproduce free energy differences since the effects of reducing degrees of freedom in the entropy are counterbalanced by the reduction of enthalpic terms (KMIECIK *et al.*, 2016). Additionally, the success of a coarse grained force field is important to decrease the computational time of solvation free energy calculations and reveal deficiencies in the description of small molecules by these models (MOBLEY *et al.*, 2007; SHIRTS *et al.*, 2003). Hence, we, in this study, assess the efficiencies and deficiencies of the SAFT- $\gamma$  Mie coarse grained force field (AVENDAÑO *et al.*, 2011) with free energy calculations for a variety of pairs solute-solvent. This force field was chosen because it uses, unlike the majority of the force fields, the Mie potential (MIE, 1903) and its method of obtaining its parameters is more straightforward than other models. It was initially parameterized with pure component equilibrium and interfacial tension data (AVENDAÑO *et al.*, 2011). This strategy has provided satisfactory results for prediction of phase equilibrium of aromatic compounds, alkanes, light gases, and water (HERDES; TOTTON; MÜLLER, 2015; MÜLLER; MEJÍA, 2017; LOBANOVA *et al.*, 2015) , thermodynamic properties of carbon dioxide and methane (AIMOLI; MAGINN; ABREU, 2014a), multiphase equilibrium of mixtures of water, carbon dioxide, and n-alkanes (LOBANOVA *et al.*, 2016) and water/oil interfacial tension (HERDES *et al.*, 2017).

The solvents and solutes in our free energy calculations were picked in order to test the force field with standard sets used as benchmark in solvation free energy calculations and with aromatic substances used as a model to asphaltenes. Asphaltenes are complicated to characterize by determining their composition on a molecular basis, but it is generally accepted that they can be characterized as a fraction of crude oil soluble in toluene and insoluble in n-alkenes (pentane, hexane, heptane) (SJÖBLOM *et al.*, 2003). They have motivated many studies with interest in developing models for their structure and behavior due to all the problems they can cause during their transportation and refining such as precipitation during the oil processing (SJÖBLOM; SIMON; XU, 2015).

This is a recurrent problem due to the growing market of the production of crude oil in deep waters, which have conditions favorable to precipitation, as pressure depletion and acid stimulation (BUENROSTRO-GONZALEZ *et al.*, 2004). As an example, asphaltene precipitation due to pressure drop can clog oil production equipment and cause an almost exponential increase in the cost of production (BUENROSTRO-GONZALEZ *et al.*, 2004; JOSHI *et al.*, 2001). What makes the understanding of the behavior of asphaltenes in different chemical and physical environments important to the oil industry.

As said in the previous paragraph, asphaltene characterization still faces some issues. Hence, we choose to use polycyclic aromatic hydrocarbons (PAH'S), which have well defined characteristics, to initially test the efficiency of the SAFT- $\gamma$  Mie force field in describing the solvation phenomenon. PAH's are a group of organic compounds that have fused rings, carbon and hydrogen in their structure (RAVINDRA; SOKHI; GRIEKEN, 2008). The ones utilized in this work were phenanthrene, anthracene and pyrene, since they have similarities in terms of solubilities with asphaltenes. Meanwhile, we selected compounds that are used to characterize asphaltenes (toluene, hexane) as solvents in our free energy calculations. The anti solvent/solvent effect of carbon dioxide was also tested due to its influence in asphaltene precipitation during the oil processing (SOROUSH *et al.*, 2014). With this study of solvation free energies with the SAFT- $\gamma$  Mie model, we intend to improve this force field and provide accurate free energy calculations of PAH's with a coarse grained model. The correct description of these smaller asphaltene-like compounds by this force field opens up the possibility of obtaining satisfactory results for more complex asphaltene models with a less computational expensive force field.

## 2 Literature Review

### 2.1 Molecular Simulations of Molecules Mimicking Asphaltenes

Asphaltenes, unlike the majority of the compounds, are not defined on a molecular basis. Their most accepted definition is that they are a fraction of crude oil insoluble in n-alkanes (pentane, hexane and heptane) and soluble in toluene (SJÖBLOM *et al.*, 2003). Due to uncertainties related to its structures, much work has been done to develop model compounds that have well defined structure and can generally represent asphaltenes. The two categories of models presented in the literature are the archipelago and continental models. In the archipelago model, asphaltenes consist of polyaromatic parts linked together by aliphatic or naphthemic moieties and, in the continental model, they consist of a single polyaromatic ring with linked aliphatic or naphthenic chains (MULLINS, 2010; MURGICH, 2003). Studies with molecular simulation uses this models or compounds, such as toluene and pyrene, that have similar solubility properties. The choice of the model's structure, such as chemical bonding, is highly important, since some structures can cause the occurrence of high energies regions during the simulation (LI; GREENFIELD, 2011) .

Ervik *et al.* (2016) obtained correct interfacial orientation of asphaltenes using coarse grained molecular dynamics simulations of the interface, with a representative model for the asphaltene molecules. Also using a coarse grained force field, Jover *et al.* (2015) carried molecular simulations with a continental asphaltene model. The results reproduced experimental data of the strong aggregation of asphaltene molecules in n-heptane and high solubility in toluene. Gao *et al.* (2014) performed a molecular dynamics study with the force field GROMOS 45a3 force field (SCHULER; DAURA; GUNSTEREN, 2001) to identify the structural features of different asphaltene molecules. The archipelago model was employed in the work of Mikami *et al.* (2013) to investigate interfacial behavior of asphaltene molecules at the oil - water interface using molecular



dynamics simulations with the OPLS-AA force field (JORGENSEN; TIRADO-RIVES, 1988). They found that asphaltenes are preferably distributed in the oil phase in the case of pure toluene and at the oil - water interface in the case of pure heptane and an oscillatory behavior of asphaltene molecules at the oil - water interface was also discovered.

A pyrene based model was used in the works of Teklebrhan *et al.* (2014) to study molecular association and interaction as well as the adsorption properties of the pyrene molecule at the water/toluene or water/heptane interface. Molecular dynamics simulations were also used in the study of the nanoaggregation of four types of model asphaltene molecules in binary mixtures of toluene and water (KUZNICKI; MASLIYAH; BHATTACHARJEE, 2009). The authors observed that in thin films of toluene trapped between two aqueous phases, both interface-bound and core-bound asphaltenes have similar diffusion behavior. Headen *et al.* (2017) reported molecular dynamics simulations of four model asphaltenes. They alleged that there is no formation of nanoaggregates, and the distribution of asphaltene clusters is continuous for mixtures of asphaltene in heptane. Generally the work on molecular simulation with asphaltenes models showed a difference in packing tendencies according to the model (GREENFIELD, 2011). For a thorough review of studies of different models of asphaltenes, the reader is referred elsewhere (GREENFIELD, 2011).

## 2.2 Coarse Grained (CG) Force Fields

Molecular simulations can be carried out at different levels of description. The detailed atomistic level or *ab initio* level is described by the laws of quantum mechanics. The system consists of a set of subatomic particles in which Schrodinger's equation is solved for all of them. The next level is the atomistic description. It considers that the system is made up of atoms following the laws of classical mechanics. Force fields at this level are based on van der Waals interactions, which may include neutral or Coulombic charged sites. Contributions due to intramolecular interactions such as bond-stretching, angle-bending and torsion are also usually accounted in these kinds of force fields.

When the simulation scale needs to be increased and the atomistic simulations become too computationally expensive, the coarse-grained (CG) description is more suited. It considers that the system is made up of pseudo atoms or beads that contain multiple atoms or even an entire molecule.

There is an obvious loss of information in grouping atoms, hence it is necessary to assure that the process of eliminating unnecessary or unimportant information ('coarse graining') does not affect the system's physical behavior. Ideally, coarse grained models need to have representability, robustness, transferability, and computational efficiency. Representability means that you can use a model at a state point other than the one in which it was parameterized. The other characteristic, robustness, is related to the model's ability of enabling reliable predictions for various structural, thermodynamic, or transport properties. Finally, a transferable model is one in which the representation of atomic or chemical moieties have the same behavior in different molecules- e. g., a pseudo atom representing  $CH_2$  should have the same properties both in an alkene molecule and in a polyethylene molecule (MÜLLER; JACKSON, 2014). To achieve these goals, coarse grained force fields are usually developed by mapping the atomistic model in order to define the pseudo atoms, which are generally formed by similar functional groups. The level of coarse graining also needs to be defined. Hadley and McCabe (2012) affirm that six heavy atoms (non-hydrogen atoms) per bead are traditionally used in order to not lose important details and maintain isotropic representations of the beads. After the mapping, CG force fields needs to be parametrized. There are two different approaches, bottom up and top down, to link the simulations on the coarse grained scale to a another scale, as it is schematically represented in Figure 2.2.1. The bottom up approach uses information of a more detailed scale such as the quantum mechanics description or the atomistic description to obtain information necessary to the parametrization. This method highly depends on the detailed model quality to succeed. Meanwhile, the top down methodology obtains parameters from larger scales, namely experimental thermodynamic properties or structure based properties.

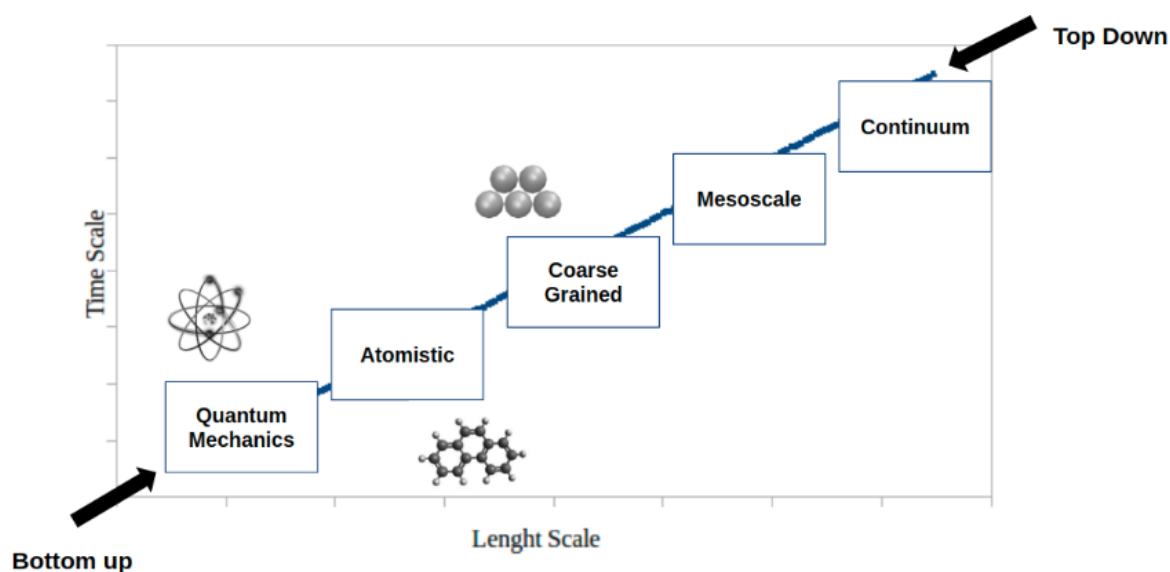


Figure 2.2.1 – Schematic representation for the two different approaches of coarse graining.

One of the first applications of coarse grained models is in the study of protein folding ([LEVITT; WARSHE, 1975](#); [LEVITT, 1976](#)). These earlier protein CG models were based on known molecular structure, and they contributed for the knowledge of physicochemical forces associated with protein folding and protein interactions ([KOGE; TAKADA, 2001](#)). More recently, models focused on retaining the protein's chemical specificity. The Bereau and Deresmo model ([BEREAU; DESERNO, 2009](#)) represents a single amino acid with a maximum of four beads, and it was used in studies of protein folding and aggregation. However, this model still needs tuning to improve protein stability ([BEREAU; BACHMANN; DESERNO, 2010](#)). The OPEP (Optimized Potential for Efficient Protein Structure Prediction) model ([STERPONE \*et al.\*, 2014](#); [STERPONE; DERREUMAUX; MELCHIONNA, 2015](#)) represents a single amino acid with a maximum of six beads. It was used to investigate a variety of phenomena, ranging from protein folding to the modeling of DNA-RNA complexes ([BARDUCCI; BONOMI; DERREUMAUX, 2011](#); [CHEBARO \*et al.\*, 2009](#); [STERPONE \*et al.\*, 2014](#)). Other CG protein models used in the literature are the Scorpion (solvated coarse-grained protein interaction) ([BASDEVANT; BORGIS; HA-DUONG, 2013](#)), the UNRES (united residue) ([ADAM \*et al.\*, 2014](#)) and the MARTINI model ([LARS \*et al.\*, 2013](#)). The later

one is the most popular model for CG modeling of membrane proteins ([MARRINK; TIELEMAN, 2013](#)). The MARTINI force field is also extensively used as a CG model for water. This force field represents four water molecules as one bead using a shifted Lennard-Jones potential for non-bonded interactions. Despite its extensive use, the MARTINI water model does not properly reproduce properties such as interfacial tension and compressibility ([HE \*et al.\*, 2010](#)). Besides, it can freeze at room temperature ([WINGER \*et al.\*, 2009](#); [MARRINK \*et al.\*, 2007](#)), which requires the use of anti-freeze agents during the simulations. This behavior can be explained by the high level of coarse graining (4:1), the lack of explicit charges, and the use of a 12-6 potential. [Chiu, Scott and Jakobsson \(2010\)](#) used the Morse Potential, which is softer than the LJ potential, to improve the MARTINI model. Meanwhile, [Shinoda, Devane and Klein \(2007\)](#) used different forms of the Mie potential to build a versatile and transferable coarse grained model for surfactants/water systems using density, interfacial, and hydration free energies data. They selected a 12-4 Mie potential for water cross interactions and a 9-6 Mie potential for the surfactant (alkanes, oxyethylenes, ethyleneglycols, ethers and alcohols) interactions.

Outside of the Martini framework, [Orsi and Essex \(2011\)](#) proposed the ELBA coarse grained model for molecular dynamics simulations of lipids membranes. In this model, electrostatics are modeled explicitly by charges and water molecules are represented by a single Lennard-Jones bead embedded with a point dipole. [Genheden \(2016\)](#) expanded the Elba force field to model 1-hexanol, 1-nonanol, n-hexane and n-nonane by representing three carbons with a single bead. Using different Mie and Morse potentials, [He \*et al.\* \(2010\)](#) studied different levels of coarse-graining for water ranging for one to 4 molecules per bead. Other investigations also assessed the use of Soft-core potentials to study aqueous solutions of surfactants ([SHINODA; DEVANE; KLEIN, 2007](#)), ionic liquids ([BHARGAVA; KLEIN, 2009](#)), lipids ([SHINODA; DEVANE; KLEIN, 2010](#)), and membranes ([PANTANO; KLEIN, 2009](#)). Another CG force field for water based on the Mie Potential is the SAFT- $\gamma$  Mie ([LOBANOVA \*et al.\*, 2015](#)). In this strategy, there are two different models: CGW1-vle and CGW1-ift. Both of them

represent the water molecule as one bead and the Mie Potential has a repulsive and attractive exponents equal to eight and six, respectively. The CGW1-vle model was parameterized using saturated-liquid density and vapor pressure data, and should be used for simulations of aqueous systems in fluid-phase equilibrium at high temperatures and pressures. This model still suffers from premature freezing with a triple point at 343 K. The other model, CGW1-ift, was parameterized using saturated-liquid density and vapor-liquid interfacial tension, hence it is best suited for interfacial property calculations. Both models have temperature-dependent size and energy parameters and performed well for these properties over the entire liquid temperature range. The SAFT- $\gamma$  Mie force field have also been applied to other compounds with satisfactory results. [Müller and Mejía \(2017\)](#) parameterized the force field for aromatic compounds and tested it with simulations of fluid phase equilibrium. [Herdes, Totton and Müller \(2015\)](#) carried out simulations of alkanes and light gases. Binary and ternary mixtures of water, carbon-dioxide, and water ([LOBANOVA \*et al.\*, 2016](#)), there are also thermodynamic and transport properties of carbon dioxide and methane ([AIMOLI; MAGINN; ABREU, 2014a](#); [AIMOLI; MAGINN; ABREU, 2014b](#)) and water/oil interfacial tension ([HERDES \*et al.\*, 2017](#)) studies with this force field.

## 2.3 Solvation Free Energies

Solvation free energy calculations with molecular dynamics have a variety of applications due the amount of information it can provide about the behavior of the solvent in different chemical environments and the influence of the solute's molecular geometry. Free energy calculations have an inherent complexity that attracted studies in order to improve free energy simulations and post processing methods ([SHIRTS; CHODERA, 2008](#); [PALIWAL; SHIRTS, 2011](#); [SHIRTS; PANDE, 2005](#); [YTREBERG; SWENDSEN; ZUCKERMAN, 2006](#)) in the last decades.

Recent work ([MOBLEY; GUTHRIE, 2014](#); [MATOS \*et al.\*, 2017](#)) made available a big database of hydration free energy of small molecules using the GAFF force field. [Beckstein, Fourrier and Iorga \(2014\)](#) also calculated the hydration free energies

for 52 compounds with OPLS-AA force field. They obtained an overall root mean square deviation of the prediction from the experimental data of 1.75 kcal/mol and concluded that the precision of the results are mainly limited by the reproducibility of the Lennard-Jones contribution towards the solvation free energy. A comparison of polar and nonpolar contributions to these hydration free energy indicated the significance of each the terms (IZAIRI; KAMBERAJ, 2017). Garrido *et al.* (2009), Garrido *et al.* (2011) calculated the free energy of solvation of large alkanes in 1-octanol and water with three different force fields (TraPPE, Gromos, OPLS-AA/TraPPE) and the solvation free energy of propane and benzene in non aqueous solvents like n-hexadecane, n-hexane, ethyl benzene and acetone with the force fields TraPPE-UA and TraPPE-AA. Roy, Blinov and Kovalenko (2017) addressed the choice of the Lennard Jones parameters for predicting solvation free energy in 1-octanol. Gonçalves and Stassen (2005) calculated the free energy of solvation in the solvents tetrachloride, chloroform and benzene with GROMOS force field. Using the GAFF and the polarizable AMOEBA force fields, Mohamed, Bradshaw and Essex (2016) evaluated the solvation free energy of small molecules in toluene, chloroform and acetonitrile, and obtained a mean unsigned error of 1.22 kcal/mol for AMOEBA and 0.66 kcal/mol for GAFF. In order to define the role of solvent water in the docking structure determination, Matubayasi (2017) developed a method to compute the solvation free energy of proteins while using OPLS-AA force field for the solutes and TIP3P for water. Genheden (2016) expanded the Elba force field to calculate solvation free energies in polar (water, hexanol, octanol and nonanol) and apolar (hexane, octane and nonane) solvents, and obtained mean absolute deviations of 1 kcal/mol for water and 1.5 kcal/mol for hexane. In this model, three carbons are represented by a single bead and water is represented by a single bead.

Though these variety of data using the intramolecular Lennard-Jones potential, we are not aware of works using the Mie Potential (MIE, 1903) in free energy calculations. We, at this study, try to provide information about theses calculations with the SAFT- $\gamma$  Mie coarse grained force field. The output of these calculations are highly dependent on the force field and deficiencies in the description of small molecules by the models

can be revealed with these calculations (MOBLEY *et al.*, 2007; SHIRTS *et al.*, 2003). Other important reason for testing a coarse grained force field is that they can generally reproduce free energy difference since the effects of the degrees of freedom reduction in the entropy are counterbalanced by reduced enthalpic terms (KMIECIK *et al.*, 2016). Hence, knowing if more coarse grained approaches have a similar performance to the all atoms force fields can help increase the scale of solvation free energy calculations.

## 2.4 Solvation Free Energy Calculation Methods

The data from molecular dynamics simulations provide potential energies that need to be post processed and analyzed in order to calculate the solvation free energies. Since these calculations can have slow convergences, a lot of papers in the last decades focused in developing methods to improve sampling and analysis techniques. Almost all methods rely on three different approaches: free energy of perturbation (FEP), histogram and thermodynamic integration methods.

### 2.4.1 Thermodynamic integration

The thermodynamic integration method (KIRKWOOD, 1935) uses equilibrium averages to evaluate the energy derivative with respect to the coupling parameter ( $\lambda$ ):

$$\frac{\partial(1/k_b T)G}{\partial\lambda} = \left\langle \frac{\partial\mathcal{H}}{\partial\lambda} \right\rangle \quad (2.1)$$

In Eq. (2.1),  $k_b$  is the Boltzmann constant,  $G$  is the Gibbs free energy and  $\mathcal{H}$  is the Hamiltonian of the system. The derivative is obtained by interpolating the output data between the states from simulations. Some examples of methods for the interpolations are the trapezoidal rule or natural cubic spline (PALIWAL; SHIRTS, 2011). There are also more complex schemes that are usually system specific as the works of Jorge *et al.* (2010) and Shyu and Ytreberg (2010). MD simulations for each coupling parameter  $k$  are carried out and the average over the derivative at each state is computed in order to

obtain the final solvation free energy:

$$\Delta G \approx \sum_k \left\langle \frac{\partial \mathcal{H}}{\partial \lambda} \right\rangle \quad (2.2)$$

## 2.4.2 Histograms

Histograms are used to compute probability distributions. Usually every histogram bin is treated as number of visits to a specific state. The standard practice when using histograms is to use the weighted histogram analysis method (WHAM) developed by [Ferrenberg and Swendsen \(1989\)](#) and generalized by [Kumar \*et al.\* \(1992\)](#) ([CHIPOT; POHORILLE, 2007](#)) to put together different histograms by minimizing the statistical error in the computed density of states and entropy function. This method describes the total probability distribution as a weighted sum of probability distributions without bias obtained from biased simulations. This method was developed to avoid problems related to data loss, high uncertainties and the calculation of the constant of the free energy added to the system by the biased potential ([ROUX, 1995](#)). The probability distribution dependent on the potential energy ( $U$ ) and temperature ( $T$ ) ( $\tilde{\varrho}_r^*(U, T)$ ) for the WHAM is:

$$\tilde{\varrho}_r^*(U, T) = \frac{\sum_i f_i(U) \exp(-\beta U)}{\sum_i f_{tot,i} \exp(\beta_i \tilde{A}_i - \beta_i U)} \quad (2.3)$$

$$\exp(-\beta_i \tilde{A}_i) = \sum_U \tilde{\varrho}_r^*(U, T) \quad (2.4)$$

$$\tilde{\varrho}_r^*(U, T) = \frac{\tilde{\varrho}_r^*(U, T)}{\sum_U \tilde{\varrho}_r^*(U, T)} \quad (2.5)$$

where  $\beta = 1/k_b T$ ,  $\tilde{A}_i$  gives the free energy for run  $i$ ,  $f_i(U)$  is the number of counts of energy  $U$  for run  $i$  and  $f_{tot,i}$  is the total number of counts in run  $i$ . The Eq. (2.3) and (2.4) are solved self consistently with the initial value for  $\tilde{A}_i$  equal to zero. The final probability distribution is then given by Eq. (2.5), and is used to calculate various



moments of the potential energy (CHIPOT; POHORILLE, 2007).

### 2.4.3 Free Energy of Perturbation (FEP)

The free energy of perturbation method (ZWANZIG, 1954) is the oldest and one of the most general purpose strategy to calculate free energy differences. In this method, the thermodynamics of two different systems( A and B) are related with the intention of evaluating differences in intermolecular potentials. This energy change from state A to state B is calculated by:

$$\Delta G_{AB} = -k_b T \ln \langle e^{-\beta(U_B - U_A)} \rangle_A \quad (2.6)$$

According to the equation above, the free energy difference is calculated by doing an average over the potential energies of state A and B obtained during the simulation of state A. This method requires a great overlap between states( the state B needs to represent a small perturbation in state A) in order to obtain a rapid convergence of the free energy difference. To assure overlap, it is possible to carry out simulations in N intermediate states between A and B, so Eq. (2.6) becomes:

$$\Delta G_{AB} = -k_b T \ln \left( \frac{1}{N} \sum_{i=0}^{N+1} e^{-\beta(U_{i+1} - U_i)} \right) \quad (2.7)$$

The way of calculating  $\Delta G$  of Eq. (2.7) is called Exponential Averaging (EXP) (ZWANZIG, 1955; PALIWAL; SHIRTS, 2011). The direction of the transformation is also important in this method. If the direction is of decreasing entropy, the step is of insertion ( $\Delta G_{AB}$ ) and the method is called insertion exponential averaging (IEXP). The direction of increasing entropy is called a deletion step ( $\Delta G_{BA}$ ) and the method is labeled as deletion exponential averaging (DEXP). These directions can yield different values of free energy differences due to under sampling in the tail regions of the  $\Delta G_{AB}$  distribution (KLIMOVICH; SHIRTS; MOBLEY, 2015; POHORILLE; JARZYNSKI; CHIPOT, 2010). These problems make the EXP methods not suited to calculate free

energy differences when the system hasn't a sufficient overlap. For these cases, the Bennet Acceptance Ratio or the Multi-State Bennet Acceptance Ratio is more indicated.

#### 2.4.3.1 Bennet Acceptance Ratio (BAR)

The BAR method (BENNETT, 1976) was developed with the intent of eliminating the bias in the free energy estimation. It uses the uncorrelated samples of the potential energy in both directions ( $A \rightarrow B$  and  $B \rightarrow A$ ) to obtain the free energy differences using the information in a statically optimal way. The free energy difference between two intermediate states (i and j) is calculated by the self-consistent solution of the following equations:

$$\Delta G_{ij} = \frac{1}{\beta} \ln \left( \frac{\sum_{k=1}^{N_j} \frac{1}{1 + \exp[-\beta(\Delta U_k^j - C)]}}{\sum_{l=1}^{N_i} \frac{1}{1 + \exp[-\beta(\Delta U_l^i - C)]}} \right) + C - \frac{1}{\beta} \ln \left( \frac{N_j}{N_i} \right) \quad (2.8)$$

$$C = \Delta G_{ij} + \frac{1}{\beta} \ln \left( \frac{N_j}{N_i} \right) \quad (2.9)$$

The total free energy difference between end states is then given by the sum over differences of consecutive intermediate states. This method also provides a function to obtain the minimum variance for free energy differences. The variance equation for any value of C is given by:

$$s_{ij}^2 = \frac{1}{\beta^2 N_i} \left[ \frac{\langle f^2(x) \rangle_i}{\langle f(x) \rangle_i^2} - 1 \right] + \frac{1}{\beta^2 N_j} \left[ \frac{\langle f^2(x) \rangle_j}{\langle f(x) \rangle_j^2} - 1 \right] \quad (2.10)$$

where  $f(x) = 1/(1+x)$  is the Fermi equation and  $x = \exp[\beta(\Delta U - C)]$ . The variance of the free energy difference between end states can be calculated by assuming independent errors and summing over the variance of consecutive intermediate states. However, this assumption is not correct and there is no general formula to obtain a statistically unbiased estimate of an entire transformation with the BAR method (PALIWAL; SHIRTS,

2011).

There are two other methods related to the BAR method that don't solve Eqs. (2.8) and (2.9) self consistently. By doing that, free energy differences will not have minimum variance, but significant space and disk memory can be saved since the averages of Eqs. (2.8) - (2.10) are accumulated (PALIWAL; SHIRTS, 2011). The two methods are the Unoptimized Bennett Acceptance Ratio (UBAR) and the Range-Based Bennett Acceptance Ratio (RBAR). The first one avoids the self consistently resolution of the BAR equations by defining  $C = \beta^{-1} \ln(N_j/N_i)$ . The UBAR method also requires that the intermediate free energy differences are approximately equal to zero to obtain optimal estimations. Meanwhile, the RBAR method selects a range of initial guesses of the constant  $C$  in order to calculate a range of  $\Delta G_{ij}$ . The value of free energy difference correspondent to the minimum variance is then used as input in Eq. (2.9) to calculate the value of  $C$ . Hence, this method requires a good estimation of the initial range for the values of  $C$ . In terms of accuracy, the UBAR method can be as accurate as the BAR method, but it may end up being as computational costly (PALIWAL; SHIRTS, 2011).

#### 2.4.3.2 Multistate Bennet Acceptance Ratio (MBAR)

The MBAR method (SHIRTS; CHODERA, 2008) is a further development of the BAR method. It proposes an estimator that computes free energies and their uncertainties of all  $K$  states by minimizing the  $K \times K$  matrix of variances simultaneously. The estimator solves the following equation for each  $G_i$  self consistently:

$$G_i = \frac{1}{\beta} \ln \sum_{k=1}^K \sum_{n=1}^{N_k} \frac{\exp[-\beta U_i(x_{kn})]}{\sum_{l=1}^K N_l \exp[\beta(G_l - U_l(x_{kn}))]} \quad (2.11)$$

The equation above requires the evaluation of the potential energy of uncorrelated configuration  $n$  for all  $K$  states ( $U_i(x_{kn})$ ) and for all uncorrelated configuration snapshots ( $N_k$ ) from state  $k$ . Free energy changes between states are given then by

$\Delta G_{ij} = G_j - G_i$ . The statistical variance of  $S_{ij}^2 \Delta G_{ij}$  is given by the matrix covariances:

$$s_{ij}^2 \Delta G_{ij} \equiv \text{cov}(-\ln \hat{Z}_j / \hat{Z}_i, -\ln \hat{Z}_j / \hat{Z}_i) \quad (2.12)$$

where  $\hat{Z}_j$  and  $\hat{Z}_i$  are the partition functions of states  $i$  and  $j$ .

# 3 Fundamentals of the Computational Methods

## 3.1 Molecular Dynamics

### 3.1.1 Background and Formalution

Molecular Dynamics (MD) is a kind of molecular simulation that uses molecular configurations (Cartesian coordinates and momentum) to extract structural , thermodynamical and dynamical information of a system. This information is extracted from the time evolution of a system, which are obtained through the Newton motion' equations numerical integration ([TUCKERMAN, 2010](#)):

$$\frac{d\vec{p}_i}{dt} = -\frac{\partial U(\vec{r}_N)}{\partial \vec{r}_i} \quad (3.1)$$

where  $p_i$  is the momentum and  $r^N$  are the coordinates of all the atoms  $(x_1, y_1, z_1, \dots, x_N, y_N, z_N)$ . Alternatively, we can write the equation relative to the velocity ( $v_i$ ):

$$m_i \frac{d\vec{v}_i}{dt} = -\frac{\partial U(\vec{r}_N)}{\partial \vec{r}_i} \quad (3.2)$$

In order to develop equations for any coordinate system ( $q^N = (r_1, \theta_1, \phi_1)$ ), the Halmitonian formulation, a more generalized formulation of classical mechanics, is used to develop the equations of motion:

$$\mathcal{H}(q^N, p^N) = K(p^N) + U(q^N) \quad (3.3)$$

In the equation above,  $K$  is the kinetic energy and  $U$  is the potential energy. The

equations of motion can now be represented by:

$$\frac{d\vec{p}_i}{dt} = -\frac{\partial \mathcal{H}}{\partial \vec{q}_i} \quad (3.4)$$

$$\frac{d\vec{q}_i}{dt} = \frac{\partial \mathcal{H}}{\partial \vec{p}_i} \quad (3.5)$$

The coordinates and momentum axes for each atom in a 6N dimensional space is defined as the phase space. The trajectory through the phase space is then the time evolution of a system in a molecular dynamics simulation. This evolution of the simulation may be used to calculate the thermodynamic properties if the system is ergodic. That is, a trajectory in this system will explore with the same probability all regions of the phase space of microstates with the same energy (SHELL, 2015).

### 3.1.2 Statistical Ensembles

A statistical ensemble corresponds to the set of configurations of a system. For an isolated system at equilibrium, the ensemble corresponds to the microcanonical ensemble. This ensemble has as control variables the number of particles (N), volume (V) and total energy (E). Following the ergodic hypothesis, the system at these conditions will spend the same amount of time in each of the microstates (points in phase space) with the fixed E. The number of accessible microstates is defined by the partition function or the density of states, and, is given by the following equation for the microcanonical ensemble:

$$\Omega(N, V, E) = \frac{1}{h^{3N} N!} \int dp^N dr^N \delta[\mathcal{H}(p^N, r^N) - E] \quad (3.6)$$

where h is the Planck constant and the delta function is a Dirac delta function. As mentioned above, the system will spend the same amount of time at each of the microstates,

i. e. each of these microstates have equal probabilities ( $\varrho$ ) of being visited:

$$\varrho(p^N, r^N) = \frac{[\mathcal{H}(p^N, r^N) - E]}{\Omega(N, V, E)} \quad (3.7)$$

In order to obtain the macroscopic properties from molecular dynamics, we need to have the relation of the microcanonical partition function to the entropy:

$$S = k_b \ln \Omega(N, V, E) \quad (3.8)$$

where  $k_b$  is the Boltzmann constant. With this equations, we can derive other relations to macroscopic properties with the fundamental equation:

$$dS = \frac{1}{T}dE + \frac{P}{T}dV + \frac{\mu}{T}dN \quad (3.9)$$

$$dE = TdS + PdV + \mu dN \quad (3.10)$$

As said above, the microcanonical ensemble have N,V,E as its control variable. Other ensembles can also be defined according to the macroscopic properties held constant. In the canonical ensemble, N, V and the temperature (T) are held constant and N, pressure (P) and T are held constant in the isothermal-isobaric ensemble. Other ensembles include the isenthalpic-isobaric (constant number of particles, pressure and enthalpy) and the grand canonical (constant chemical potential, volume and temperature). A variety of physical properties are measure at the conditions of the isenthalpic-isobaric ensemble such as enthalpies, entropies, redox potential, equilibrium constants and free energies, what makes this ensemble one of the most important (TUCKERMAN, 2010). This is also the ensemble in which solvation free energy simulations are carried at this work, hence we are going to briefly talk about it. This ensemble is obtained from a Legendre transformation on the canonical ensemble. The Helmholtz free energy  $A(N, V, T)$  becomes the Gibbs free energy  $G(N, P, T)$  by transforming the volume into

the external pressure:

$$G(N, P, T) = A(N, V(P), T) + PV(P) \quad (3.11)$$

The Gibbs free energy is related to its partition function  $\Delta(N, P, T)$  by:

$$G(N, P, T) = -\kappa_b T \ln \Delta(N, P, T) \quad (3.12)$$

where  $\Delta(N, P, T)$  is given by:

$$\Delta(N, P, T) = \frac{1}{V_0} \int_0^\infty dV \int d^N p d^N r \exp \left[ -\beta \left( \sum_{i=1}^N \frac{p_i^2}{2m_i} + U(r^N) + PV(r^N) \right) \right] \quad (3.13)$$

In the equation above,  $Q(N, V, T)$  is the partition function of the canonical ensemble:

$$Q(N, V, T) = \int d^N p d^N r \exp \left[ -\beta \left( \sum_{i=1}^N \frac{p_i^2}{2m_i} + U(r^N) \right) \right] \quad (3.14)$$

From these relations and a differential change in  $G$ , we can obtain the chemical potential ( $\mu$ ), volume and entropy ( $S$ ) relations for isenthalpic-isobaric ensemble:

$$\mu = \left( \frac{\partial G}{\partial N} \right)_{P,T} = -\kappa_b T \left( \frac{\partial \ln \Delta(N, P, T)}{\partial N} \right)_{N,T} \quad (3.15)$$

$$\langle V \rangle = \left( \frac{\partial G}{\partial P} \right)_{N,T} = \kappa_b T \left( \frac{\partial \ln \Delta(N, P, T)}{\partial P} \right)_{N,P} \quad (3.16)$$

$$S = \left( \frac{\partial G}{\partial T} \right)_{N,P} = \kappa_b (\ln Q(N, V, T) + T \left( \frac{\partial \ln Q(N, V, T)}{\partial T} \right)_{V,N}) \quad (3.17)$$

### 3.1.3 Thermostats and Barostats

The isothermal-isobaric and canonical ensembles have external conditions being applied to it (temperature and pressure). For temperature control, the method employed



mimics the effect of a thermal reservoir through a thermostat. The thermostats need to be capable of capturing the correct energy fluctuations in the system since the kinetic energy will fluctuate when using a heat bath to control temperature in a canonical ensemble of a finite system.

Among the available thermostat are the Berendsen (BERENDSEN *et al.*, 1984), the Andersen (ANDERSEN, 1980) and the Nose (NOSÉ, 1984) thermostats, but here we are going to discuss the most widely used thermostat: the Nosé-Hoover (HOOVER, 1985). This thermostat is based on the formulation of Nosé (NOSÉ, 1984), whom used a Lagrangian that contains additional, artificial coordinates and velocities (FRENKEL; SMIT, 2001). In this method the Halmitonian in a canonical ensemble is constructed as:

$$\mathcal{H} = K(p^N) + U(q^N) + \frac{\xi^2 Q}{2} + 3Nk_b T \ln s \quad (3.18)$$

where  $\xi$  is a friction coefficient related to the conjugate momentum of the thermal reservoir to which the system is coupled,  $s$  is the position of the thermal reservoir and  $Q$  is the effective mass associated with  $s$ . The velocity update is then done with the Newton's equation with the addition of the friction term (SHELL, 2015):

$$\frac{dr_i}{dt} = v_i \quad (3.19)$$

$$\frac{dv_i}{dt} = -\frac{1}{m_i} \frac{\partial U(r^N)}{\partial r_i} - \xi v_i \quad (3.20)$$

$$\frac{\xi}{dt} = \frac{\sum m_i v_i - 3Nk_b T}{Q} \quad (3.21)$$

$$\frac{\xi}{dt} = -\frac{1}{m_i} \frac{\partial U(r^N)}{\partial r_i} - \xi v_i \quad (3.22)$$

To increase the robustness of the Nosé-Hoover thermostat, the Nosé-Hoover chains of thermostats method was developed. It proposes the use of multiple thermal

reservoirs that are linked to enhance temperature equilibration (SHELL, 2015).

Meanwhile, the pressure is controlled with a barostat. It maintains the pressure constant during the simulation by adjusting the simulation volume. Among the available barostats methodologies are the Berendsen (BERENDSEN *et al.*, 1984), in which the pressure is coupled to a pressure bath and the volume is periodically rescaled and the Anderson barostat (ANDERSEN, 1980), which serves as basis for other barostating methods such as the ones developed by Hoover (HOOVER, 1985), Martina-Tobias-Klein (MARTYNA; TOBIAS; KLEIN, 1994) and Parrinello-Rahman (PARRINELLO; RAHMAN, 1981). The Andersen's idea was couple the system to a fictitious pressure bath and incorporate the volume into the phase space as an additional degree of freedom (TUCKERMAN, 2010). As in the Nosé-Hoover thermostat, Andersen added terms into the Hamiltonian in order to control the variable of interest:

$$\mathcal{H} = \sum_i \frac{V^{-2/3} \pi_i^2}{2m_i} + U(V^{1/3} \mathbf{s}^N) + \frac{p_V^2}{2\mathcal{W}} + PV \quad (3.23)$$

with  $\mathbf{s}$  and  $\pi$  being scale transformations:

$$\mathbf{s}_i = V^{-1/3} \mathbf{r}_i \quad (3.24)$$

$$\pi_i = V^{1/3} p_i \quad (3.25)$$

Here,  $p_V$  is the momentum conjugate to the volume and  $\mathcal{W}$  is a mass parameter that determines the time scale of the volume motion. With the equations above, we can derive the equations of motion in Cartesian coordinates for a constant pressure ensemble:

$$\frac{dr_i}{dt} = \frac{p_i}{m_i} + \frac{1}{3} \frac{dV}{dt} \frac{r_i}{V} \quad (3.26)$$

$$\frac{dp_i}{dt} = -\frac{\partial U}{\partial r_i} - \frac{1}{3} \frac{dV}{dt} \frac{p_i}{V} \quad (3.27)$$

$$\frac{dV_i}{dt} = \frac{p_V}{\mathcal{W}} \quad (3.28)$$

$$\frac{dp_V}{dt} = \frac{1}{3V} \sum_i \left[ \frac{p_i^2}{m_i} - \frac{\partial U}{\partial r_i} \cdot r_i \right] - P \quad (3.29)$$

The equation of motions above are integrated numerically using the methodologies described in the next section.

### 3.1.4 Integration of the motion's equations

With the formalism defined for the equations of motions and for the statistical ensemble, we can then derive discrete-time numerical approximations for them. The basic idea is to solve the trajectory of atoms as function of time ( $r^N(t)$ ) by updating the positions in discrete time intervals or time steps. One of the possible algorithms is The Verlet ([VERLET, 1967](#)). Its proposed equation for the coordinates update is:

$$r(t + \Delta t) = 2r(t) - r(t - \Delta t) + \frac{F(t)}{m} \Delta t^2 + \mathcal{O}(\Delta t^4) \quad (3.30)$$

In this equation, the accuracy is of order  $\mathcal{O}(\Delta t^4)$  and the positions are updated by a time step of  $\Delta t$  by using the positions at the previous two time steps and the forces ( $F$ ) at  $\Delta t$ . The forces acting on every particle are calculated by doing directional derivatives of the intermolecular potential  $U(r)$  in relation to the atoms' positions:

$$\vec{F}(r)_i = -\nabla U(r) \quad (3.31)$$

The intermolecular potential is generally described by a force field. The veloci-

ties of this method can be approximated by:

$$v(t + \Delta t) = \frac{r(t + \Delta t) - r(t - \Delta t)}{2\Delta t} + \mathcal{O}(\Delta t^3) \quad (3.32)$$

The Verlet method doesn't use the velocity directly to update the positions. Hence, the Velocity Verlet algorithm was proposed to serve as a reformulation of the Verlet algorithm that uses the velocity:

$$r(t + \Delta t) = r(t) + v(t)\Delta t + \frac{F(t)}{2m}\Delta t^2 \quad (3.33)$$

The velocity in the equation above is updated following:

$$v(t + \Delta t) = v(t) + \frac{F(t + \Delta t) + F(t)}{2m}\Delta t \quad (3.34)$$

Instead of using a time step of  $\Delta t$ , the velocities can be updated at  $\Delta t/2$ . This is the strategy proposed by the leap frog algorithm:

$$v(t + \Delta t/2) = v(t - \Delta t/2) + \frac{F(t + \Delta t) + F(t)}{m}\Delta t \quad (3.35)$$

$$r(t + \Delta t) = r(t) + v(t + \Delta t/2)\Delta t \quad (3.36)$$

### 3.1.5 Initial Configuration

The equations above require a non overlapping initial positions and velocities for every atom in the system in MD simulations. The initial velocities follow a temperature dependent Maxwell-Boltzmann distribution:

$$\varrho(v_{x,i}) = \frac{m_i}{2\pi k_b T}^{\frac{1}{2}} \exp\left(-\frac{m_i v_{x,i}^2}{2\pi k_b T}\right) \quad (3.37)$$

Random velocities are then found with the equation above for each of the  $3N$

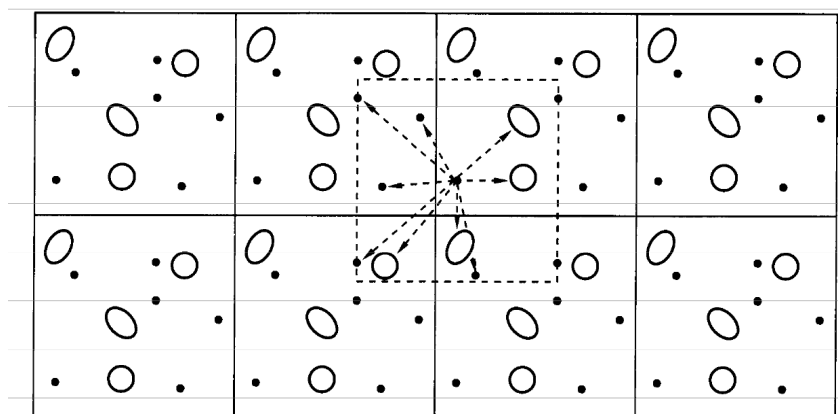


Figure 3.1.1 – Periodic boundary condition representation. Taken from [Frenkel and Smit \(2001\)](#)

components of the velocity. Meanwhile, the initial positions can be obtained by several approaches. The initial configuration can be taken from x ray or NMR spectroscopy, the atoms can be placed randomly in the simulation volume or the atoms can be placed in idealized or approximate geometries. The generally used method to acquire the configurations places the molecules on a cubic lattice. Independent of the method used, certain restrictions should be applied in the initial configurations in order to carry out molecular simulations. As an example, the cubic lattice has a finite size, but a finite size box would result in simulations dominated by surface effects. To avoid that, we can create a box periodically repeated in all directions by applying the so called Periodic Boundary Conditions (PBC). The periodic box has a primitive cell, which contains the system  $N$  particles, replicated in periodic lattice of infinite cells as represented in Figure 3.1.1 (FRENKEL; SMIT, 2001).

### 3.1.6 Force Fields

Force fields are models used to describe structural characteristics such as van der Waals interactions, bond lengths, bond angles and torsion. The description is done by approximating the potential energy function ( $U(r^N)$ ).  $U(r^N)$  has contributions due to intermolecular and intramolecular interactions. The intramolecular interactions include bond stretching, bond angle bending and bond torsion. The contribution to the bond stretching is usually given by the following Taylor expansion around the energy

minimum:

$$u_{bs}(d) = k_{bs}(d - d_0)^2 \quad (3.38)$$

Here,  $d$  is the bond length,  $d_0$  is the equilibrium bond length and  $k_{bs}$  is bond stretching constant. The bond angle bending contribution corresponds to deviations from the preferred geometry, and is given by:

$$u_{ab}(\theta) = k_{ab}(\theta - \theta_0)^2 \quad (3.39)$$

where  $k_{ab}$  and  $\theta_0$  are constants defined by the force field and  $\theta$  is the bond angle between three atoms. The bond torsion interactions corresponds to the energies of rotations along bonds and it happens among four atoms:

$$u_{bt}(\omega) = \sum_{n=0}^N c_n \cos(\omega)^n \quad (3.40)$$

where  $N$  is the number of terms,  $c_n$  is the summation index defined by the force field and  $\omega$  is the torsional angle defined by the force field.

The intermolecular interactions include electrostatics interactions, van der Waal interactions and volume repulsions. The electrostatics interactions of two atoms  $i$  and  $j$  with partial charges follow the Coulomb's Law:

$$u_q(r_{ij}) = \frac{q_i q_j}{4\pi\epsilon_0 r_{ij}} \quad (3.41)$$

In the equation above,  $q_i$  and  $q_j$  are the partial charges and  $\epsilon_0$  is the free space permittivity constant. In many force fields, the van der Waal interactions and volume repulsions between particles  $i$  and  $j$  are modeled in the same equation by the Lennard Jones Potential:

$$u_{LJ}(r_{ij}) = 4\epsilon \left[ \left( \frac{\sigma}{r} \right)^{12} - \left( \frac{\sigma}{r} \right)^6 \right] \quad (3.42)$$

where  $r$  is the distance the molecules,  $\epsilon$  is the depth of the potential well,  $\sigma$  is the distance

correspondent to a zero intermolecular potential. The graphical representation of the Lennard Jones potential is:

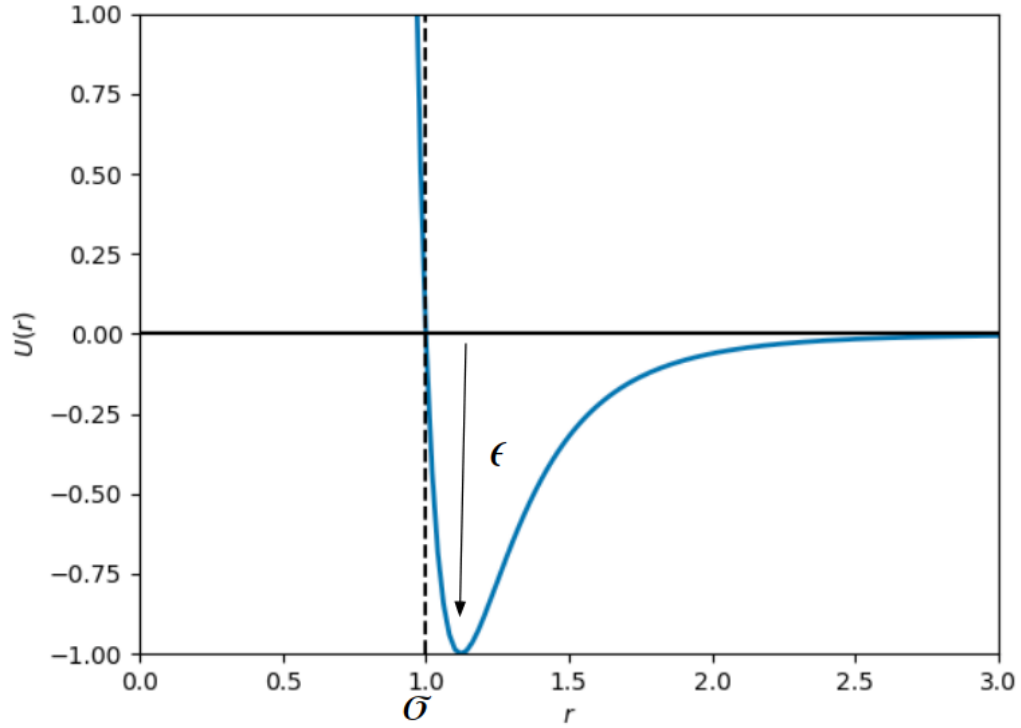


Figure 3.1.2 – Lennard Jones potential representation.

The interactions in Figure 3.1.2 tend to zero after a certain value of  $r$ , so this value can be set as the cutoff radius in which the potential energy is considered to be zero after it. Also, only interactions with the nearest periodic image of the cell are considered for short range interactions (Minimum image convention condition). With this conditions, the calculations of forces and velocities are viable.

The final potential energy function defined by the force field can then be expressed by summing all the interactions above:

$$U(r^N) = u_{bs}(d) + u_{ab}(\theta) + u_{bt}(\omega) + u_q(r_{ij}) + u_{LJ}(r_{ij}) \quad (3.43)$$

## 3.2 SAFT- $\gamma$ Mie Force Field

### 3.2.1 SAFT-VR Mie EoS

The SAFT-VR Mie equation of state (LAFITTE *et al.*, 2013) is the basis for the SAFT- $\gamma$  Mie coarse grained force field (AVENDAÑO *et al.*, 2011). This EoS was initially developed to describe chain molecule formed from fused Mie segments using the Mie attractive and repulsive potential. The Mie potential is a type of generalized Lennard-Jones potential that can be used to explicitly describe repulsive interactions of different hardness/softness and attractive interactions of different ranges, and is given by:

$$U_{Mie}(r) = \epsilon \frac{\lambda_r}{\lambda_r - \lambda_a} \left( \frac{\lambda_r}{\lambda_a} \right)^{\left( \frac{\lambda_a}{\lambda_r - \lambda_a} \right)} \left[ \left( \frac{\sigma}{r} \right)^{\lambda_r} - \left( \frac{\sigma}{r} \right)^{\lambda_a} \right] \quad (3.44)$$

where  $\lambda_r$  is the repulsive exponent and  $\lambda_a$  is the attractive exponent. This equation uses the Barker and Henderson (1976) high perturbation expansion of the Helmholtz free energy up to third order and an improved expression for the radial distribution function (RDF) of Mie monomers at contact to obtain an equation able to give an accurate theoretical description of the vapor-liquid equilibrium and second derivative properties (LAFITTE *et al.*, 2013). For a non-associating fluid, the Helmholtz free energy is:

$$\frac{A}{N\kappa_b T} = a = a^{IDEAL} + a^{MONO} + a^{CHAIN} \quad (3.45)$$

#### 3.2.1.1 Ideal Contribution

The ideal contribution for a mixture is given by:

$$a^{IDEAL} = \sum_{i=1}^{N_c} x_i \ln (\rho_i \Lambda_i^3) - 1 \quad (3.46)$$

where  $x_i = N_i/N$  is the molar fraction of component  $i$ ,  $\rho_i = N_i/V$  is the number density,  $N_i$  is the number of molecules of each component and  $\Lambda_i^3$  is the de Broglie wavelength.



### 3.2.1.2 Monomer Contribution

The monomer contribution describes interactions between Mie segments and can be expressed, for a mixture, as:

$$a^{MONO} = \left( \sum_{i=1}^{N_c} x_i m_{s,i} \right) a^M \quad (3.47)$$

In the equation above,  $m_{s,i}$  is the number of spherical segments making up the molecule  $i$  and  $a^M$  is the monomer dimensionless Helmholtz free energy and it is expressed as a third order perturbation expansion in the inverse temperature (BARKER; HENDERSON, 1976):

$$a^M = a^{HS} + \beta a_1 + \beta a_2^2 + \beta a_3^3 \quad (3.48)$$

where  $\beta = \kappa_b T$  and  $a^{HS}$  is the hard-sphere dimensionless Helmholtz free energy for a mixture :

$$a^{HS} = \frac{6}{\pi \rho_s} \left[ \left( \frac{\zeta_2^3}{\zeta_3^2} - \zeta_0 \right) \ln(1 - \zeta_3) + \frac{3\zeta_1 \zeta_2}{1 - \zeta_3} + \frac{\zeta_2^3}{\zeta_3(1 - \zeta_3)^2} \right] \quad (3.49)$$

The variable  $\rho_s = \rho \sum_i^{N_c} x_i m_{s,i}$  is the total number density of spherical segments and  $\zeta_l$  are the moments of the number density:

$$\zeta_l = \frac{\pi \rho_s}{6} \left( \sum_{i=1}^{N_c} x_{s,i} d_{ii}^l \right), l = 0, 1, 2, 3 \quad (3.50)$$

where  $x_{s,i}$  is the mole fraction of segments and is related through the mole fraction of component  $i$  ( $x_i$ ) by:

$$x_{s,i} = \frac{m_{s,i} x_i}{\sum_{k=1}^{N_c} m_{s,k} x_k} \quad (3.51)$$

The effective hard-sphere diameter  $d_{ii}$  for the segments is:

$$d_{ii} = \int_0^{\sigma_{ii}} (1 - \exp(-\beta U_{ii}^{Mie}(r))) dr \quad (3.52)$$

The integral in Eq. (3.52) is normally obtained by means of Gauss-Legendre with a 5-point quadrature (PAPAIOANNOU *et al.*, 2014). The detailing of terms of Eq. (3.47)

can be found in [Lafitte \*et al.\* \(2013\)](#).

### 3.2.1.3 Chain Contribution

The chain formation of  $m_s$  tangentially bonded Mie segments contribution is based on the first-order perturbation theory (TPT1) ([PAPAIOANNOU \*et al.\*, 2014](#)) and can be expressed as:

$$a^{CHAIN} = - \sum_{i=1}^{N_c} x_i (m_{s,i} - 1) \ln(g_{ii}^{Mie}(\sigma_{ii})) \quad (3.53)$$

The  $g_{ij}^{Mie}(\sigma_{ij})$  term correspond to the radial distribution function (RDF) of the hypothetical Mie system evaluated at the effective diameter and can be obtained with the perturbation expansion:

$$g_{ij}^{Mie}(\sigma_{ij}) = g_{d,ij}^{HS}(\sigma_{ij}) \exp[\beta \epsilon g_{1,ij}(\sigma_{ij}) / g_{d,ij}^{HS}(\sigma_{ij}) + (\beta \epsilon)^2 g_{2,ij}(\sigma_{ij}) / g_{d,ij}^{HS}(\sigma_{ij})] \quad (3.54)$$

The other terms in the equations above are explicitly exposed in the original article ([LAFITTE \*et al.\*, 2013](#)).

### 3.2.1.4 Ring Contribution

There are two forms for the Helmholtz free energy for rings formed from  $m_s$  tangentially bonded segments in the literature. The first one ([LAFITTE \*et al.\*, 2012](#)) considered that the difference between a chain and a ring molecule is that the latter has one more bond that is connecting the first segment to the last. With this assumption, Eq. (3.53) can be adapted to rings by:

$$a^{RING} = - \sum_{i=1}^{N_c} x_i m_{s,i} \ln(g_{ii}^{Mie}(\sigma_{ii})) \quad (3.55)$$

According to [Lafitte \*et al.\* \(2012\)](#), Eq. (3.55) needs an additional parameterization with molecular simulation data so the EoS can be used in molecular simulations, but this procedure is not necessary for chain molecules. Recently, [Müller and Mejía \(2017\)](#)

tried to correct this inconsistency by means of developing the ring free energy based on the work of [Müller and Gubbins \(1993\)](#), who obtained rigorous expressions for hard fluids with molecular geometries of rings of  $m_s = 3$ . The final expression developed for the ring dimensionless Helmholtz free energy is:

$$a^{RING} = - \sum_{i=1}^{N_c} x_i (m_{s,i} - 1 + \chi_i \eta_i) \ln(g_{ii}^{Mie}(\sigma_{ii})) \quad (3.56)$$

$\eta_i = m_{s,i} \rho_i \sigma_{ii}^3 / 6$  is the packing fraction and  $\chi_i$  is a parameter which depends on  $m_{s,i}$  and on the geometry of the ring of each component  $i$ . For a value of  $\chi = 0$ , Eq. (3.56) is equal to Eq. (3.53). Meanwhile, the equation corresponds to a hard sphere system of triangles when  $\chi = 1.3827$ . [Müller and Mejía \(2017\)](#) also calculated values of  $\zeta$  for  $m_s = 3, m_s = 4, m_s = 5, m_s = 7$  with pseudo-experimental data from molecular dynamics (MD) for a defined pure fluid. Values of  $\chi$  for some of the geometry estimated can be seen in [Figure 3.2.1](#).

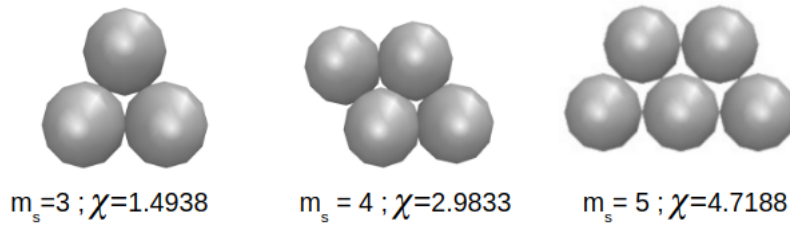


Figure 3.2.1 – Values for parameter  $\chi$  according to the ring geometry. Adapted from [Müller and Mejía \(2017\)](#).

### 3.2.1.5 Combining rules for the intermolecular potential parameters

[Lafitte et al. \(2013\)](#) also suggested mixing rules for the potential parameters based on Lorentz-Berthelot combining rules ([ROWLINSON; SWINTON, 1982](#)):

$$\sigma_{ij} = \frac{\sigma_{ii} + \sigma_{jj}}{2} \quad (3.57)$$

$$\lambda_{k,ij} - 3 = \sqrt{(\lambda_{k,ii} - 3)(\lambda_{k,jj} - 3)}, k = r, a \quad (3.58)$$

$$\epsilon_{ij} = (1 - k_{ij}) \frac{\sqrt{\sigma_{ii}^3 \sigma_{jj}^3}}{\sigma_{ij}^3} \sqrt{\epsilon_{ii} \epsilon_{jj}} \quad (3.59)$$

The  $k_{ij}$  is a binary interaction parameter to correct the deviations of the Lorentz-Berthelot rule for chemically distinct compounds. This parameter can be fitted to experimental data or pseudo experimental data.

### 3.2.2 Parameter Estimation for the SAFT- $\gamma$ Mie Force Field

The SAFT- $\gamma$  Mie Force Field uses a coarse graining top down methodology in its parameterization. This methodology aims to obtain the intermolecular parameters from macroscopic experimental data such as fluid-phase equilibrium or interfacial tension data. The idea is that the force field parameters estimated with the SAFT-VR Mie EoS can be used on molecular simulations since both the equation of state and the force field use the same explicit intermolecular potential model (Mie potential). This correspondence between models has already been seen for a variety of fluids in which this force field was parameterized. This success in the representation of the properties of real fluids can be imputed to the degrees of freedom of Mie Potential ([HERDES; TOTTON; MÜLLER, 2015](#)). Furthermore, this flexibility provides the exploration of a very large parameter space without using an iterative simulation scheme ([AVENDAÑO \*et al.\*, 2011](#)).

Each substance has initially five parameters to be estimated ( $m_s, \sigma, \epsilon, \lambda_r$  and  $\lambda_a$ ) according to Eq. (3.44). The number of segments are usually fixed in an integer value since each segment represents one pseudo atom. The attractive parameter is generally fixed due to its high correlation with the repulsive parameter. Usually, the parameter is fixed in the London value of 6, which is a good representation of the dispersion scale of most simple fluids that don't have strong polar interactions ([RAMRATTAN \*et al.\*, 2015](#); [HERDES; TOTTON; MÜLLER, 2015](#)). There are two strategies to obtain the parameters: one is by fitting the Saft-Vr Mie EoS to experimental data as vapor pressure and liquid density and the other one is using correspondent state parametrization. The

first, generally, minimizes the following unweighted least-squares objective function:

$$\min_{\sigma, \epsilon, \lambda_r} F_{obj}(\sigma, \epsilon, \lambda_r) = \sum_{i=1}^{N_p} \left( \frac{P_v^{SAFT}(T_i, \sigma, \epsilon, \lambda_r) - P_v^{exp}(T_i)}{P_v^{exp}(T_i)} \right)^2 + \sum_{i=1}^{N_p} \left( \frac{\rho_l^{SAFT}(T_i, \sigma, \epsilon, \lambda_r) - \rho_l^{exp}(T_i)}{\rho_l^{exp}(T_i)} \right)^2 \quad (3.60)$$

where  $N_p$  is the number of experimental points,  $P_v$  is the vapor pressure and  $\rho_l$  is the saturated liquid density. Another properties that can be used in the estimation are superficial tension and speed of sound. The multiple parameters of the model make it necessary the use of a wide range of experimental data since multiple solutions may be found for the fit. Therefore, one needs to be careful in deciding the level of coarse graining (i.e. the parameter  $m_s$ ) and the subsequent parameter space that will not result in some physical inconsistencies such as a premature freezing fluid.

[Lafitte et al. \(2012\)](#) suggested that two corrections factors ( $c_\sigma$  and  $c_\epsilon$ ) should be estimated with simulation data when using Eq. (3.55) for the ring contribution. They are related to the EoS parameters by scaled parameters:

$$\sigma^{scaled} = c_\sigma \sigma^{SAFT} \quad (3.61)$$

$$\epsilon^{scaled} = c_\epsilon \epsilon^{SAFT} \quad (3.62)$$

According to [Lafitte et al. \(2012\)](#), these corrections are necessary because the approximations employed in the EoS theory generate discrepancies between molecular simulations and the EoS for ring molecules modeled with Eq. (3.55). The objective

function for this estimation is given by:

$$\min_{c_\sigma, c_\epsilon} F_{obj}(c_\sigma, c_\epsilon) = \sum_{i=1}^{N_p} \left( \frac{P_v^{sim}(T_i, \sigma^{SAFT}, \epsilon^{SAFT}) - P_v^{SAFT}(T_i, \sigma^{scaled}, \epsilon^{scaled})}{P_v^{sim}(T_i, \sigma^{SAFT}, \epsilon^{SAFT})} \right)^2 + \sum_{i=1}^{N_p} \left( \frac{\rho_{liq}^{sim}(T_i, \sigma^{SAFT}, \epsilon^{SAFT}) - \rho_{liq}^{SAFT}(T_i, \sigma^{scaled}, \epsilon^{scaled})}{\rho_{liq}^{sim}(T_i, \sigma^{SAFT}, \epsilon^{SAFT})} \right)^2 \quad (3.63)$$

The repulsive parameter is maintained in the value found on the minimization of Eq. (3.60). The refined values for  $\sigma$  and  $\epsilon$  are:

$$\sigma^{sim} = \sigma^{SAFT} / c_\sigma \quad (3.64)$$

$$\epsilon^{sim} = \epsilon^{SAFT} / c_\epsilon \quad (3.65)$$

It is interesting to point out that this new parameterization is not necessary when using Eq. (3.56) as the ring contribution. The other method to obtain the force field parameters is the correspondent state parametrization (MEJÍA; HERDES; MÜLLER, 2014). This method considers that the unweighted volume average of the attractive contribution to the Mie intermolecular potential,  $a_1$ , is a mean field approximation:

$$a_1 = 2\pi\rho\sigma^3\epsilon\alpha \quad (3.66)$$

The van der Waals constant,  $\alpha$ , considering  $\lambda_a = 6$  is related by the Mie exponents by:

$$\alpha = \frac{1}{\epsilon\sigma^3} \int_{\sigma}^{\infty} \phi(r)r^2 dr = \frac{\lambda_r}{3(\lambda_r - 3)} \left( \frac{\lambda_r}{6} \right)^{6/(\lambda_r - 6)} \quad (3.67)$$

The parameterization in this method starts by using the experimental acentric factor,  $\omega$ , for each molecule with a fixed value of  $m_s$  to obtain the value of the repulsive

exponent with the following Padé series:

$$\lambda_r = \frac{\sum_{i=0} a_i \omega^i}{1 + \sum_{i=1} b_i \omega^i} \quad (3.68)$$

$a_i$  and  $b_i$  are dependent parameters of the number of segments and a table with their values is presented in the original paper (MEJÍA; HERDES; MÜLLER, 2014). The van der Waals constant can be found substituting  $\lambda_r$  into Eq. (3.67). The reduced critical potential  $T_c^*$  is related to  $\alpha$  by a Padé series:

$$T_c^* = \frac{\sum_{i=0} c_i \alpha^i}{1 + \sum_{i=1} d_i \alpha^i} \quad (3.69)$$

The values of  $c_i$  and  $d_i$  are also available in the original paper. The reduced temperature of the equation above is used in conjunction with the experimental critical temperature,  $T_c$ , to find the energy parameter with the relation below:

$$T_c^* = \frac{\kappa_b T_c}{\epsilon} \quad (3.70)$$

The diameter parameter, however, is not obtained with the critical properties, but with the reduced liquid density,  $\rho_{T_r=0.7}$ , at the reduced temperature,  $T_r$ , of 0.7. This density is also obtained with a Padé series using parameters by Mejía, Herdes and Müller (2014):

$$\rho_{T_r=0.7}^* = \frac{\sum_{i=0} j_i \alpha^i}{1 + \sum_{i=1} k_i \alpha^i} \quad (3.71)$$

The relation among the equation above,  $\sigma$  and the experimental density is given by:

$$\rho_{T_r=0.7}^* = \rho_{T_r=0.7} \sigma^3 N_{av} \quad (3.72)$$

where  $N_{av}$  is The Avogadro number. This correspondent state method has the advantage

of only requiring critical data, which is available for a great range of fluids, and liquid density data. The parameters found with this strategy are available at an online database (ERVIK; MEJÍA; MÜLLER, 2016).

The binary interaction parameter  $k_{ij}$  of Eq. (3.59) is necessary to adjust the mixture behavior of chemically distinct components. Normally, it is estimated minimizing the difference between experimental binary vapor liquid equilibrium or interfacial tension data and the SAFT-VR Mie EoS output data (MÜLLER; MEJÍA, 2017; LOBANOVA *et al.*, 2016). The objective function is similar to:

$$\min_{k_{ij}} F_{obj}(k_{ij}) = \sum_{k=1}^{N_p} \left( \frac{P_v^{SAFT}(T_k, x, k_{ij}) - P_v^{exp}(T_k, x)}{P_v^{exp}(T_k, x)} \right)^2 + \sum_{k=1}^{N_p} \left( \frac{\rho_l^{SAFT}(T_k, x, k_{ij}) - \rho_l^{exp}(T_i)}{\rho_l^{exp}(T_i)} \right)^2 \quad (3.73)$$

However, Ervik *et al.* (2016) used molecular simulation results to fit the parameter to the superficial tension data. The strategy followed by them was to do simulations in three values of  $k_{ij}$  first and, after, they refined the parameter until a value in good agreement with the experimental data was found.

### 3.3 Solvation Free Energy Simulations Based on Molecular Dynamics

Free energies can be expressed as averages over ensembles of atomic configurations generated using Monte Carlo or molecular dynamics techniques. In the canonical ensemble, the free energy is given by:

$$F(N, V, T) = -\kappa_b T \ln Q(N, V, T) \quad (3.74)$$



Remembering that  $Q(N, V, T)$  is the partition function of the canonical ensemble:

$$Q(N, V, T) = \int d^N p d^N r \exp \left[ -\beta \left( \sum_{i=1}^N \frac{p_i^2}{2m_i} + U(r_1, \dots, r_n) \right) \right] \quad (3.75)$$

Meanwhile, the average over the isothermal-isobaric ensemble gives the Gibbs free energy:

$$G(N, P, T) = -\kappa_b T \ln \Delta(N, P, T) \quad (3.76)$$

where  $\Delta(N, P, T)$  is the partition function of the isothermal-isobaric ensemble:

$$\Delta(N, P, T) = \frac{1}{V_0} \int_0^\infty dV \int d^N p d^N r \exp \left[ -\beta \left( \sum_{i=1}^N \frac{p_i^2}{2m_i} + U(r_1, \dots, r_n) + PV(r_1, \dots, r_n) \right) \right] \quad (3.77)$$

Evaluating the partition function is a difficult task, but we are interested in calculating only the Gibbs free energy difference between two states of a system, that is given by:

$$\Delta G_{AB} = G_B - G_A = -\kappa_b T \ln \left( \frac{\Delta_B}{\Delta_A} \right) \quad (3.78)$$

Since the masses of particles in systems 0 and 1 are the same, the moment integrals in the ratio  $\Delta_B/\Delta_A$  can be simplified into to the ratio of the configuration integrals:

$$\frac{Z_B}{Z_A} = \frac{\int_0^\infty dV \int d^N r \exp [-\beta (U(r_1, \dots, r_n) + PV(r_1, \dots, r_n))]_B}{\int_0^\infty dV \int d^N r \exp [-\beta (U(r_1, \dots, r_n) + PV(r_1, \dots, r_n))]_A} \quad (3.79)$$

What results in the following equation for the Gibbs free energy difference that

doesn't require the calculation of the partition function at each state:

$$\Delta G_{AB} = G_B - G_A = -\kappa_b T \ln \left( \frac{Z_B}{Z_A} \right) \quad (3.80)$$

The Gibbs free energy difference between end states  $A$  and  $B$  are, more specifically, the difference between the solute alone in the gas phase and the solute interacting with the solvent. In order to have accurate results for free energy differences, the states' phase integral must have sufficient overlap (KLIMOVICH; SHIRTS; MOBLEY, 2015). This can be achieved by calculating the free energy difference between a series of intermediates states. The result of these differences are independent of the path chosen since free energy is a state function. That's why alchemical states (no physical sense) are used to link physical states of interest. The solvation free energy calculations are done through a thermodynamic cycle to gradually insert the solute molecule into the solvent as illustrated in Figure 3.3.1. According to this cycle, the free energy of solvation is expressed as:

$$\Delta G_{solv} = \Delta G_{1 \rightarrow 4} = \Delta G_{1 \rightarrow 2} + \Delta G_{2 \rightarrow 3} + \Delta G_{3 \rightarrow 4} \quad (3.81)$$

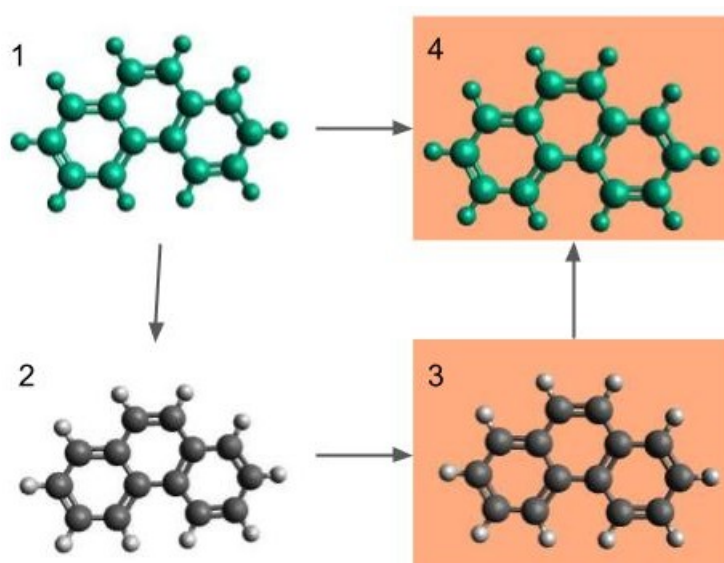


Figure 3.3.1 – Thermodynamic cycle for solvation free energy calculations with molecular dynamics (Adapted from Klimovich, Shirts and Mobley (2015))

The solvation free energy between states 1 and 2 in [Figure 3.3.1](#) is associated with turning off the molecule's non bonded interactions in the gas phase. The following transformation,  $\Delta G_{2 \rightarrow 3}$ , is the free energy of moving the non-interacting molecule in the gas phase to the solvent, and is equal to zero since the transformation of a non-interacting molecule doesn't depend on the environment. Lastly,  $\Delta G_{3 \rightarrow 4}$  is the free energy required to the non-interaction molecule in the aqueous phase regain its non-bonded interactions. The solvation free energy calculation can be classified according to the types of non bonded interactions that are turned off in the  $1 \rightarrow 2$  and  $3 \rightarrow 4$  parts of the cycle. If both non-bonded interactions with the environment and internal interactions are turned off, this is an annihilation free energy calculation. Meanwhile, if only non-bonded interactions with the environment are turned off, this is a decoupling free energy calculation. In the later case,  $\Delta G_{1 \rightarrow 2} = 0$  and the  $\Delta G_{solv} = \Delta G_{3 \rightarrow 4}$ . The methods used to carry out these transformations scale the solute charges to zero and then turn off the interactions corresponding to the Lennard Jones potential. In order to carry out the later process, a modified potential with a coupling parameter( $\lambda$ ) is used. Each  $\lambda$  represent an alchemical state and, when  $\lambda = 0$ , there is no interaction with the solvent and, when  $\lambda = 1$ , interactions are fully activated. The coupling of the  $\lambda$  parameter could be linear, but it could generate numerical problems related to the exponential part of the potential. That's why the non-linear soft-core scheme ([BEUTLER et al., 1994](#)) is used to make the potential behave more smoothly in relation to the change of  $\lambda$  as can be seem in [Figure 3.3.2](#). The generalized soft core potential is given by:

$$U^{sc}(r) = \lambda \epsilon \frac{\lambda_r}{\lambda_r - \lambda_a} \left( \frac{\lambda_r}{\lambda_a} \right)^{\left( \frac{\lambda_a}{\lambda_r - \lambda_a} \right)} \left\{ \frac{1}{[\alpha(1 - \lambda) + (r/\sigma)^{\lambda_a}]^{\lambda_r/\lambda_a}} - \frac{1}{\alpha(1 - \lambda) + (r/\sigma)^{\lambda_a}} \right\} \quad (3.82)$$

where  $\alpha$  is a constant which the value of 0.5 is normally assumed to it,  $r$  is the distance the molecules,  $\epsilon$  is the depth of the potential well,  $\sigma$  is the distance correspondent to a zero intermolecular potential,  $\lambda_r$  is the repulsive exponent and  $\lambda_a$  is the attractive

exponent. Using the Lennard Jones exponents ( $\lambda_r = 12$  and  $\lambda_a = 6$ ), Eq. (3.82) becomes:

$$U_{LJ}^{sc}(r) = 4\lambda\epsilon \left\{ \frac{1}{[\alpha(1-\lambda) + (r/\sigma)^6]^2} - \frac{1}{\alpha(1-\lambda) + (r/\sigma)^6} \right\} \quad (3.83)$$

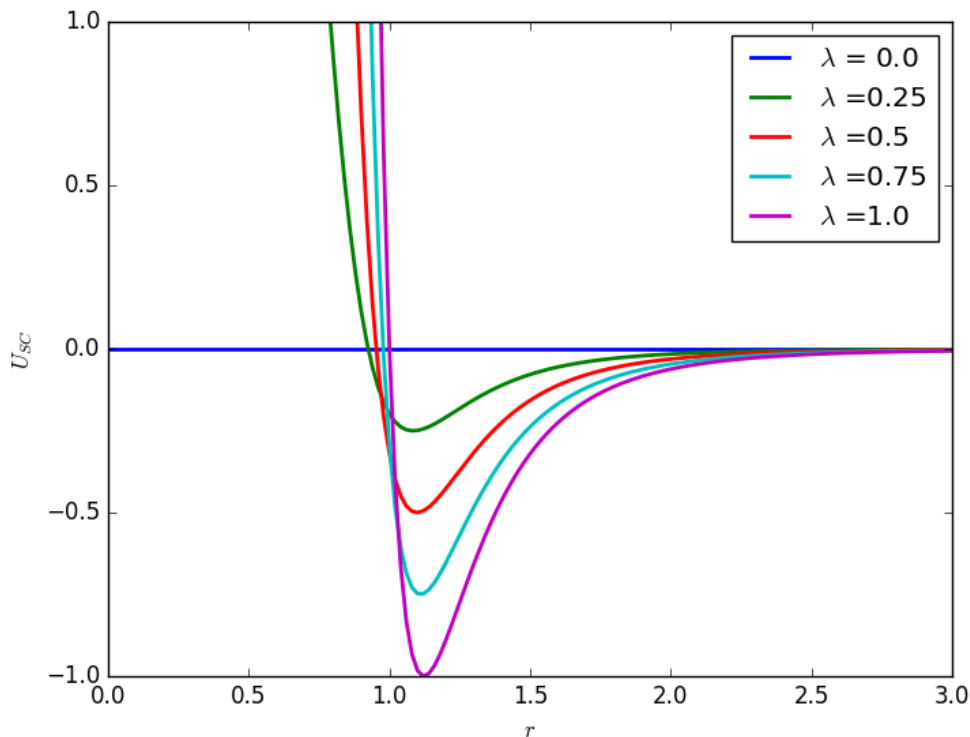


Figure 3.3.2 – Soft-core potential in reduced units.

The  $\Delta G_{3 \rightarrow 4}$  can be then obtained by doing independent simulations in different values of  $\lambda$  or by doing expanded ensemble simulations (LYUBARTSEV *et al.*, 1992), which samples all states in a single simulation. This method allows a faster sampling across the alchemical states, provided that the kinetic barriers are not substantial. The free energies of solvation obtained can then be used to calculate other properties such as the partition coefficient, that is a measure of the partitioning of one solute in two solvents (a and b) with different physicochemical characteristics at a temperature T:

$$\log P^{a/b} = \frac{\Delta G_{solv}^a - \Delta G_{solv}^b}{2.303RT} \quad (3.84)$$

### 3.4 Multistate Bennet Acceptance Ratio (MBAR)

The MBAR method is a free energy of perturbation based method, the MBAR is equal to the BAR method when the calculations are made between only two states. It proposes an estimator that computes free energies and their uncertainties of all  $K$  states by minimizing the  $K \times K$  matrix of variances simultaneously for a simulation with  $N_j$  uncorrelated samples in equilibrium. For each of the  $x_{i,n=1}^{N_i}$  configurations of  $i$ , the following probability distributions is sampled:

$$p_i(x) = \frac{q_i(x)}{c_i} \quad (3.85)$$

$$c_i = \int dx q_i(x) \quad (3.86)$$

where  $q_i(x) = \exp(-u_i(x))$  and  $u_i$  is the potential energy of each state, defined by  $u_i = \beta[U_i(x) + P_i V(x) + \mu_i^T n(x)]$ . Meanwhile,  $c_i$  is normalization constant. The free energies are estimated with the ratio of this constant in each state:

$$\Delta f_{ij} = f_i - f_j = -\ln \frac{c_j}{c_i} = -\ln \frac{\int dx q_j(x)}{\int dx q_i(x)} \quad (3.87)$$

[Shirts and Chodera \(2008\)](#) then proposed the following arbitrary function:

$$c_i \langle \alpha_{ij} q_j \rangle_i = c_j \langle \alpha_{ij} q_i \rangle_j \quad (3.88)$$

Using the above equation for every state  $K$ , the relation is obtained:

$$\sum_{j=1}^K \frac{\hat{c}_i}{N_i} \sum_{n=1}^{N_i} \alpha_{ij} q_j(x_{i,n}) = \sum_{j=1}^K \frac{\hat{c}_j}{N_j} \sum_{n=1}^{N_j} \alpha_{ij} q_i(x_{j,n}) \quad (3.89)$$

[Shirts and Chodera \(2008\)](#) suggested the following equation for the arbitrary

term  $\alpha_{ij}$  in order to decrease the variance:

$$\alpha_{ij}(x) = \frac{N_j \hat{c}_i^{-1}}{\sum_{k=1}^K N_k c_i^{-1} q_k(x)} \quad (3.90)$$

Assuming the sampling is carried out following Boltzmann statistics, Eqs. (3.89) and (3.90) can be rearranged to obtain the free energy estimator, which is solved self consistently:

$$f_i = \frac{1}{\beta} \ln \sum_{k=1}^K \sum_{n=1}^{N_k} \frac{\exp[-\beta u_i(x_{kn})]}{\sum_{l=1}^K N_l \exp[\beta(f_l - u_l(x_{kn}))]} \quad (3.91)$$

The equation above requires the evaluation of the potential energy of uncorrelated configuration  $n$  for all  $K$  states ( $u_i(x_{kn})$ ) and for all uncorrelated configuration snapshots ( $N_k$ ) from state  $k$ . Free energy changes between states are then:

$$\Delta f_{ij} = f_j - f_i \quad (3.92)$$

The statistical variance resulting from free energy estimation  $S_{ij}^2 \Delta f_{ij}$  is given by the matrix covariances:

$$s_{ij}^2 \Delta f_{ij} \equiv \text{cov}(-\ln \hat{Z}_j / \hat{Z}_i, -\ln \hat{Z}_j / \hat{Z}_i) \quad (3.93)$$

where  $\hat{Z}_j$  and  $\hat{Z}_i$  are the partition functions of states  $i$  and  $j$ . The MBAR method can be considered as limit case of the Weighted Histogram Analysis Method (WHAM) (KUMAR *et al.*, 1992) for computing free energies. Eq. (3.91) becomes equal to the WHAM equations if the histogram width tends to zero. Despite this, the MBAR is still more suited than the WHAM because it doesn't have the bias associated with the discretization, allows the calculation of an error estimate and allows free energy calculations of states that weren't sampled (SHIRTS; CHODERA, 2008).

### 3.5 Expanded Ensemble Method

Instead of doing various simulations in different values of  $\lambda$ , expanded ensemble simulations (LYUBARTSEV *et al.*, 1992) were developed to allow a non-Boltzmann sampling scheme of different states in only one simulation. In this scheme, the sampling is done by biasing the phase space exploration process with weights not related to the statistical ensemble. The statistical expanded ensemble,  $Z^{EE}$ , is obtained from the probability distributions correspondent to each  $\lambda$ , hence  $Z^{EE}$  is defined as a sum of sub ensembles  $Z_i$  in different values of  $\lambda$ :

$$Z^{EE} = \sum_{i=1}^N Z_i(\lambda_i) \exp(\eta_i) \quad (3.94)$$

where  $N$  is the number of alchemical states,  $\eta_i$  is the arbitrary weight of the sub ensemble at each state and  $Z_i$  is configuration partition function at state  $i$ . For the isothermal-isobaric ensemble,  $Z$  is:

$$Z = \int_0^\infty dV \int d^n r \exp [-\beta (U(\lambda, r_1, \dots, r_n) + PV(r_1, \dots, r_n))] \quad (3.95)$$

In solvation free energy calculations with molecular dynamics,  $\lambda$  corresponds to the coupling parameter of the soft-core potential (Eq. 3.82). For molecular dynamic simulations, the sampling of the expanded ensemble is done by performing an arbitrary number of MD steps followed by a  $\lambda$  transition. Chodera and Shirts (2011) proved that type of sampling of the expanded ensemble is similar to the Gibbs sampling method (GEMAN; GEMAN, 1984; LIU, 2002). Following the Gibbs method, the sampling of the configuration space  $x$  for one state  $\lambda_k$  during the MD steps is done by using the conditional distribution:

$$\pi(x|\lambda_k) = \frac{\exp[-\beta u(x, \lambda_k)]}{\int dx \exp[-\beta u(x, \lambda_k)]} \quad (3.96)$$

Meanwhile, the state transition in the MD simulation uses the following condi-

tional distribution:

$$\pi(\lambda_k|x) = \frac{\exp[-\beta u(x, \lambda_k) + \eta_k]}{\sum_{k=1}^K \exp[-\beta u(x, \lambda_k) + \eta_k]} \quad (3.97)$$

where  $u(x, \lambda_k) = U(x, \lambda_k) + PV(x, \lambda_k)$  is the reduced potential function for the NPT ensemble. There are a variety of acceptance schemes to do the expanded sampling using Eq. (3.97), but [Chodera and Shirts \(2011\)](#) suggested that the independence sampling ([LIU, 2002](#)) is the best strategy to increase the number of uncorrelated configurations. The implementation suggested by them updates the state index from  $i$  to  $j$  by first generating a uniform random number  $R$  on the interval  $[0, 1)$  and then selecting the smallest new value of  $j$  that satisfies the relation below:

$$R < \sum_{i=1}^j \pi(\lambda_i|x) \quad (3.98)$$

The sampling strategy above depends on the weights in order to assure an adequate sampling of the states. If there isn't a sufficient number of states sampled, the expanded ensemble becomes deficient in obtaining input data to estimate free energy differences with the methods exposed in Chapter 2. The weights can be calculated following the flat-histogram approach ([BERG; NEUHAUS, 1992](#); [LEE, 1993](#); [DAYAL \*et al.\*, 2004](#)). This strategy aims to obtain adequate sampling by assuring that all the states have an equal number of samples, i.e. the ratio of the probability of sampling state ( $\pi_i$ ) to the probability of sampling state  $j$  ( $\pi_j$ ) is equal to one. Given that  $\pi_i$  has the following equation:

$$\pi_i = \frac{Z_i(\lambda_i) \exp(\eta_i)}{Z^{EE}} \quad (3.99)$$

and using Eqs. 3.80 and 3.79, the following relation can be obtained for  $\pi_i/\pi_j = 1$ :

$$(\eta_i - \eta_j) = \beta(G_i - G_j) \quad (3.100)$$



Eq. (3.100) is solved iteratively with trial simulations. For the first simulation, the values of  $\eta$  are chosen or set to zero and the histogram of the states visited is obtained. With this histogram, it is possible to estimate the free energy differences and, since the weights are related to the free energies by Eq. (3.100), the next values of  $\eta$  can be calculated. This iteration goes on until a uniform distribution is secured. The weights found are then used in a longer simulation to obtain the final solvation free energy differences.

The choice of the  $\lambda$  set correspondent to overlapping alchemical states are crucial to acquire accurate energy differences. In this work, the method chosen to obtain the optimal stage of the  $\lambda$  domain is the one developed by Escobedo and Martinez-Veracoechea (2007) with basis in the study of Trebst, Huse and Troyer (2004). This method targets "bottlenecks" in the simulation. It does that by optimizing  $\lambda$  through the minimization of the number of round trips per CPU time between the lowest  $\lambda$  ( $= 0$ ) and highest  $\lambda$  ( $= 1$ ). This is specifically done by maximizing the steady-state stream  $\phi$  of the simulation, which "walks" among the values of  $\lambda$ . This stream is estimated from Fick's diffusion type of law:

$$\phi = D(\Lambda)\Pi(\Lambda)\frac{dx(\Lambda)}{d\Lambda} \quad (3.101)$$

In the equation above,  $\Lambda$  is the actual continue value of the coupling parameter. This continue function of  $\lambda$ s is obtained by interpolating the  $\lambda$  set linearly.  $D(\Lambda)$  is the diffusivity at state  $\Lambda$  and  $x(\Lambda)$  is the fraction of times that the trial simulation at state  $\Lambda_i$  has most recently visited the state  $\lambda = 1$  as opposed to state  $\lambda = 0$ . The derivative  $dx(\Lambda)/d\Lambda$  is approximated with the central finite differences method. Finally,  $\Pi(\Lambda)$  is the probability of visiting  $\Lambda$ :

$$\Pi(\Lambda) = \frac{C'\bar{\Pi}(\lambda)}{\Lambda_{i+1} - \Lambda_i} \quad (3.102)$$

The  $C'$  term in the equation above represents a constant and  $\bar{\Pi}(\lambda)$  is the arithmetic

average of visiting the  $\Lambda$  states:

$$\bar{\Pi}(\lambda) = \frac{\pi_{i+1} - \pi_i}{2} \quad (3.103)$$

The  $\phi$  is maximum when the probability  $\Pi'(\Lambda_i)$  is proportional to  $1/\sqrt{D(\Lambda)}$ . With that information, it is possible to estimate the diffusivity using one trial simulation with the following equation:

$$D(\Lambda) = \frac{\Lambda_{i+1} - \Lambda_i}{\bar{\Pi}(\lambda) dx(\Lambda)/d\Lambda} \quad (3.104)$$

Hence, we can calculate  $\bar{\Pi}$  and, consequently, the cumulative probability, which is used to obtain the new  $\lambda$  states:

$$\Phi = \int_{\lambda=0}^{\lambda=1} \Pi'(\Lambda_i) d\Lambda = \frac{i}{K} \quad (3.105)$$

where,  $K$  is the total number of  $\lambda$  states.

### 3.6 Gibbs Ensemble Monte Carlo (GEMC)

The Monte Carlo (MC) approach is another method for generating atomic trajectories in order to obtain macroscopic properties. The trajectories are obtained stochastically, unlike the molecular dynamics approach. The positions are evolved by random moves (MC steps) or perturbations obtained with the Metropolis method ([Metropolis et al., 1953](#)), hence the trajectories are not predictable from the set of initial positions. The Metropolis method is a Markov process, that is a stochastic process in which the configurations change randomly with time and have no memories of the previous configurations. The random move is constructed in such way that the probability of visiting a particular point  $r^N$  is proportional to the Boltzmann factor ( $\exp[-\beta U(r^N)]$ ) ([FRENKEL; SMIT, 2001](#)). The construction of a particle displacement MC step according to [Metropolis et al. \(1953\)](#) can be briefly summed up in:

1. Pick a random particle, and calculate its energy  $U(r^N)$ .
2. Perturb the particle by randomly displacing its configuration,  $r' = r + \Delta$ . Where  $\Delta$  is a perturbation chosen from a defined interval of maximum displacement  $([-\delta_{max}, \delta_{max}])$ . Calculate the energy with the new positions  $U(r'^N)$ .
3. Accept the move from  $r^N$  to  $r'^N$  with the probability:

$$acc_{A \rightarrow B} = \min(1, \exp[-\beta U(r'^N) + \beta U(r^N)]) \quad (3.106)$$

The values of maximum displacement are defined in order to obtain acceptance rates of 25-50 % in the step 3 (FRENKEL, 2013). Monte Carlo simulations are interesting when we need to calculate properties in different thermodynamic ensembles, such as the Gibbs Ensemble (PANAGIOTOPOULOS, 1987). This ensemble is used to study phase coexistence with simultaneous Monte Carlo (MC) simulations of two boxes, representing a two phase system, with periodic conditions. The boxes exchange molecules, energy and volume between them. Equilibrium is obtained through MC steps that consist of translation and rotation moves, volume exchange moves and randomly exchanges of molecules between the boxes. For the phase equilibrium of multi-component systems, the GEMC simulations should be carried out at the NPT (constant number of particles, pressure and temperature) ensemble to obey the requirement of an additional degree of freedom for mixtures. Meanwhile, the simulation of single component systems is carried out at constant number of particles, temperature and volume (NVT) since the two phase region would be a line for this system at constant pressure and temperature. The constant volume GEMC ensemble is rigorously equivalent to the canonical ensemble in the thermodynamic limit as demonstrated by Frenkel and Smit (2001). The partition function of the GEMC-NVT ensemble is obtained considering that the particles in both boxes are subjected to the same intermolecular interactions. Also, the boxes' volumes and number of particles ( $N_1, N_2, V_1$  and  $V_2$ ) can vary while the total volume ( $V$ )

and total number of particles ( $N$ ) remain constant ( $N = N_1 + N_2, V = V_1 + V_2$ ):

$$Q(NVT) \equiv \sum_{N_1}^N \frac{1}{V \Lambda^{3N} N_1! (N - N_1)!} \int_0^V dV_1 V_1^{N_1} V_2^{N_2} \int dx_1^{N_1} \exp[-\beta U(x_1^{N_1})] \int dx_2^{N_2} \exp[-\beta U(x_2^{N_2})] \quad (3.107)$$

In order to define the acceptance rules for the MC moves and compute any property of interest, it is necessary to know the probability of finding the configuration with  $N_1$  particles in box 1 with volume  $V_1$  and positions  $x_1^{N_1}$  and  $x_2^{N_2}$ . This probability is given by:

$$\pi(x_1^{N_1}, x_2^{N_2}, N_1, N_2, V_1, V_2) \propto \frac{V_1^{N_1} V_2^{N_2}}{N_1! N_2!} \exp[-\beta U(x_1^{N_1}) - \beta U(x_2^{N_2})] \quad (3.108)$$

The acceptance criterion for the translation and rotation moves of configuration A to B is similar to the conventional NVT MC ensembles and is equal to:

$$acc_{A \rightarrow B} = \min(1, \exp[-\beta U(x_A^{N_1}) - \beta U(x_B^{N_1})]) \quad (3.109)$$

The exchange volume moves happen by exchanging an amount  $\Delta V$  between the boxes to achieve pressure equilibrium.  $\Delta V$  can be chosen from a uniform distribution based on the maximum variation of volume defined ( $\delta V_{max}$ ) with probability  $1/\delta V_{max}$ . The acceptance rule for these moves is:

$$acc_{A \rightarrow B} = \min \left( 1, \left( \frac{V_1^B}{V_1^A} \right)^{N_1-1} \left( \frac{V_2^B}{V_2^A} \right)^{N_2+1} \exp[-\beta U(x_A^N) - \beta U(x_B^N)] \right) \quad (3.110)$$

Particle exchange moves are carried out to obtain the equality of chemical potential between the boxes. One particle from one box is removed and then added to a

random location in the other box. The criteria to accept or reject this type of move is:

$$acc_{A \rightarrow B} = \min \left( 1, \frac{N_1 V_2}{N_2 V_1} \exp[-\beta U(x_A^N) - \beta U(x_B^N)] \right) \quad (3.111)$$

This method has been widely used to calculate phase equilibrium, but it underperforms for the region near the critical point due to large density fluctuations. The GEMC also has a poor performance for dense systems since the particle exchange moves have a low acceptance ratio.

# 4 Methodology

## 4.1 Phenanthrene Parameterization

The two parameterization strategies for ring molecules described in section 3.2.2 were implemented for phenanthrene. For both of them, only vapor pressure data (MORTIMER; MURPHY, 1923) were used due to the unavailability of saturated liquid density. The attractive parameter,  $\lambda_a$ , was set to six to avoid correlation with the repulsive parameter. The parameterization with the ring equation of Müller and Mejía (2017) was done with the number of segments fixed in 5 since this level of coarse graining was also used for the similar molecule anthracene:

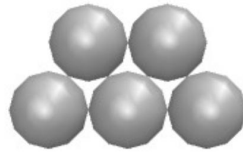


Figure 4.1.1 – Geometry for  $m_s = 5$

The minimization was done using the Particle Swarm Optimization (PSO) method with the following objective function:

$$\min_{\sigma, \epsilon, \lambda_r} F_{obj}(\sigma, \epsilon, \lambda_r) = \sum_{i=1}^{N_p} \left( \frac{P_v^{SAFT}(T_i, \sigma, \epsilon, \lambda_r) - P_v^{exp}(T_i)}{P_v^{exp}(T_i)} \right)^2 \quad (4.1)$$

$P_v^{exp}$  is the experimental vapor pressure and  $P_v^{SAFT}$  is the vapor pressure obtained with SAFT-VR Mie EoS. We used the routine proposed by Smith, Ness and Abbot (2007) routine to calculate the bubble point with the EoS. The resulting parameters  $\sigma$ ,  $\epsilon$  and  $\lambda_r$  of Eq. (4.1) are the final force field parameters used in molecular simulations.

The parameterization with the Lafitte *et al.* (2012) ring equation was done with  $m_s = 3$  so every bead would represent one ring:

The first part of the estimation followed the same procedure described above

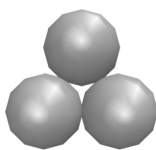


Figure 4.1.2 – Geometry for  $m_s = 3$

for the Müller and Mejía (2017) equation. As explained in section 3.2.2, the Lafitte *et al.* (2012) equation requires the estimation of correction factors  $c_\sigma$  and  $c_\epsilon$  (Eqs. (3.61) and (3.62)). The PSO method was used with Eq. (3.63). In this equation, the vapor pressures and saturated liquid densities from molecular simulations were obtained using the Gibbs Ensemble Monte Carlo method on the NVT ensemble (section 3.6).

The boxes for the GEMC-NVT simulations were generated inserting 400 molecules on the liquid box and 100 on the vapor one using the Packmol package (MARTÍNEZ *et al.*, 2009). Initial densities of each box were equal to the saturated densities found with the SAFT-VR Mie Eos in order to avoid the migration of all molecules to a single phase throughout the simulation. Simulations had equilibration and production times of  $10^4$  and  $510^4$  MC cycles respectively. Each MC cycle corresponded to  $10^3$  rotation trials,  $10^3$  translation trials,  $10^2$  molecule insertion trials,  $10^2$  molecule deletion trials and 10 volume exchange trials. The cut off distance was equal to  $20\hat{A}$  without long range interactions. The saturated vapor density ( $\rho_{vap}$ ), the saturated liquid density ( $\rho_{liq}$ ) and the vapor pressure ( $P_v$ ) were sampled at each 100 MC cycles and this data were divided in five blocks to calculate the averages and standard deviations. With the correction factors found after the estimations, we calculated the  $\sigma$  and  $\epsilon$  parameters with Eqs. (3.64) and (3.65).

## 4.2 Solvation Free Energy Calculations

Molecular dynamic simulations to estimate the free energy differences with the SAFT- $\gamma$  Mie force field were performed using the Lammmps package (PLIMPTON, 1995). The motion equations were integrated with the velocity-Verlet algorithm (VERLET, 1967) with a time step of 1 fs. As required by the coarse grained model, molecules were

treated as rigid bodies. The thermostat and the barostat were the Nose/Hoover with chains with a damping factors of 100 and 1000 fs respectively. Electrostatics interactions are not explicitly accounted by the SAFT- $\gamma$  Mie force field, hence there were no shifting of forces or long range corrections. The potential cutoff was equal to 20 Å (MÜLLER; MEJÍA, 2017) with a neighbor skin of 2 Å. The initial configurations of the solvated systems were generated with the Packmol package (MARTÍNEZ *et al.*, 2009). For the binary mixtures, one molecule of solute and a varying number of solvent molecules - 700 molecules for toluene and octanol, 1024 for hexane, 3000 for water - were randomly added to a cubic box. The simulations to study solvation free energy of phenanthrene in a mixture of toluene and carbon dioxide were done with different weight fractions of carbon dioxide. The system consisted of one molecule of phenanthrene for all the fractions and 123 molecules of  $CO_2$  and 618 molecules of toluene for  $w_{CO_2} = 0.087$ ; 166 molecules of  $CO_2$ ; 589 molecules of toluene for  $w_{CO_2} = 0.119$ ; 232 molecules of  $CO_2$  and 545 molecules of toluene for  $w_{CO_2} = 0.169$  and 380 molecules of  $CO_2$  and 446 molecules of toluene for  $w_{CO_2} = 0.289$ .

All simulations were carried out maintaining the temperature and pressure constant at 298 K and 1 bar, except the ones containing carbon dioxide. These had the temperature of 298 K and the pressure of the liquid phase equilibrium correspondent to the  $CO_2$  fraction (CHANG, 1992). For all the simulations, the initial box was equilibrated at the NPT ensemble for 2 ns and then the resulting configurations were used as the initial configuration of the expanded ensemble simulations. These were carried out with the Lammmps user package for expanded ensemble simulations with the Mie Potential developed by our group, available at <https://github.com/atoms-ufrrj/USER-ALCHEMICAL>. The sampling of a new state was tried at every 10 MD steps. In order to define the optimal values of  $\lambda$  and  $\eta$  related to each state, short trials simulations, having around 9 ns of production time, were carried out. In the first simulation, the group of  $\lambda$  for all the pairs solvent-solute was: (0.0,0.15,0.2,0.25,0.3,0.4,0.45,0.5,0.55,0.7,0.9,1.0) and the  $\eta$ s were set to zero or were given the values of the ones found for similar pairs solute-solvent. The subsequent group of  $\eta$  were estimated with the flat histogram



approach (Eq. (3.100)). We then did another trial simulation with the new weights. The results of this simulation were used to optimize the group of  $\lambda$ s by minimizing the number of round trips, as described in section 3.5. The  $\eta$ s correspondent to the newest group of  $\lambda$ s were interpolated linearly from the free energy differences. With the final values of  $\eta$  and  $\lambda$  defined for each mixture, larger simulations with a production time of 20 ns were carried out.

Since the force field considers that the beads don't have charges, there is no coulombic interaction and Eq. (3.81) becomes equal to  $\Delta G_{3 \rightarrow 4}$ . The post processing method used to calculate free energy differences was the Multisate Bennet Acceptance Ratio (MBAR) described in section 3.4. The software alchemical-analysis (KLIMOVICH; SHIRTS; MOBLEY, 2015) was used to obtain the  $\Delta G_{solv}$  with MBAR and to assess the quality of the results. We only estimated the binary interaction parameter of Eq. (3.59) for pairs with water as a solvent. The estimation was done by performing trial expanded ensemble simulations in three values of  $k_{ij}$ . With the  $\Delta G_{solv}$  obtained with these simulations, we did a linear fit to obtain the refined value of the parameter. We used this strategy because the estimation with SAFT VR Mie EoS gave poor results for the free energy.

# 5 Results and Discussion

## 5.1 Solvation free energies

The first part of this work consisted of obtaining phenanthrene parameters for the SAFT- $\gamma$  Mie Force Field, as described in section 4.1, since the parameters were not available for the ring geometry on the force field database. The parameters obtained and the mean percentage error (MPE) to the experimental data were:

Table 1 – Estimated SAFT- $\gamma$  Mie Force Field parameters for phenanthrene

$m_s$	$\epsilon/k_B$ (K)	$\sigma$ (Å)	$\lambda_r$	MPE(%)
3 (LAFITTE <i>et al.</i> , 2012)	485.55	4.197	14.34	1.64   9.74
5 (MÜLLER; MEJÍA, 2017)	262.74	4.077	9.55	0.88

In the table above, the first value of MPE for the Lafitte *et al.* (2012) strategy corresponds to the estimation with experimental data and the second corresponds to the corrections factors estimation with MD data. This strategy has an inconsistency of requiring two estimations because parameters solely estimated with the EoS aren't accurate for molecular simulation. Hence, the solvation free energy of phenanthrene was only studied with the set of parameters estimated with Müller and Mejía (2017) strategy. In fact, the (LAFITTE *et al.*, 2012) strategy was only followed because it was the only one available when we first started this work. The sets of parameters for the other compounds were retrieved from the literature (LOBANOVA *et al.*, 2016; HERDES; TOTTON; MÜLLER, 2015; ERVIK; MEJÍA; MÜLLER, 2016; MÜLLER; MEJÍA, 2017):

The solvation free energies of aromatic solutes in nonpolar (hexane), aromatic (toluene) and hydrogen bonding (1-octanol) solvents were examined with binary interaction parameters equal to zero. Since the force field doesn't account for charges, the solvation free energy is equal to the Mie contribution ( Eq. (3.82)). A total of 15-18, depending on the pairs solute-solvent,  $\lambda_s$  and their respective  $\eta_s$  were estimated as described in the methodology. The final  $\lambda$  set was found using the cumulative probability

Table 2 – SAFT- $\gamma$  Mie Force Field for each substance used in this work

	$m_s$	$\epsilon/k_B$ (K)	$\sigma(\text{\AA})$	$\lambda_r$
Water	1	305.21	2.902	8.0
Propane	1	426.08	4.871	34.29
Carbon dioxide	2	194.94	2.848	14.65
Hexane	2	376.35	4.508	19.57
Octanol	3	495.71	4.341	28.79
Toluene	3	268.24	3.685	11.80
Benzene	3	230.30	3.441	10.45
Pyrene	4	459.04	4.134	15.79
Anthracene	5	259.68	3.631	9.55

distribution (Eq. (3.105)) for all pairs. The distribution for the pair hexane+benzene can be seen in Figure 5.1.1 and the optimized values of  $\lambda$  and  $\eta$  in Table 3. The  $\lambda_s$  and  $\eta_s$  for the other pairs are available at Appendix A. The coupling parameters are concentrated on the region with a steeper slope for all the pairs as it was expected.

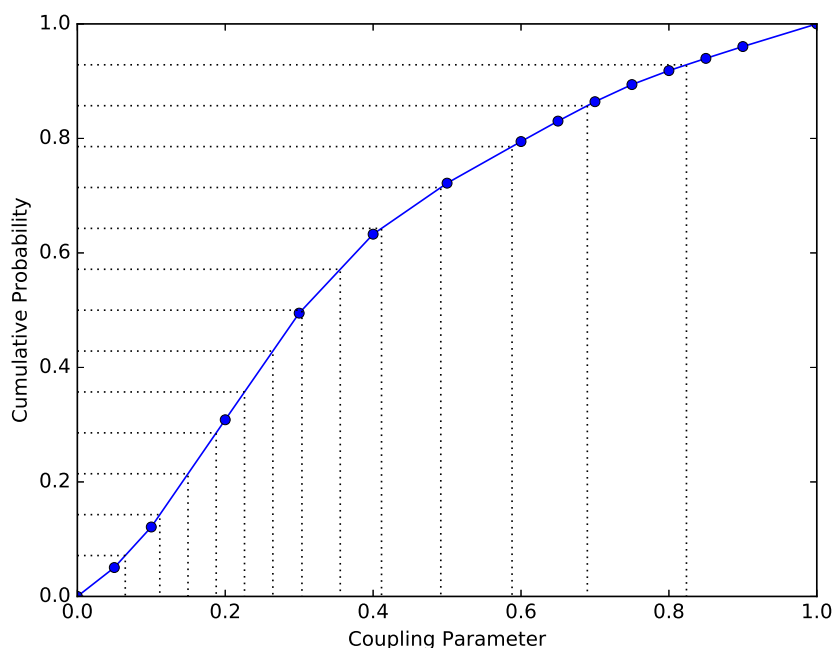


Figure 5.1.1 – Cumulative probability

It is also important to analyze the reliability of solvation free energy estimations through the overlapping of the intermediate states found with the optimization above. Insufficient overlap among states when using a FEP based such MBAR may result in the underestimation of variance, and, consequently, in substantially incorrect free energies. The overlapping matrix for the solvation free energy of benzene in hexane is

Table 3 – Optimized values of  $\lambda$  and  $\eta$  for the pair benzene + hexane

$\lambda$	$\eta$
0	0
0.065	0.708
0.112	1.385
0.15	1.892
0.188	2.399
0.226	2.519
0.264	2.457
0.304	2.367
0.356	1.921
0.411	1.411
0.492	0.524
0.588	-0.663
0.69	-2.016
0.824	-3.922
1	-6.583

presented in [Figure 5.1.2](#) and the matrices for the other pairs are available at Appendix B. The elements of these matrices are the probabilities of observing a sample from state  $i$  in state  $j$ . As an example, the probability of observing state 6 in a simulation of state 8 is 0.16 in [Figure 5.1.2](#). It can be observed in the figures that the matrices for all the pairs in this work have more than three diagonals. In addition to that, the probabilities in the three main diagonals are higher than 0.03, which indicates that the free energy estimations are reliable ([KLIMOVICH; SHIRTS; MOBLEY, 2015](#)). After this analysis, we present the results of solvation free energies obtained using the optimized coupling parameters and their weights and absolute deviations to experimental data in [Table 4](#).

$\lambda$	0	1	2	3	4	5	6	7	8	9	10	11	12	13	14
0	.42	.29	.16	.08	.03	.01	.01								
1	.33	.27	.18	.10	.06	.03	.02	.01							
2	.23	.23	.18	.12	.09	.06	.04	.02	.01	.01					
3	.14	.16	.16	.13	.11	.10	.08	.06	.03	.02	.01				
4	.06	.09	.11	.11	.12	.12	.13	.11	.07	.04	.02	.01	.01		
5	.02	.03	.05	.07	.09	.12	.16	.16	.12	.08	.05	.02	.01	.01	
6		.01	.02	.03	.06	.09	.15	.18	.16	.12	.08	.04	.02	.01	
7			.01	.02	.03	.07	.13	.17	.18	.16	.11	.07	.04	.02	.01
8				.01	.02	.04	.09	.14	.17	.18	.15	.10	.06	.03	.01
9					.01	.02	.06	.11	.15	.18	.17	.13	.09	.05	.02
10						.01	.04	.07	.11	.16	.18	.17	.14	.08	.03
11						.01	.02	.04	.08	.12	.17	.19	.19	.14	.06
12							.01	.02	.05	.08	.13	.18	.22	.19	.11
13							.01	.01	.03	.05	.09	.15	.22	.25	.19
14								.01	.01	.03	.06	.11	.19	.29	.30

Figure 5.1.2 – Overlapping matrix for hexane+benzene.

Table 4 – Calculated and experimental values for the solvation free energy differences (kcal/mol) of solutes in non aqueous solvents

Solvent	Solute	$\Delta G_{solv}^{exp}$	$\Delta G_{solv}^{Mie}$	Absolute Deviation
hexane	benzene	-3.96	$-3.76 \pm 0.01$	0.20
hexane	pyrene	-11.53	$-10.82 \pm 0.02$	0.71
hexane	phenanthrene	-10.01	$-9.16 \pm 0.01$	0.85
1-octanol	propane	-1.32	$-1.36 \pm 0.02$	0.04
1-octanol	anthracene	-11.72	$-8.16 \pm 0.03$	3.61
1-octanol	phenanthrene	-10.22	$-8.34 \pm 0.03$	1.47
toluene	pyrene	-12.86	$-11.74 \pm 0.01$	1.11
toluene	anthracene	-11.31	$-9.90 \pm 0.01$	1.41

The numerical values for solvation free energies estimated in Table 4 had smaller absolute deviations to experimental data, what shows that the SAFT- $\gamma$  Mie force field performs better for a non polar solvent. Additionally, this force field presented better

results for the pair hexane+benzene than the Trappe force field (GARRIDO *et al.*, 2011) and ELBA coarse grained force field (GENHEDEN, 2016). We also observed the effect of molecule's size on the entropic region of the free energy curve in Figure 5.1.3. It was expected that a force field based on an EoS that doesn't explicitly account for hydrogen bond would not perform well for 1-octanol. Despite this, the solvation free energies of propane and phenanthrene in 1-octanol stayed in the desired deviation range of 1-2 kcal/mol (MOBLEY; GILSON, 2017). The solvation free energy absolute deviation for propane was much smaller when compared to the other solutes and when compared to the prediction of the ELBA force field (GENHEDEN, 2016). This can be attributed to propane's non polarity and smoother free energy curve (Figure 5.1.4) and higher degrees of freedom provided by the Mie Potential. The anthracene and phenanthrene molecules have the same geometry in the model and similar physical properties, but the absolute deviation of the solvation free energy of anthracene in 1-octanol is much higher than the one of phenanthrene 1-octanol. This may indicate a problem in the parameterization of anthracene.

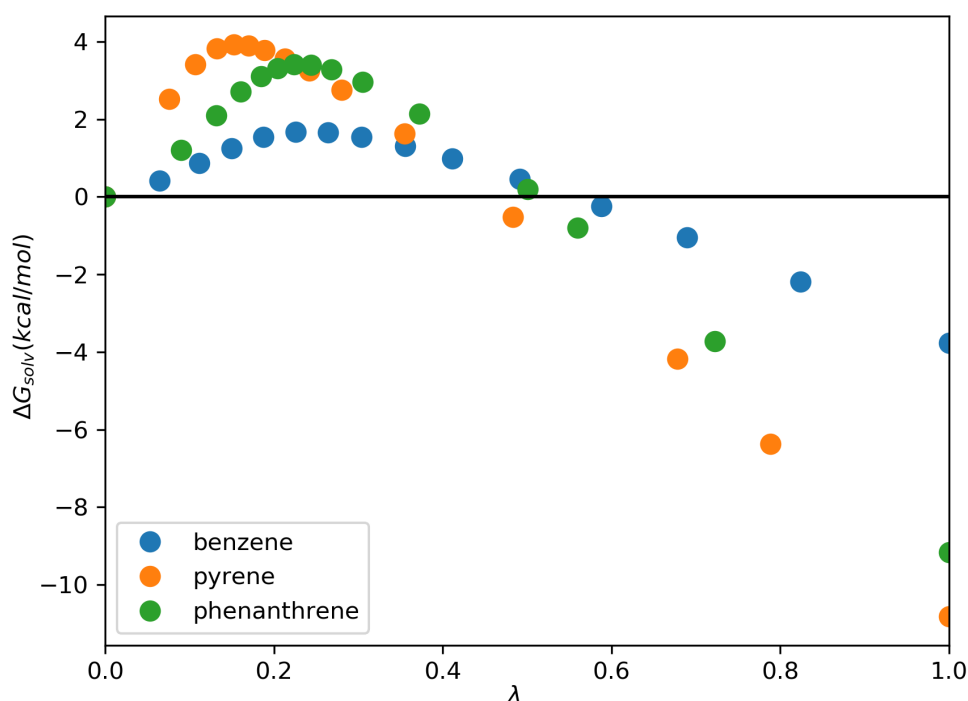


Figure 5.1.3 – Solvation free energy profiles of different solutes in hexane.

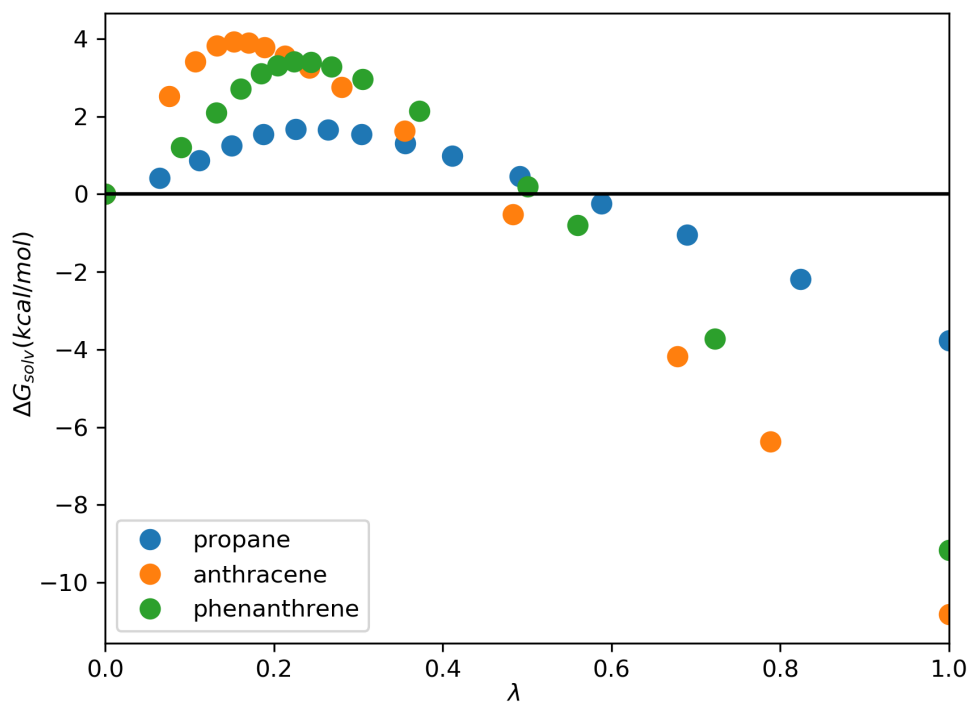


Figure 5.1.4 – Solvation free energy profiles of different solutes in 1-octanol.

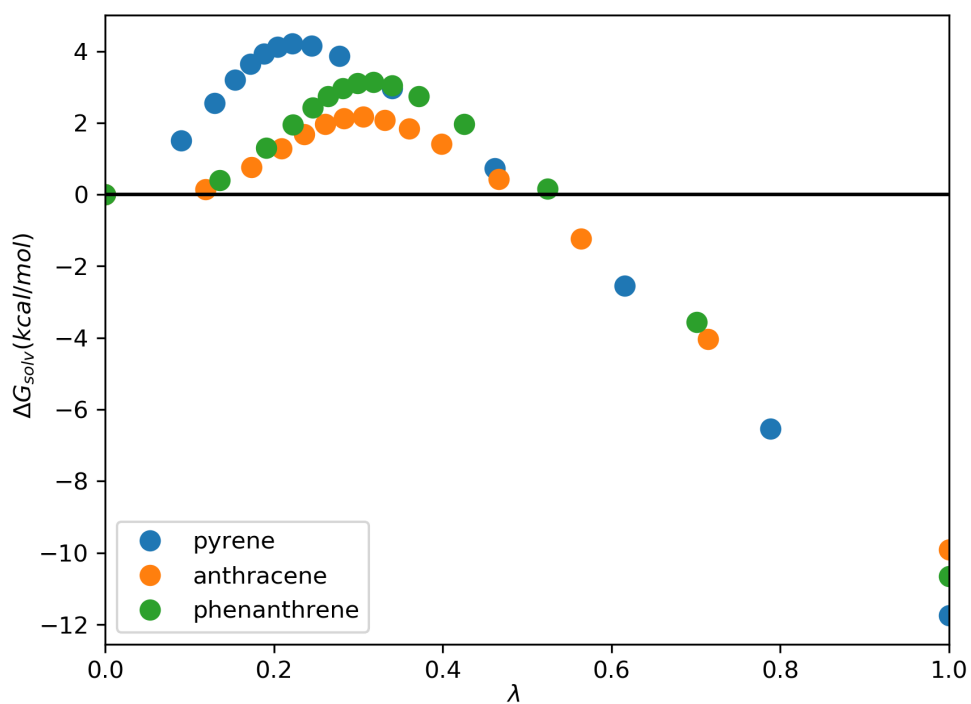


Figure 5.1.5 – Solvation free energy profiles of different solutes in toluene.

The results also indicated the prediction capability of the force field for pairs of aromatic solute and solvent. The influence of the molecule's geometry on free energy curves (Figure 5.1.5) was also observed for these pairs.  $\Delta G_{solv}$  was calculated too for phenanthrene in toluene and in toluene+ $CO_2$ . To the best of our knowledge, there was no available experimental data for these solvation free energies, but the previous results for phenanthrene in other solvents and for the pair anthracene+toluene showed that the force field is adequate to describe the solvation phenomenon of phenanthrene in an aromatic solvent. The results for these sets are exposed below:

Table 5 – Calculated values for the solvation free energy differences (kcal/mol) of phenanthrene in toluene+ $CO_2$ .

$w_{CO_2}$	$\Delta G_{solv}^{Mie}$
0.0	$-10.65 \pm 0.02$
0.087	$-10.73 \pm 0.02$
0.119	$-10.78 \pm 0.02$
0.169	$-10.71 \pm 0.02$
0.289	$-10.69 \pm 0.02$

The increasing of  $CO_2$  mass fraction in toluene caused a small effect on solvation free energies. First, the  $\Delta G_{solv}$  decreased with the increase of  $w_{CO_2}$ , indicating a higher solubility. From the 0.169 fraction, the effect was reversed and carbon dioxide became an anti solvent. It was observed that asphaltene precipitation occurs when carbon dioxide mass fractions became higher than 0.10 in the system asphaltene+toluene+carbon dioxide (SOROUSH *et al.*, 2014), what is in accordance with the anti solvent effect of carbon dioxide observed on the calculated values. It is also important to point out that the small differences observed in the free energy profiles (Figure 5.1.6) may indicate the non-influence of  $CO_2$  in solvation of phenanthrene in toluene when using the Saft- $\gamma$  Mie force field. But, since this is a qualitative study due the lack of this system experimental data, more studies need to be done in order to make a secure assertion about it.



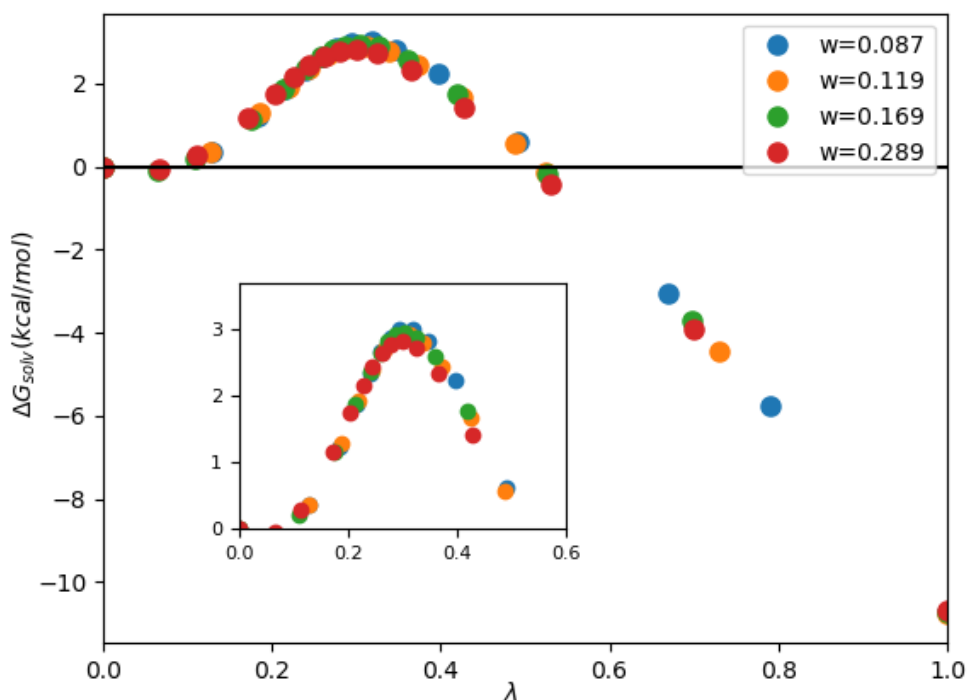


Figure 5.1.6 – Solvation free energy profiles of phenanthrene in toluene+ $CO_2$ .

## 5.2 Hydration free energies

The hydration free energies of widely studied solutes (propane, benzene) and aromatic solutes (toluene, phenanthrene) were calculated with a group of fifteen intermediate states. First, the binary interaction parameter was set to zero, but the results obtained deviated a lot from the experimental data as can be seen in the table below:

Table 6 – Calculated values for the hydration free energy differences (kcal/mol) of solutes in water for  $k_{ij} = 0$ .

Solute	$\Delta G_{solv}^{exp}$	$\Delta G_{solv}^{Mie}$
propane	$2.00 \pm 0.20$	$1.10 \pm 0.01$
benzene	$-0.86 \pm 0.20$	$-4.45 \pm 0.03$
toluene	$-0.83 \pm 0.20$	$-15.80 \pm 0.06$
phenanthrene	$-3.88 \pm 0.60$	$-10.90 \pm 0.04$

After these results, the need of the binary interaction parameter was clear. The  $k_{ij}$  estimation with the SAFT VR Mie EoS and experimental vapor pressure data also didn't provide good results, then the strategy of estimating the  $k_{ij}$  with the output from

solvation free energy calculations with molecular dynamics was used, as described in the last paragraph of section 4.2. Individual values for the interaction parameter for each solvent was initially found, but, since the parameters values for aromatic solutes were very similar (0.148, 0.162, 0.152), the average of these values was taken in order to obtain a general parameter for the water+aromatic pairs. The parameters estimated are:

Table 7 – Binary interaction parameters employed.

Pair	$k_{ij}$
water + propane	0.067
water + aromatic	0.154

The relatively large  $k_{ij}$  value for the aromatic solutes can be pinned on the lack of an explicit association term on the model and on the water model itself, since the model didn't need a  $k_{ij}$  for mixtures with 1-octanol. Nevertheless, the value obtained by fitting the parameter with molecular dynamics interfacial tension data was larger for the mixture water+toluene (0.241) (HERDES *et al.*, 2017). The SAFT- $\gamma$  Mie model for water (LOBANOVA *et al.*, 2016) has actually two different of temperature dependent sets of parameters. The one used in this work was the set estimated with experimental interfacial tension data, but the binary interaction parameter estimated with MD phenomenon tension data could not be transferable to solvation free energy calculations. Modeling the water with a coarse grained methodology has a lot of difficulties because the water molecules move independently and only have non bonded interactions (HADLEY; MCCABE, 2010; HADLEY; MCCABE, 2012). The SAFT- $\gamma$  Mie water model considers that one water molecule corresponds to one bead, this strategy only saves small simulation time, but it is able to predict properties at physiological temperatures unlike other more aggressive models, which consider that one bead represents various water molecules. In light of all this, the SAFT- $\gamma$  Mie force field appears to be a good alternative when working close to room temperatures, but the necessity of additional parameters estimated with molecular simulation indicates problems on the model. The solvation free energy differences calculated with the final fitted binary interaction parameters are presented in Table 8.

Table 8 – Calculated and experimental values for the hydration free energy differences (kcal/mol) of solutes in water.

Solute	$\Delta G_{solv}^{GAFF}$	$\Delta G_{solv}^{ELBA}$	$\Delta G_{solv}^{exp}$	$\Delta G_{solv}^{Mie}$	Absolute Deviation
propane	$2.50 \pm 0.02$	$2.76 \pm 0.02$	$2.00 \pm 0.20$	$2.01 \pm 0.01$	0.01
benzene	$-0.81 \pm 0.02$	$-0.69 \pm 0.01$	$-0.86 \pm 0.20$	$-1.12 \pm 0.01$	0.26
toluene	$-0.79 \pm 0.03$	$-0.76 \pm 0.01$	$-0.83 \pm 0.20$	$-0.84 \pm 0.01$	0.01
phenanthrene	$-5.26 \pm 0.03$	-	$-3.88 \pm 0.60$	$-3.47 \pm 0.02$	0.41

Hydration free energy differences with  $k_{ij}$  had low absolute deviations to the experimental data, as expected since the parameter was adjusted to fit the data. The root mean square error (RMSE) for the pairs tested with the SAFT- $\gamma$  Mie model was equal to 0.24, meanwhile the RMSE for hydration free energy differences with the GAFF force field (MOBLEY; GUTHRIE, 2014) was 0.73 and for the ELBA coarse grained force field was 0.44 (GENHEDEN, 2016). The difference in absolute deviations between the GAFF and SAFT- $\gamma$  Mie force fields is significantly high for phenanthrene, hence the coarse grained force field with a binary parameter is preferred if the application requires a higher level of accuracy. The ELBA coarse grained force field models three carbons as one Lennard Jones site and models the water molecules as Lennard Jones sites with a point dipole, and it comprises six independent parameters. Despite of the same level of coarse graining (one water molecule is represented by one bead) as the SAFT- $\gamma$  Mie model, the results indicated that the Mie Model with the binary interaction parameter performed better in modeling the solvation phenomenon of the pairs studied in this work and worst with the binary parameter equal to zero. Hence, the choice between the two coarse grained models is dependent on the availability and transferability of binary interaction parameters for the Mie Model. Hydration free energy profiles in Figure 5.2.1 show the geometry dependence on the free energy profiles. We can observe also that the solvation free energy for the first non zero lambda is negative for benzene and toluene, when a positive value is expected. This can be caused by numerical errors or by the force field.

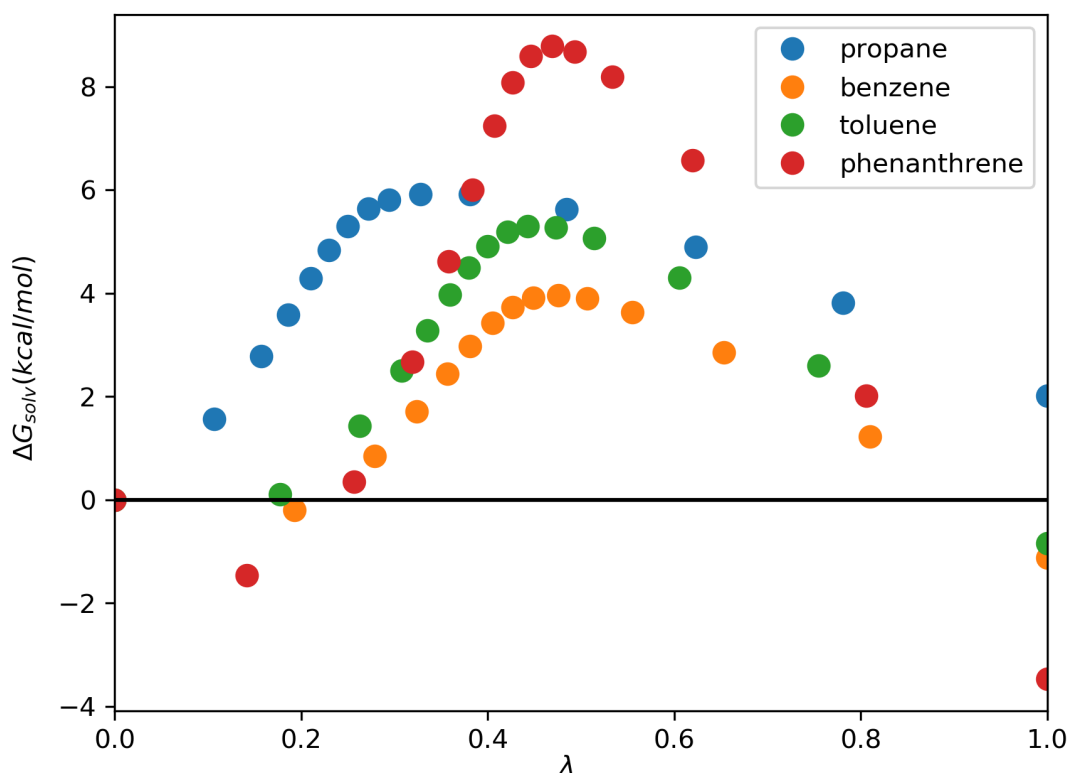


Figure 5.2.1 – Hydration free energy profiles for different solutes.

### 5.3 Partition Coefficients

Using the solvation free energies estimated, we also calculated partition coefficients, Eq. (3.84), for toluene/hexane, water/hexane and water/1-octanol. The later is the one with most experimental data in the literature due to the fact that 1-octanol is a model for biological lipids and different soils and that this partition coefficient is used to quantify hydrophobicity (RUELLE, 2000). The water/hexane partition coefficient is important because hexane is a model for an apolar, hydrophobic phase and the toluene/hexane was calculated because the characterization of asphaltenes by these two solvents. Results and experimental data are shown in Table 9. The experimental data of partition coefficients are usually available for water/1-octanol (POOLE; DURHAM; KIBBEY, 2000; SANGSTER, 1997) and water/hexane (SCHULTE *et al.*, 1998). Since direct experimental data were not available for the partition coefficient of toluene/hexane, we used the solvation free energy experimental data exposed in the section above as an input in Eq. (3.84) to generate estimated experimental data.

Table 9 – Partition Coefficient Calculated from MD simulations and from experimental data.

	Molecular Dynamics	Experimental	Absolute Deviation
	$\log P^{\text{water}/1\text{-octanol}}$		
propane	2.47	2.40	0.07
phenanthrene	3.57	4.46	0.89
	$\log P^{\text{water}/\text{hexane}}$		
benzene	1.93	2.06	0.13
phenanthrene	4.17	4.49	0.32
	$\log P^{\text{toluene}/\text{hexane}}$		
pyrene	-0.67	-0.97	0.30
phenanthrene	-0.47	-	-

Overall absolute deviations were small for pairs with smaller solvation free energy deviations such as propane and benzene. The water/1-octanol partition coefficient of phenanthrene had higher deviation due to the higher deviation of the free energy of solvation of this compound in 1-octanol and the toluene/hexane partition coefficient of pyrene has its high deviation related to the the prediction of the solvation free energy in toluene. Comparing with other force fields, [Garrido \*et al.\* \(2009\)](#) reported average absolute deviations for the water/1-octanol partition coefficient of 0.4 for Gromos, 0.3 for TraPPE and 0.9 for OPLS-AA/TraPPE force fields, and the low deviations of TraPPE are attributed to cancellation of errors between two phases. Additionally, [Genheden \(2016\)](#) found average absolute deviations of 0.86 for the water/hexane partition coefficient and of 0.75 for the water/1-octanol partition coefficient with the ELBA coarse grained force field . Although these papers didn't predict the partition coefficient of phenanthrene and pyrene in the pair of solvents, we can say that the predictions for our small sets of solute-solvent stayed in the same range of absolute deviations than the other force fields. However, a large set would be necessary in order to evaluate this force field using partition coefficients.

## 6 Conclusions

This dissertation consisted in the study of solvation free energy calculations of aromatic solutes that can mimic asphaltenes with the SAFT- $\gamma$  Mie force field. By doing that, we provided information about these calculations since solvation free energy studies are mostly done using water as solvent and all atom force fields based on the Lennard Jones Potential. Additionally, the free energy estimations can help improve the SAFT- $\gamma$  Mie force field since this calculations are helpful in identifying errors in the modeling process. The parametrization of the SAFT- $\gamma$  Mie force field is more straightforward when compared to other force fields since its parameters are obtained through the SAF-VR Mie EoS. Following this strategy, the phenanthrene parameters were obtained using two different ring equations and geometries and phase equilibrium data. However, only the parameters estimated with the ring equation proposed by [Müller and Mejía \(2017\)](#) were used in the solvation free energy simulations since this equation provided a more adequate set of parameters.

In order to obtain accurate solvation free energies, we carefully selected and optimized the coupling parameter and their respective simulation weights used in our Expanded Ensemble simulations. The resulting potential energies from these simulations were then served as input to estimate solvation free energy differences with the MBAR method. The results for solvation free energy differences with non aqueous solvents had absolute deviations to the experimental data of less than 2.0 kcal/mol, except for the pair 1-octanol+anthracene. The geometry effect on the free energy curves was also observed - larger molecules had steeper curves and larger absolute deviations. The influence of carbon dioxide on the solvation free energy of phenanthrene in toluene was found to be minimum. The  $\Delta G_{solv}$  decreased slightly until the mass fraction of  $CO_2$  was equal to 0.119 and, after this point, solvation free energies increased.

Hydration free energy differences calculations with the SAFT- $\gamma$  Mie model required the use of relatively larger values of  $k_{ij}$  in order to obtain satisfactory results.

The parameter was estimated with the output from molecular dynamics data as the strategy of using the SAFT-VR Mie EoS also didn't provide good results. This necessity of one additional parameter happens probably due to the lack of an association term on the EoS that the model is based on. The results with  $k_{ij}$  estimated with MD output were great, the absolute deviations to the experimental data found were smaller than the ones for the GAFF and ELBA force field. We also used the solvation free energies to calculate partition coefficients in water/1-octanol, water/hexane and toluene/hexane, and the results were generally satisfactory when compared to the experimental data.

Generally, the SAFT- $\gamma$  Mie force field proved to be a good model to represent the solvation phenomenon. It correctly described solvation free energy differences of solutes mimicking asphaltenes in hexane, toluene, 1-octanol and water. The requirement of binary interaction parameter estimated with MD output for hydration free energies increases the simulation time, which is already larger for this water model due to its coarse graining level. Nevertheless, the SAFT- $\gamma$  Mie force field for water used doesn't predict freezing at room temperature as other force fields, which is essential for hydration free energy calculations. This dissertation had success in using a coarse grained force field to perform free energy calculations. Based on this work, we have some ideas for future development. We intend to test the binary interaction parameter transferability to calculations with other aromatic solutes in water. Additionally, we want to use the SAFT- $\gamma$  Mie force field to model more complex asphaltenes models and, consequently, increase the scale of these simulations. The final step to expand this work would be to develop new methodologies to use solvation free energies to effectively calculate solubility

# Bibliography

ADAM, L.; MACIEJ, B.; CEZARY, C.; EWA, G.; YI, H.; DAWID, J.; PAWEL, K.; MACIEJ, M.; MARIUSZ, M.; A, M. M.; ANDREI, N.; STANISLAW, O.; A, S. H.; K, S. A.; RAFAL, S.; TOMASZ, W.; YANPING, Y.; BARTLOMIEJ, Z. A unified coarse-grained model of biological macromolecules based on mean-field multipole-multipole interactions. *Journal of molecular modeling*, v. 20, p. 2306, 2014.

AIMOLI, C. G.; MAGINN, E. J.; ABREU, C. R. A. Force field comparison and thermodynamic property calculation of supercritical  $CO_2$  and  $CH_4$  using molecular dynamics simulations. *Fluid Phase Equilibria*, v. 368, p. 80–90, 2014.

AIMOLI, C. G.; MAGINN, E. J.; ABREU, C. R. A. Transport properties of carbon dioxide and methane from molecular dynamics simulations. *The Journal of Chemical Physics*, v. 141, p. 134101, 2014.

ANDERSEN, H. C. Molecular dynamics simulations at constant pressure and/or temperature. *Journal of Chemical Physics*, v. 72, p. 2384–2393, 1980.

AVENDAÑO, C.; LAFITTE, T.; GALINDO, A.; ADJIMAN, C. S.; JACKSON, G.; MÜLLER, E. A. Saft- $\gamma$  force field for the simulation of molecular fluids.1. a single-site coarse grained model of carbon dioxide. *The Journal of Physical Chemistry B*, v. 115, p. 11154–11169, 2011.

BARDUCCI, A.; BONOMI, M.; DERREUMAUX, P. Assessing the quality of the opep coarse-grained force field. *Journal of Chemical Theory and Computation*, v. 7, p. 1928–1934, 2011.

BARKER, J. A.; HENDERSON, D. What is "liquid"? understanding the states of matter. *Review of Modern Physics*, v. 48, p. 587–671, 1976.

BASDEVANT, N.; BORGIS, D.; HA-DUONG, T. Modeling protein-protein recognition in solution using the coarse-grained force field scorpion. *Journal of Chemical Theory and Computation*, v. 9, p. 803–813, 2013.

BECKSTEIN, O.; FOURRIER, A.; IORGA, B. I. Prediction of hydration free energies for the sampl4 diverse set of compounds using molecular dynamics simulations with the op1s-aa force field. *Journal of Computer-Aided Molecular Design*, v. 28, n. 3, p. 265–276, Mar 2014.

BENNETT, C. Efficient estimation of free energy differences from monte carlo data. *Journal of Computational Physics*, v. 22, p. 245–268, 1976.

BEREAU, T.; BACHMANN, M.; DESERNO, M. Interplay between secondary and tertiary structure formation in protein folding cooperativity. *Journal of the American Chemical Society*, v. 132, p. 13129–13131, 2010.

BEREAU, T.; DESERNO, M. Generic coarse-grained model for protein folding and aggregation. *Journal of Chemical Physics*, v. 130, p. 235106, 2009.



- BERENDSEN, H. J. C.; POSTMA, J. P. M.; GUNSTEREN, W. F. van; DINOLA, A.; HAAK, J. R. Molecular dynamics with coupling to an external bath. *The Journal of Chemical Physics*, v. 81, n. 8, p. 3684–3690, 1984.
- BERG, B. A.; NEUHAUS, T. Multicanonical ensemble: A new approach to simulate first-order phase transitions. *Physical Review Letters*, American Physical Society, v. 68, p. 9–12, Jan 1992.
- BEUTLER, T.; MARK, A.; SCHAIK, R. van; GERBER, P.; GUNSTEREN, W. van. Avoiding singularities and numerical instabilities in free energy calculations based on molecular simulations. *Chemical Physics Letters*, v. 222, p. 529–539, 1994.
- BHARGAVA, B.; KLEIN, M. L. Formation of micelles in aqueous solutions of a room temperature ionic liquid: a study using coarse grained molecular dynamics. *Molecular Simulation*, v. 107, p. 393–401, 2009.
- BUENROSTRO-GONZALEZ, E.; LIRA-GALEANA, C.; GIL-VILLEGAS, A.; WU, J. Asphaltene precipitation in crude oils: Theory and experiments. *AIChE Journal*, American Institute of Chemical Engineers, v. 50, n. 10, p. 2552–2570, 2004.
- CHANG, C. J. The solubility of carbon dioxide in organic solvents at elevated pressures. *Fluid Phase Equilibria*, v. 15, p. 235–242, 1992.
- CHEBARO, Y.; DONG, X.; LAGHAEL, R.; DERREUMAUX, P.; MOUSSEAU, N. Replica exchange molecular dynamics simulations of coarse-grained proteins in implicit solvent. *Journal of Physical Chemistry B*, v. 113, p. 267–274, 2009.
- CHIPOT, C.; POHORILLE, A. *Free Energy Calculations Theory and Applications in Chemistry and Biology*. 1. ed. New York: Springer, 2007.
- CHIU, S. W.; SCOTT, H. L.; JAKOBSSON, E. A coarse-grained model based on morse potential for water and n-alkanes. *Journal of Chemical Theory and Computation*, v. 6, p. 851–863, 2010.
- CHODERA, J. D.; SHIRTS, M. R. Replica exchange and expanded ensemble simulations as gibbs sampling: simple improvements for enhanced mixing. *Journal of Chemical Physics*, v. 135, p. 194110, 2011.
- DAYAL, P.; TREBST, S.; WESSEL, S.; WÜRTZ, D.; TROYER, M.; SABHAPANDIT, S.; COPPERSMITH, S. N. Performance limitations of flat-histogram methods. *Physical Review Letters*, American Physical Society, v. 92, p. 097201, Mar 2004.
- ERVIK, A.; LYSGAARD, M. O.; HERDES, C.; JIMÉNEZ-SERRATOS, G.; MÜLLER, E. A.; MUNKEJORD, S. T.; MÜLLER, B. A multiscale method for simulating fluid interfaces covered with large molecules such as asphaltenes. *Journal of Computational Physics*, v. 327, p. 576–611, 2016.
- ERVIK, A.; MEJÍA, A.; MÜLLER, E. A. Bottled saft: A web app providing saft- $\gamma$  mie force field parameters for thousands of molecular fluids. *Journal of Chemical Information and Modeling*, v. 56, p. 1609–1614, 2016.
- ESCOBEDO, F. A.; MARTINEZ-VERACOECHEA, F. J. Optimized expanded ensembles for simulations involving molecular insertions and deletions. i. closed systems. *Journal of Chemical Physics*, v. 127, p. 174103, 2007.

FERRENBURG, A. M.; SWENDSEN, R. H. Optimized monte carlo data analysis. *Phys. Rev. Lett.*, American Physical Society, v. 63, p. 1195–1198, Sep 1989.

FRENKEL, D. Simulations: The dark side. *The European Physical Journal Plus*, v. 128, n. 1, p. 10, 2013.

FRENKEL, D.; SMIT, B. *Understanding Molecular Simulation*. 2nd. ed. Orlando, FL, USA: Academic Press, Inc., 2001.

GAO, F.; XU, Z.; LIU, G.; YUAN, S. Molecular dynamics simulation: The behavior of asphaltene in crude oil and at the oil/water interface. *Energy & Fuels*, v. 28, n. 12, p. 7368–7376, 2014.

GARRIDO, N. M.; JORGE, M.; QUEIMADA, A. J.; MACEDO, E. A.; ECONOMOU, I. G. Using molecular simulation to predict solute solvation and partition coefficients in solvents of different polarity. *Physical Chemistry Chemical Physics*, v. 20, p. 9155–9164, 2011.

GARRIDO, N. M.; QUEIMADA, A. J.; JORGE, M.; MACEDO, E. A.; ECONOMOU, I. G. 1-octanol/water partition coefficients of n-alkanes from molecular simulations of absolute solvation free energies. *Journal of Chemical Theory and Computation*, v. 5, p. 2436–2446, 2009.

GEMAN, S.; GEMAN, D. Stochastic relaxation, gibbs distributions, and the bayesian restoration of images. *IEEE Transactions on Pattern Analysis and Machine Intelligence*, PAMI-6, p. 721 – 741, 1984.

GENHEDEN, S. Predicting partition coefficients with a simple all-atom/coarse-grained hybrid model. *Journal of Chemical Theory and Computation*, v. 12, n. 1, p. 297–304, 2016.

GONÇALVES, P. F. B.; STASSEN, H. Free energy of solvation from molecular dynamics simulation applying voronoi-delaunay triangulation to the cavity creation. *The Journal of Chemical Physics*, v. 123, p. 214109, 2005.

GREENFIELD, M. L. Molecular modelling and simulation of asphaltenes and bituminous materials. *International Journal of Pavement Engineering*, v. 12, n. 4, p. 325–341, 2011.

HADLEY, K. R.; MCCABE, C. On the investigation of coarse-grained models for water: Balancing computational efficiency and the retention of structural properties. *The Journal of Physical Chemistry B*, v. 114, n. 13, p. 4590–4599, 2010.

HADLEY, K. R.; MCCABE, C. Coarse-grained molecular models of water: a review. *Molecular Simulation*, v. 38, p. 671–681, 2012.

HE, X.; SHINODA, W.; DEVANE, R.; KLEIN, M. L. Exploring the utility of coarse-grained water models for computational studies of interfacial systems. *Molecular Simulation*, v. 108, p. 2007–2020, 2010.

HEADEN, T. F.; BOEK, E. S.; JACKSON, G.; TOTTON, T. S.; MÜLLER, E. A. Simulation of asphaltene aggregation through molecular dynamics: Insights and limitations. *Energy & Fuels*, v. 31, n. 2, p. 1108–1125, 2017.

HERDES, C.; ERVIK, A.; MEJÍA, A.; MÜLLER, E. A. Prediction of the water/oil interfacial tension from molecular simulations using the coarse-grained soft- $\gamma$  mie force field. *Fluid Phase Equilib.*, 2017.

HERDES, C.; TOTTON, T. S.; MÜLLER, E. A. Coarse grained force field for the molecular simulation of natural gases and condensates. *Fluid Phase Equilibria*, v. 406, p. 91–100, 2015.

HOOVER, W. G. Canonical dynamics: Equilibrium phase-space distributions. *Phys. Rev. A*, American Physical Society, v. 31, p. 1695–1697, Mar 1985.

IZAIRI, R.; KAMBERAJ, H. Comparison study of polar and nonpolar contributions to solvation free energy. *Journal of Chemical Information and Modeling*, v. 57, p. 2539–2553, 2017.

JORGE, M.; GARRIDO, N.; QUEIMADA, A.; ECONOMOU, I.; MACEDO, E. Effect of the integration method on the accuracy and computational efficiency of free energy calculations using thermodynamic integration. *Journal of Chemical Theory and Computation*, v. 6, p. 1018–1027, 2010.

JORGENSEN, W. L.; TIRADO-RIVES, J. The opls [optimized potentials for liquid simulations] potential functions for proteins, energy minimizations for crystals of cyclic peptides and crambin. *Journal of the American Chemical Society*, v. 110, n. 6, p. 1657–1666, 1988.

JOSHI, N. B.; MULLINS, O. C.; JAMALUDDIN, A.; CREEK, J.; MCFADDEN, J. Asphaltene precipitation from live crude oil. *Energy & Fuels*, v. 15, n. 4, p. 979–986, 2001.

JOVER, J. F.; MÜLLER, E. A.; HASLAM, A. J.; GALINDO, A.; JACKSON, G.; TOULHOAT, H.; NIETO-DRAGHI, C. Aspects of asphaltene aggregation obtained from coarse-grained molecular modeling. *Energy and Fuels*, v. 29, n. 2, p. 556–566, 2015.

KIRKWOOD, J. Statistical mechanics of fluid mixtures. *Journal of Chemical Physics*, v. 3, p. 300–313, 1935.

KLIMOVICH, P. V.; SHIRTS, M. R.; MOBLEY, D. L. Guidelines for the analysis of free energy calculations. *Journal of Computer-Aided Molecular Design*, v. 29, p. 397–411, 2015.

KMIECIK, S.; GRONT, D.; KOLINSKI, M.; WIETESKA, L.; DAWID, A. E.; KOLINSKI, A. Coarse-grained protein models and their applications. *Chemical Reviews*, v. 116, p. 7898–7936, 2016.

KOGA, N.; TAKADA, S. Roles of native topology and chain-length scaling in protein folding: a simulation study with a go-like model. *Journal of Molecular Biology*, v. 331, p. 171–180, 2001.

KUMAR, S.; BOUZIDA, D.; SWENDSEN, R.; KOLLMAN, P.; ROSENBERG, J. The weighted histogram analysis method for free-energy calculations on biomolecules. 1. the method. *Journal of Computational Chemistry*, v. 13, p. 1011–1021, 1992.

KUZNICKI, T.; MASLIYAH, J. H.; BHATTACHARJEE, S. Aggregation and partitioning of model asphaltenes at toluene - water interfaces: Molecular dynamics simulations. *Energy and Fuels*, v. 23, n. 10, p. 5027–5035, 2009.

- LAFITTE, T.; APOSTOLAKOU, A.; AVENDANO, C.; GALINDO, A.; ADJIMAN, C. S.; MULLER, E. A.; JACKSON, G. Accurate statistical associating fluid theory for chain molecules formed from mie segments. *The Journal of Chemical Physics*, v. 139, p. 154504, 2013.
- LAFITTE, T.; AVENDAÑO, C.; PAPAIOANNOU, V.; GALINDO, A.; ADJIMAN, C. S.; JACKSON, G.; MÜLLER, E. A. Saft- $\gamma$  force field for the simulation of molecular fluids: 3. coarse-grained models of benzene and hetero-group models of n-decylbenzene. *Molecular Physics*, v. 110, p. 1189–1203, 2012.
- LARS, V.; PERIOLE, X.; TIELEMAN, D. P.; MARRINK, S. J. Improved parameters for the martini coarse-grained protein force field. *Journal of Chemical Theory and Computation*, v. 9, p. 687–697, 2013.
- LEE, J. New monte carlo algorithm: Entropic sampling. *Physical Review Letters*, American Physical Society, v. 71, p. 211–214, Jul 1993.
- LEVITT, M. A simplified representation of protein conformations for rapid simulation of protein folding. *Journal of Molecular Biology*, v. 104, p. 59–107, 1976.
- LEVITT, M.; WARSHE, A. Computer-simulation of protein folding. *Nature*, v. 253, p. 694–698, 1975.
- LI, D. D.; GREENFIELD, M. L. High internal energies of proposed asphaltene structures. *Energy & Fuels*, v. 25, n. 8, p. 3698–3705, 2011.
- LIU, J. S. *Monte Carlo strategies in Scientific Computing*. 2. ed. New York: Springer, 2002.
- LOBANOVA, O.; AVENDAÑO, C.; LAFITTE, T.; MÜLLER, E. A.; JACKSON, G. Saft- $\gamma$  force field for the simulation of molecular fluids: 4. a single-site coarse-grained model of water applicable over a wide temperature range. *Mol. Phys.*, v. 113, p. 1228–1249, 2015.
- LOBANOVA, O.; MEJÍA, A.; JACKSON, G.; MÜLLER, E. A. Saft- $\gamma$  force field for the simulation of molecular fluids 6: Binary and ternary mixtures comprising water, carbon dioxide, and n-alkanes. *The Journal of Chemical Thermodynamics*, v. 93, p. 320–336, 2016.
- LYUBARTSEV, A. P.; MARTSINOVSKI, A. A.; SHEVKUNOV, S. V.; VORONTSOV-VELYAMINOV, P. N. New approach to monte carlo calculation of the free energy: Method of expanded ensembles. *Journal of Chemical Physics*, v. 96, p. 1776–1783, 1992.
- MARRINK, S. J.; RISSELADA, H. J.; YEFIMOV, S.; TIELEMAN, D. P.; VRIES, A. H. de. The martini force field: Coarse grained model for biomolecular simulations. *Journal of Physical Chemistry B*, v. 111, p. 7812–7824, 2007.
- MARRINK, S. J.; TIELEMAN, D. P. Perspective on the martini model. *Chemical Society Reviews*, v. 42, p. 6801–6822, 2013.
- MARTÍNEZ, L.; ANDRADE, R.; BIRGIN, E. G.; MARTÍNEZ, J. M. Packmol: a package for building initial configurations for molecular dynamics simulations. *Journal of Computational Chemistry*, v. 30, p. 2157–2164, 2009.
- MARTYNA, G. J.; TOBIAS, D. J.; KLEIN, M. L. Constant pressure molecular dynamics algorithms. *The Journal of Chemical Physics*, v. 101, n. 5, p. 4177–4189, 1994.

- MATOS, G. D. R.; KYU, D. Y.; LOEFFLER, H. H.; CHODERA, J. D.; SHIRTS, M. R.; MOBLEY, D. L. Approaches for calculating solvation free energies and enthalpies demonstrated with an update of the freesolv database. *Journal Chemical Engineering Data*, v. 62, p. 1559–1569, 2017.
- MATUBAYASI, N. Free-energy analysis of protein solvation with all-atom molecular dynamics simulation combined with a theory of solutions. *Current Opinion in Structural Biology*, v. 43, p. 45 – 54, 2017. Theory and simulation • Macromolecular assemblies.
- MEJÍA, A.; HERDES, C.; MÜLLER, E. A. Force fields for coarse-grained molecular simulations from a corresponding states correlation. *Industrial and Chemical Engineering Research*, v. 53, p. 4131–4141, 2014.
- Metropolis, N.; Rosenbluth, A. W.; Rosenbluth, M. N.; Teller, A. H.; Teller, E. Equation of State Calculations by Fast Computing Machines. *The Journal of Chemical Physics*, v. 21, p. 1087–1092, 1953.
- MIE, G. Zur kinetischen theorie der einatomigen korper. *Ann. Phys.*, v. 316, p. 657–697, 1903.
- MIKAMI, Y.; LIANG, Y.; MATSUOKA, T.; BOEK, E. S. Molecular dynamics simulations of asphaltenes at the oil–water interface: From nanoaggregation to thin-film formation. *Energy & Fuels*, v. 27, n. 4, p. 1838–1845, 2013.
- MOBLEY, D. L.; DUMONT, E.; CHODERA, J. D.; DILL, K. A. Comparison of charge models for fixed-charge force fields: Small-molecule hydration free energies in explicit solvent. *The Journal of Physical Chemistry B*, v. 111, n. 9, p. 2242–2254, 2007.
- MOBLEY, D. L.; GILSON, M. K. Predicting binding free energies: Frontiers and benchmarks. *Annual Review of Biophysics*, v. 46, n. 1, p. 531–558, 2017.
- MOBLEY, D. L.; GUTHRIE, J. P. Freesolv: a database of experimental and calculated hydration free energies, with input files. *Journal of computer-aided molecular design*, v. 28, n. 7, p. 711–720, July 2014.
- MOHAMED, N. A.; BRADSHAW, R. T.; ESSEX, J. W. Evaluation of solvation free energies for small molecules with the amoeba polarizable force field. *Journal of Computational Chemistry*, v. 37, p. 2749–2758, 2016.
- MORTIMER, S.; MURPHY, R. The vapor pressures of some substances found in coal tar. *Industrial and Engineering Chemistry Research*, v. 14, p. 1140–1142, 1923.
- MÜLLER, E. A.; GUBBINS, K. E. Simulation of hard triatomic and tetratomic molecules. a test of associating fluid theory. *Molecular Physics*, v. 80, p. 957–976, 1993.
- MÜLLER, E. A.; JACKSON, G. Force field parameters from the saft -  $\gamma$  equation of state for use in coarse-grained molecular simulations. *Annual Review of Chemical and Biomolecular Engineering*, v. 5, n. 1, p. 405–427, 2014.
- MÜLLER, E. A.; MEJÍA, A. Extension of the saft-vr mie eos to model homonuclear rings and its parametrization based on the principle of corresponding states. *Langmuir*, -, p. A–L, 2017.
- MULLINS, O. C. The modified yen model. *Energy & Fuels*, v. 24, n. 4, p. 2179–2207, 2010.

MURGICH, J. Molecular simulation and the aggregation of the heavy fractions in crude oils. *Molecular Simulation*, v. 29, n. 6-7, p. 451–461, 2003.

NOSÉ, S. A unified formulation of the constant temperature molecular dynamics methods. *The Journal of Chemical Physics*, v. 81, n. 1, p. 511–519, 1984.

ORSI, M.; ESSEX, J. W. The elba force field for coarse-grain modeling of lipid membranes. *PLOS ONE*, Public Library of Science, v. 6, n. 12, p. 1–22, 12 2011.

PALIWAL, H.; SHIRTS, M. R. A benchmark test set for alchemical free energy transformations and its use to quantify error in common free energy methods. *Journal of Chemical Theory and Computation*, v. 7, p. 4115–4134, 2011.

PANAGIOTOPOULOS, A. Direct determination of phase coexistence properties of fluids using *Molecular Physics*, v. 61, p. 813–826, 1987.

PANTANO, D.; KLEIN, M. L. Characterization of membrane-protein interactions for the leucine transporter from *aquifex aeolicus* by molecular dynamics calculations. *Journal of Physical Chemistry B*, v. 113, p. 13715–13722, 2009.

PAPAIIOANNOU, V.; LAFITTE, T.; AVENDAÑO, C.; ADJIMAN, C. S.; JACKSON, G.; MÜLLER, E. A.; GALINDO, A. Group contribution methodology based on the statistical associating fluid theory for heteronuclear molecules formed from mie segments. *The Journal of Chemical Physics*, v. 140, p. 054107, 2014.

PARRINELLO, M.; RAHMAN, A. Polymorphic transitions in single crystals: A new molecular dynamics method. *Journal of Applied Physics*, v. 52, n. 12, p. 7182–7190, 1981.

PLIMPTON, S. Fast parallel algorithms for short-range molecular dynamics. *Journal of Computational Physics*, v. 117, p. 1–19, 1995.

POHORILLE, A.; JARZYNSKI, C.; CHIPOT, C. Good practices in freeenergy calculations. *Journal of Physical Chemistry B*, v. 114, p. 10235–10253, 2010.

POOLE, S. K.; DURHAM, D.; KIBBEY, C. Rapid method for estimating the octanol–water partition coefficient (log *p*<sub>ow</sub>) by microemulsion electrokinetic chromatography. *Journal of Chromatography B: Biomedical Sciences and Applications*, v. 745, n. 1, p. 117 – 126, 2000.

RAMRATTAN, N.; AVENDAÑO, C.; MÜLLER, E.; GALINDO, A. A corresponding-states framework for the description of the mie family of intermolecular potentials. *Molecular Physics*, v. 113, p. 1–16, 2015.

RAVINDRA, K.; SOKHI, R.; GRIEKEN, R. V. Atmospheric polycyclic aromatic hydrocarbons: Source attribution, emission factors and regulation. *Atmospheric Environment*, v. 42, n. 13, p. 2895 – 2921, 2008.

ROUX, B. The calculation of the potential of mean force using computer simulations. *Computer Physics Communications*, v. 91, n. 1, p. 275 – 282, 1995.

ROWLINSON, J. S.; SWINTON, F. L. *Liquid and Liquid Mixtures*. 3. ed. London: Butterworth Scientific, 1982.

ROY, D.; BLINOV, N.; KOVALENKO, A. Predicting accurate solvation free energy in n-octanol using 3d-rism-kh molecular theory of solvation: Making right choices. *Journal of Physical Chemistry B*, v. 121, p. 9268–9273, 2017.

RUELLE, P. The n-octanol and n-hexane/water partition coefficient of environmentally relevant chemicals predicted from the mobile order and disorder (mod) thermodynamics. *Chemosphere*, v. 40, n. 5, p. 457 – 512, 2000.

SANGSTER, J. *Octanol-Water Partitioning Coefficients: Fundamentals and Physical Chemistry*. 1nd. ed. [S.l.]: John Wiley and Sons, 1997.

SCHULER, L. D.; DAURA, X.; GUNSTEREN, W. F. van. An improved gromos96 force field for aliphatic hydrocarbons in the condensed phase. *Journal of Computational Chemistry*, v. 22, n. 11, p. 1205–1218, 2001.

SCHULTE, J.; DÜRR, J.; RITTER, S.; HAUTHAL, W. H.; QUITZSCH, K.; MAURER, G. Partition coefficients for environmentally important, multifunctional organic compounds in hexane + water. *Journal of Chemical & Engineering Data*, v. 43, n. 1, p. 69–73, 1998.

SHELL, M. S. *Thermodynamics and Statistical Mechanics: a Integrated Approach*. 1nd. ed. [S.l.]: Cambridge University Press, 2015.

SHINODA, W.; DEVANE, R.; KLEIN, M. L. Multi-property fitting and parameterization of a coarse grained model for aqueous surfactants. *Molecular Simulation*, v. 33, p. 27–36, 2007.

SHINODA, W.; DEVANE, R.; KLEIN, M. L. Zwitterionic lipid assemblies: molecular dynamics studies of monolayers, bilayers, and vesicles using a new coarse grain force field. *Journal of Physical Chemistry B*, v. 114, p. 6836–6849, 2010.

SHIRTS, M. R.; CHODERA, J. D. Statistically optimal analysis of samples from multiple equilibrium states. *Journal of Chemical Physics*, v. 129, p. 124105, 2008.

SHIRTS, M. R.; PANDE, V. S. Comparison of efficiency and bias of free energies computed by exponential averaging, the bennett acceptance ratio, and thermodynamic integration. *J. Chem. Phys.*, v. 122, p. 144107, 2005.

SHIRTS, M. R.; PITERA, J. W.; SWOPE, W. C.; PANDE, V. S. Extremely precise free energy calculations of amino acid side chain analogs: Comparison of common molecular mechanics force fields for proteins. *Journal of Chemical Physics*, v. 119, p. 5740, 2003.

SHYU, C.; YTREBERG, F. M. Reducing the bias and uncertainty of free energy estimates by using regression to fit thermodynamic integration data. *Journal of Computational Chemistry*, v. 6, p. 1018–1027, 2010.

SJÖBLOM, J.; ASKE, N.; AUFLEM, I. H.; BRANDAL Øystein; HAVRE, T. E.; SæTHER Øystein; WESTVIK, A.; JOHNSEN, E. E.; KALLEVIK, H. Our current understanding of water-in-crude oil emulsions.: Recent characterization techniques and high pressure performance. *Advances in Colloid and Interface Science*, v. 100-102, n. Supplement C, p. 399 – 473, 2003.

SJÖBLOM, J.; SIMON, S.; XU, Z. Model molecules mimicking asphaltenes. *Advances in Colloid and Interface Science*, v. 218, n. Supplement C, p. 1 – 16, 2015.

SMITH, J.; NESS, H. V.; ABBOT, M. M. *Introdução á Termodinâmica da Engenharia Química*. 2. ed. Rio de Janeiro: LTC, 2007.

SOROUSH, S.; STRAVER, E. J.; RUDOLPH, E. S. J.; PETERS, C. J.; LOOS, T. W. de; ZITHA, P. L.; VAFAIE-SEFTI, M. Phase behavior of the ternary system carbon dioxide+toluene+asphaltene. *Fuel*, v. 137, n. Supplement C, p. 405 – 411, 2014.

STERPONE, F.; DERREUMAUX, P.; MELCHIONNA, S. Protein simulations in fluids: Coupling the opep coarse-grained force field with hydrodynamics. *ga*, v. 11, p. 1843–1853, 2015.

STERPONE, F.; MELCHIONNA, S.; TUFFERY, P.; PASQUALI, S.; MOUSSEAU, N.; CRAGNOLINI, T.; CHEBARO, Y.; ST-PIERRE, J.-F.; KALIMERI, M.; BARDUCCI, A.; LAURIN, Y.; TEK, A.; BAADEN, M.; NGUYEN, P. H.; DERREUMAUX, P. The opep protein model: from single molecules, amyloid formation, crowding and hydrodynamics to dna/rna systems. *Chemical Society Reviews*, v. 43, p. 4871– 4893, 2014.

TEKLEBRHAN, R. B.; GE, L.; BHATTACHARJEE, S.; XU, Z.; SJÖBLOM, J. Initial partition and aggregation of uncharged polyaromatic molecules at the oil–water interface: A molecular dynamics simulation study. *The Journal of Physical Chemistry B*, v. 118, n. 4, p. 1040–1051, 2014. PMID: 24397444.

TORRIE, G.; VALLEAU, J. Nonphysical sampling distributions in monte carlo free-energy estimation: Umbrella sampling. *Journal of Computational Physics*, v. 23, n. 2, p. 187 – 199, 1977.

TREBST, S.; HUSE, D. A.; TROYER, M. Optimizing the ensemble for equilibration in broad-histogram monte carlo simulations. *Physical Review E*, American Physical Society, v. 70, p. 046701, Oct 2004.

TUCKERMAN, M. *Statistical Mechanics: Theory And Molecular Simulation*. 1nd. ed. New York, NY, USA: Oxford University Press, 2010.

VERLET, L. Computer "experiments" on classical fluids. i. thermodynamical properties of lennard-jones molecules. *Physical Review*, v. 159, p. 98–103, 1967.

WINGER, M.; TRZESNIAK, D.; BARON, R.; GUNSTEREN, W. van. On using a too large integration time step in molecular dynamics simulations of coarse-grained molecular models. *Physical Chemistry Chemical Physics*, v. 11, p. 1934, 2009.

YTREBERG, F. M.; SWENDSEN, R. H.; ZUCKERMAN, D. M. Comparison of free energy methods for molecular systems. *Journal of Chemical Physics*, v. 125, p. 184114, 2006.

ZWANZIG, R. W. High-temperature equation of state by a perturbation method. i. nonpolar gases. *The Journal of Chemical Physics*, v. 22, p. 1420, 1954.

ZWANZIG, R. W. High-temperature equation of state by a perturbation method. ii. polar gases. *The Journal of Chemical Physics*, v. 23, p. 1915, 1955.



# APPENDIX A – Optimized values of $\lambda$ and $\eta$

Table 10 – Optimized values of  $\lambda$  and  $\eta$  for the solutes in hexane

pyrene		phenanthrene	
$\lambda$	$\eta$	$\lambda$	$\eta$
0.000	0.000	0.000	0.000
0.076	4.234	0.090	1.981
0.107	5.620	0.132	3.461
0.132	6.499	0.161	4.494
0.152	6.690	0.185	5.185
0.170	6.643	0.205	5.552
0.189	6.461	0.224	5.725
0.213	6.091	0.244	5.722
0.242	5.566	0.268	5.523
0.280	4.729	0.305	4.975
0.355	2.853	0.372	3.576
0.483	-0.778	0.500	0.297
0.678	-6.947	0.560	-1.390
0.788	-10.631	0.722	-6.309
1.000	-18.141	1.000	-15.448

Table 11 – Optimized values of  $\lambda$  and  $\eta$  for the solutes in 1-octanol

propane		anthracene		phenanthrene	
$\lambda$	$\eta$	$\lambda$	$\eta$	$\lambda$	$\eta$
0.000	0.000	0.000	0.000	0.000	0.000
0.027	3.126	0.078	3.932	0.049	2.578
0.050	5.109	0.111	6.178	0.091	5.663
0.073	6.093	0.130	7.426	0.125	8.575
0.095	6.570	0.143	8.201	0.144	10.069
0.117	6.826	0.154	8.717	0.157	10.978
0.142	6.956	0.164	9.085	0.169	11.599
0.174	6.969	0.174	9.357	0.180	12.040
0.215	6.847	0.184	9.556	0.192	12.340
0.269	6.554	0.197	9.676	0.206	12.499
0.337	6.050	0.214	9.681	0.225	12.478
0.427	5.228	0.238	9.490	0.253	12.161
0.545	3.955	0.274	8.958	0.298	11.280
0.720	1.843	0.326	7.906	0.371	9.406
1.000	-1.903	0.399	6.088	0.484	5.891
		0.515	2.777	0.664	-0.516
		0.695	-2.960	0.802	-5.908
		1.000	-13.768	1.000	-14.073

Table 12 – Optimized values of  $\lambda$  and  $\eta$  for the solutes in toluene

pyrene		anthracene		phenanthrene	
$\lambda$	$\eta$	$\lambda$	$\eta$	$\lambda$	$\eta$
0.000	0.000	0.000	0.000	0.000	0.000
0.090	2.563	0.119	0.218	0.136	0.726
0.130	4.338	0.174	1.210	0.191	2.307
0.154	5.439	0.209	2.052	0.223	3.430
0.172	6.181	0.236	2.664	0.246	4.233
0.188	6.670	0.261	3.122	0.264	4.780
0.204	6.986	0.283	3.378	0.281	5.149
0.222	7.121	0.306	3.449	0.299	5.354
0.244	7.025	0.332	3.311	0.318	5.389
0.278	6.520	0.360	2.936	0.340	5.222
0.340	5.010	0.399	2.209	0.372	4.717
0.462	1.247	0.466	0.567	0.425	3.440
0.616	-4.283	0.564	-2.211	0.524	0.444
0.788	-11.032	0.715	-6.983	0.701	-5.814
1.000	-19.814	1.000	-16.923	1.000	-17.803

Table 13 – Optimized values of  $\lambda$  and  $\eta$  for the phenanthrene in different mass fractions of  $CO_2$  in toluene

0.087		0.119		0.169		0.289	
$\lambda$	$\eta$	$\lambda$	$\eta$	$\lambda$	$\eta$	$\lambda$	$\eta$
0.000	0.000	0.000	0.000	0.000	0.000	0.000	0.000
0.128	0.604	0.128	0.732	0.064	0.883	0.066	0.806
0.184	2.067	0.186	2.223	0.108	0.764	0.111	0.760
0.217	3.164	0.219	3.319	0.175	1.969	0.172	1.983
0.240	3.940	0.244	4.098	0.214	3.156	0.204	2.967
0.260	4.472	0.267	4.704	0.240	3.974	0.227	3.627
0.277	4.823	0.289	5.031	0.258	4.457	0.245	4.082
0.295	5.035	0.313	5.084	0.273	4.750	0.262	4.395
0.318	5.059	0.339	4.950	0.287	4.921	0.279	4.583
0.347	4.762	0.373	4.371	0.305	4.962	0.299	4.621
0.397	3.753	0.425	3.055	0.326	4.885	0.325	4.423
0.491	1.031	0.488	1.196	0.361	4.401	0.365	3.739
0.670	-5.148	0.525	-0.027	0.419	2.990	0.428	2.198
0.791	-9.713	0.730	-7.185	0.527	-0.299	0.530	-0.842
1.000	-18.098	1.000	-17.769	0.697	-6.180	0.701	-6.763
				1.000	-17.998	1.000	-18.163

Table 14 – Optimized values of  $\lambda$  and  $\eta$  for the solutes in water

propane		benzene		toluene		phenanthrene	
$\lambda$	$\eta$	$\lambda$	$\eta$	$\lambda$	$\eta$	$\lambda$	$\eta$
0.000	0.000	0.000	0.000	0.000	0.000	0.000	0.000
0.107	2.673	0.193	-0.295	0.177	0.182	0.142	-2.462
0.157	4.703	0.279	1.468	0.262	2.432	0.256	0.597
0.186	6.047	0.324	2.931	0.307	4.244	0.319	4.504
0.210	7.148	0.357	4.168	0.336	5.552	0.358	7.762
0.230	8.017	0.381	5.091	0.360	6.696	0.384	10.104
0.250	8.883	0.405	5.891	0.380	7.558	0.407	12.185
0.272	9.291	0.427	6.443	0.400	8.233	0.427	13.607
0.294	9.700	0.449	6.770	0.422	8.678	0.446	14.490
0.328	9.900	0.476	6.900	0.443	8.859	0.469	14.834
0.381	9.930	0.506	6.805	0.473	8.810	0.494	14.667
0.484	9.463	0.555	6.392	0.514	8.452	0.533	13.832
0.623	8.195	0.653	5.109	0.606	7.148	0.620	11.069
0.781	6.378	0.810	2.421	0.755	4.273	0.806	3.279
1.000	3.333	1.000	-1.480	1.000	-1.547	1.000	-6.122

# APPENDIX B – Overlapping Matrices

$\lambda$	0	1	2	3	4	5	6	7	8	9	10	11	12	13	14
0	.75	.19	.05	.01											
1	.28	.33	.19	.09	.05	.03	.02	.01							
2	.08	.21	.19	.15	.12	.10	.07	.04	.02	.01					
3	.01	.08	.11	.13	.14	.15	.15	.11	.07	.03	.01				
4		.03	.05	.08	.12	.16	.18	.16	.12	.07	.03	.01			
5		.01	.02	.05	.09	.14	.18	.18	.15	.10	.05	.01			
6			.01	.03	.07	.12	.17	.19	.18	.13	.07	.02			
7				.02	.04	.09	.14	.19	.20	.16	.11	.04	.01		
8				.01	.03	.06	.12	.17	.20	.19	.15	.06	.01		
9					.02	.04	.08	.14	.19	.20	.19	.09	.02	.01	
10					.01	.02	.05	.09	.14	.19	.25	.17	.06	.03	
11						.01	.02	.04	.07	.11	.21	.27	.17	.09	.01
12								.01	.02	.03	.08	.18	.32	.29	.07
13									.01	.01	.03	.10	.30	.38	.16
14											.01	.03	.16	.36	.44

Figure B.0.1 – Overlapping matrix for hexane+pyrene.

$\lambda$	0	1	2	3	4	5	6	7	8	9	10	11	12	13	14
0	.54	.29	.11	.04	.01										
1	.29	.31	.19	.11	.05	.03	.01	.01							
2	.14	.25	.20	.15	.10	.07	.04	.02	.01						
3	.06	.15	.17	.16	.14	.11	.09	.06	.04	.02					
4	.02	.07	.11	.13	.14	.13	.13	.11	.09	.05	.02				
5	.01	.03	.06	.09	.12	.13	.14	.14	.13	.10	.04	.01			
6		.01	.03	.05	.08	.11	.13	.15	.17	.16	.07	.02	.01		
7			.01	.03	.05	.08	.11	.15	.19	.21	.12	.03	.02		
8				.01	.03	.05	.08	.12	.19	.25	.17	.06	.03		
9					.01	.02	.05	.09	.16	.26	.24	.10	.06	.01	
10						.01	.02	.04	.09	.20	.27	.19	.14	.03	
11								.01	.03	.08	.17	.28	.28	.13	.02
12									.01	.04	.12	.27	.31	.20	.03
13										.01	.04	.17	.27	.37	.14
14											.01	.05	.09	.31	.55

Figure B.0.2 – Overlapping matrix for hexane+phenanthrene.

$\lambda$	0	1	2	3	4	5	6	7	8	9	10	11	12	13	14
0	.66	.26	.06	.01											
1	.40	.30	.14	.08	.04	.02	.01								
2	.10	.14	.17	.22	.15	.09	.06	.03	.02	.01					
3	.01	.03	.09	.20	.20	.16	.12	.08	.05	.03	.01	.01			
4		.01	.05	.14	.18	.17	.15	.12	.08	.05	.03	.01	.01		
5			.02	.09	.15	.16	.16	.14	.11	.08	.04	.02	.01		
6			.01	.06	.11	.14	.15	.16	.13	.11	.06	.04	.02	.01	
7			.01	.04	.07	.11	.13	.16	.15	.14	.09	.06	.03	.01	
8				.02	.05	.07	.10	.14	.16	.17	.13	.09	.05	.02	
9				.01	.02	.04	.07	.11	.14	.18	.16	.14	.09	.03	.01
10					.01	.02	.04	.07	.10	.16	.18	.18	.15	.06	.01
11					.01	.01	.02	.04	.06	.11	.15	.21	.24	.13	.02
12							.01	.02	.03	.06	.10	.19	.30	.24	.05
13								.01	.01	.02	.05	.11	.26	.38	.16
14										.01	.02	.04	.13	.34	.47

Figure B.0.3 – Overlapping matrix for 1-octanol+propane.

$\lambda$	0	1	2	3	4	5	6	7	8	9	10	11	12	13	14	15	16	17
0	.57	.28	.09	.03	.01	.01												
1	.28	.32	.17	.09	.06	.03	.02	.01	.01									
2	.13	.25	.19	.12	.09	.07	.05	.04	.03	.02	.01							
3	.06	.17	.17	.13	.11	.09	.07	.06	.05	.04	.03	.01						
4	.03	.11	.13	.12	.11	.10	.09	.08	.08	.06	.05	.03	.01					
5	.01	.07	.10	.10	.10	.10	.09	.09	.09	.09	.08	.05	.02	.01				
6	.01	.04	.07	.07	.08	.09	.09	.10	.11	.11	.10	.07	.04	.02				
7		.02	.04	.05	.07	.08	.08	.10	.11	.12	.13	.10	.06	.03	.01			
8		.01	.02	.03	.05	.06	.07	.09	.11	.13	.15	.13	.09	.04	.01			
9			.01	.02	.03	.04	.05	.07	.10	.13	.17	.16	.12	.06	.02	.01		
10				.01	.02	.02	.04	.05	.08	.11	.17	.19	.16	.10	.04	.01		
11					.01	.01	.02	.03	.05	.09	.14	.19	.20	.15	.07	.02		
12							.01	.01	.03	.05	.10	.17	.22	.21	.13	.05	.01	
13								.01	.01	.03	.06	.11	.19	.25	.22	.11	.02	
14										.01	.02	.05	.12	.21	.29	.22	.06	
15											.01	.02	.04	.11	.24	.36	.21	.01
16													.01	.03	.09	.28	.49	.10
17															.01	.06	.33	.59

Figure B.0.4 – Overlapping matrix for 1-octanol+anthracene.

$\lambda$	0	1	2	3	4	5	6	7	8	9	10	11	12	13	14	15	16	17
0	.51	.34	.11	.03	.01													
1	.37	.36	.17	.06	.02	.01												
2	.22	.32	.23	.12	.06	.03	.02	.01										
3	.10	.20	.22	.18	.11	.07	.05	.03	.02	.01	.01							
4	.04	.12	.16	.18	.13	.11	.08	.07	.05	.03	.02	.01						
5	.02	.06	.10	.14	.13	.12	.10	.10	.09	.07	.05	.02	.01					
6	.01	.03	.06	.10	.11	.11	.11	.11	.11	.10	.08	.05	.02					
7		.01	.03	.06	.07	.09	.09	.11	.13	.13	.13	.09	.05	.01				
8			.01	.03	.04	.06	.07	.10	.13	.14	.17	.14	.09	.02				
9				.01	.02	.03	.05	.07	.11	.14	.19	.19	.15	.04				
10					.01	.01	.02	.04	.07	.11	.19	.23	.22	.07	.01			
11							.01	.02	.04	.07	.15	.23	.30	.14	.02			
12								.01	.02	.04	.09	.18	.35	.24	.06	.01		
13										.01	.03	.10	.28	.34	.16	.06	.01	
14											.01	.03	.12	.27	.28	.23	.06	
15													.02	.06	.14	.44	.31	.03
16														.01	.04	.33	.49	.13
17															.01	.13	.45	.41

Figure B.0.5 – Overlapping matrix for 1-octanol+phenanthrene.



$\lambda$	0	1	2	3	4	5	6	7	8	9	10	11	12	13	14
0	.53	.30	.11	.04	.01	.01									
1	.21	.34	.22	.12	.06	.03	.01	.01							
2	.09	.25	.24	.16	.11	.07	.04	.02	.01						
3	.04	.17	.20	.17	.14	.11	.08	.05	.03	.01					
4	.02	.10	.15	.15	.14	.13	.11	.09	.07	.04	.01				
5	.01	.05	.10	.12	.13	.13	.13	.12	.11	.08	.02				
6		.02	.05	.08	.10	.12	.13	.14	.15	.14	.05	.01			
7		.01	.02	.04	.06	.09	.11	.14	.19	.21	.11	.02			
8			.01	.02	.03	.05	.08	.12	.19	.27	.18	.05	.01		
9					.01	.02	.04	.07	.15	.29	.28	.10	.02		
10							.01	.03	.08	.22	.35	.23	.06	.01	
11								.01	.02	.08	.22	.38	.22	.07	.01
12										.02	.07	.25	.37	.25	.05
13											.01	.07	.26	.45	.20
14												.01	.08	.36	.55

Figure B.0.6 – Overlapping matrix for toluene+pyrene.

$\lambda$	0	1	2	3	4	5	6	7	8	9	10	11	12	13	14
0	.48	.29	.14	.05	.02	.01									
1	.24	.30	.23	.12	.06	.03	.01								
2	.12	.24	.24	.17	.11	.06	.03	.02	.01						
3	.06	.16	.21	.19	.14	.09	.07	.04	.02	.01					
4	.03	.10	.16	.17	.15	.12	.10	.07	.05	.03	.02				
5	.01	.05	.10	.13	.14	.13	.13	.11	.09	.06	.04	.01			
6		.02	.05	.08	.10	.11	.13	.13	.12	.11	.09	.03	.01		
7		.01	.02	.04	.06	.08	.11	.13	.15	.15	.15	.07	.02		
8			.01	.02	.03	.05	.08	.11	.14	.18	.21	.12	.05	.01	
9				.01	.01	.02	.05	.08	.12	.18	.26	.18	.08	.02	
10						.01	.02	.04	.08	.15	.27	.24	.14	.04	
11							.01	.02	.04	.09	.21	.28	.25	.10	.01
12								.01	.01	.04	.12	.23	.33	.23	.03
13										.01	.04	.11	.28	.41	.14
14												.02	.08	.29	.60

Figure B.0.7 – Overlapping matrix for toluene+anthracene.

$\lambda$	0	1	2	3	4	5	6	7	8	9	10	11	12	13	14
0	.52	.31	.11	.04	.01										
1	.20	.34	.23	.12	.06	.03	.01	.01							
2	.07	.24	.25	.17	.11	.07	.04	.02	.01						
3	.03	.15	.21	.18	.14	.11	.07	.05	.03	.01	.01				
4	.01	.09	.16	.16	.15	.13	.11	.08	.06	.03	.02				
5		.05	.11	.13	.14	.13	.13	.11	.09	.06	.04	.01			
6		.02	.06	.09	.11	.12	.13	.13	.12	.10	.08	.03	.01		
7		.01	.03	.05	.08	.10	.12	.13	.14	.14	.13	.07	.02		
8			.01	.03	.04	.07	.09	.11	.14	.16	.18	.13	.04		
9				.01	.02	.04	.06	.08	.12	.16	.22	.20	.07	.01	
10					.01	.01	.03	.05	.08	.13	.24	.29	.14	.02	
11							.01	.02	.04	.08	.19	.34	.26	.07	
12									.01	.03	.09	.25	.39	.22	.01
13											.02	.07	.25	.53	.13
14													.03	.27	.69

Figure B.0.8 – Overlapping matrix for toluene+phenanthrene.

$\lambda$	0	1	2	3	4	5	6	7	8	9	10	11	12	13	14
0	.54	.30	.11	.04	.01										
1	.23	.34	.23	.11	.05	.03	.01	.01							
2	.09	.25	.25	.17	.10	.06	.04	.02	.01						
3	.04	.16	.22	.18	.13	.10	.08	.05	.03	.01					
4	.02	.10	.16	.17	.14	.12	.11	.08	.05	.03	.01				
5	.01	.05	.11	.13	.13	.13	.13	.12	.09	.06	.03				
6		.02	.06	.10	.11	.12	.14	.14	.13	.11	.06	.01			
7		.01	.03	.06	.07	.10	.13	.14	.15	.16	.11	.03			
8			.01	.02	.04	.06	.09	.13	.16	.21	.20	.07	.01		
9				.01	.01	.03	.05	.08	.13	.22	.29	.14	.02		
10						.01	.02	.03	.07	.17	.35	.27	.06	.02	
11								.01	.02	.07	.24	.39	.19	.07	.01
12										.01	.05	.19	.37	.32	.07
13											.01	.07	.29	.43	.20
14												.01	.11	.34	.54

Figure B.0.9 – Overlapping matrix for toluene+CO<sub>2</sub>(0.087)+phenanthrene.

$\lambda$	0	1	2	3	4	5	6	7	8	9	10	11	12	13	14
0	.55	.31	.10	.03	.01										
1	.24	.36	.22	.10	.05	.02	.01								
2	.09	.27	.26	.17	.10	.06	.03	.01	.01						
3	.04	.17	.22	.18	.14	.10	.07	.04	.02	.01					
4	.01	.09	.16	.17	.15	.14	.12	.08	.05	.03	.01				
5		.04	.09	.12	.13	.15	.15	.12	.10	.07	.03	.01			
6		.01	.04	.07	.10	.12	.15	.15	.15	.12	.06	.02	.01		
7			.01	.03	.05	.08	.12	.14	.17	.19	.12	.05	.03		
8				.01	.02	.04	.08	.11	.17	.22	.19	.09	.05	.01	
9					.01	.02	.03	.06	.12	.22	.26	.16	.10	.01	
10							.01	.02	.06	.15	.27	.24	.19	.04	
11								.01	.03	.09	.22	.28	.26	.11	.01
12								.01	.02	.06	.18	.28	.28	.16	.01
13										.01	.05	.13	.18	.48	.14
14											.01	.02	.03	.32	.62

Figure B.0.10 – Overlapping matrix for toluene+CO<sub>2</sub>(0.119)+phenanthrene.

$\lambda$	0	1	2	3	4	5	6	7	8	9	10	11	12	13	14	15
0	.32	.36	.24	.06	.02											
1	.24	.34	.27	.09	.03	.01	.01									
2	.18	.30	.28	.13	.06	.02	.01	.01								
3	.08	.19	.24	.19	.12	.06	.04	.03	.02	.01						
4	.03	.10	.16	.19	.16	.10	.08	.06	.05	.03	.02	.01				
5	.01	.05	.09	.14	.15	.12	.11	.09	.08	.07	.05	.02	.01			
6	.01	.03	.05	.10	.12	.11	.11	.11	.11	.10	.08	.05	.02			
7		.01	.03	.07	.09	.09	.11	.11	.12	.12	.11	.08	.04	.01		
8		.01	.01	.04	.06	.07	.09	.11	.12	.13	.14	.12	.07	.01		
9				.02	.03	.05	.07	.09	.11	.14	.16	.17	.13	.03		
10				.01	.01	.02	.04	.06	.08	.12	.17	.21	.21	.06	.01	
11						.01	.02	.03	.05	.08	.14	.23	.31	.12	.02	
12								.01	.02	.03	.07	.18	.37	.24	.07	
13										.01	.02	.07	.26	.37	.25	.01
14												.01	.07	.24	.55	.12
15													.01	.04	.30	.66

Figure B.0.11 – Overlapping matrix for toluene+ $CO_2$ (0.169)+phenanthrene.

$\lambda$	0	1	2	3	4	5	6	7	8	9	10	11	12	13	14	15
0	.33	.33	.22	.07	.02	.01										
1	.25	.31	.25	.11	.05	.02	.01									
2	.17	.27	.26	.15	.08	.04	.02	.01								
3	.08	.17	.22	.20	.13	.09	.05	.03	.02	.01						
4	.04	.10	.15	.19	.16	.12	.09	.07	.04	.03	.01	.01				
5	.02	.06	.10	.15	.15	.13	.11	.10	.07	.05	.03	.02				
6	.01	.03	.06	.11	.13	.13	.12	.12	.09	.08	.06	.03	.01			
7		.01	.03	.07	.10	.11	.12	.12	.11	.11	.10	.07	.03	.01		
8		.01	.01	.04	.07	.09	.10	.12	.12	.14	.13	.11	.05	.01		
9				.02	.04	.05	.07	.09	.11	.14	.17	.17	.10	.03		
10				.01	.01	.02	.04	.06	.08	.12	.17	.23	.18	.06	.01	
11						.01	.01	.02	.04	.08	.14	.25	.28	.14	.03	
12								.01	.01	.03	.07	.19	.33	.27	.08	
13										.01	.02	.09	.25	.38	.23	.02
14												.02	.08	.27	.50	.12
15													.01	.05	.30	.65

Figure B.0.12 – Overlapping matrix for toluene+ $CO_2$ (0.289)+phenanthrene.

$\lambda$	0	1	2	3	4	5	6	7	8	9	10	11	12	13	14
0	.45	.28	.16	.08	.02	.01									
1	.24	.26	.24	.16	.06	.02	.01	.01							
2	.13	.21	.26	.21	.09	.05	.02	.02	.01						
3	.07	.16	.24	.23	.12	.06	.04	.03	.03	.01					
4	.04	.11	.21	.22	.13	.08	.05	.05	.06	.04	.01				
5	.02	.07	.16	.19	.12	.08	.06	.08	.10	.08	.03	.01			
6	.01	.04	.09	.13	.09	.07	.07	.10	.16	.16	.07	.02			
7		.01	.04	.06	.05	.05	.06	.10	.20	.24	.14	.04	.01		
8			.01	.02	.03	.03	.04	.09	.20	.29	.19	.07	.02		
9				.01	.01	.01	.02	.06	.17	.29	.25	.13	.03	.01	
10							.01	.03	.11	.24	.28	.21	.08	.02	
11								.01	.04	.12	.21	.31	.22	.09	.01
12									.01	.03	.08	.22	.33	.26	.07
13										.01	.02	.08	.25	.40	.25
14												.02	.08	.31	.59

Figure B.0.13 – Overlapping matrix for water+propane.



$\lambda$	0	1	2	3	4	5	6	7	8	9	10	11	12	13	14
0	.44	.33	.16	.05	.02	.01									
1	.19	.32	.27	.13	.05	.03	.01								
2	.08	.23	.30	.19	.10	.06	.03	.01	.01						
3	.04	.16	.27	.20	.13	.09	.05	.03	.02	.01					
4	.02	.10	.21	.19	.14	.11	.08	.06	.04	.03	.02				
5	.01	.06	.15	.16	.13	.12	.11	.08	.07	.06	.04	.01			
6		.03	.08	.11	.11	.11	.11	.10	.10	.10	.09	.04	.01		
7		.01	.04	.06	.07	.08	.10	.10	.12	.14	.16	.09	.02		
8			.01	.03	.04	.05	.07	.09	.11	.17	.23	.15	.05	.01	
9				.01	.01	.02	.04	.06	.09	.16	.27	.22	.09	.02	
10						.01	.02	.03	.06	.14	.27	.27	.14	.04	.01
11							.01	.01	.03	.09	.23	.29	.23	.08	.01
12									.01	.04	.12	.22	.31	.22	.06
13										.01	.03	.08	.22	.39	.28
14												.02	.07	.29	.62

Figure B.0.14 – Overlapping matrix for water+benzene.

$\lambda$	0	1	2	3	4	5	6	7	8	9	10	11	12	13	14
0	.46	.32	.15	.04	.01										
1	.19	.31	.28	.13	.06	.02	.01								
2	.07	.21	.32	.20	.11	.05	.02	.01							
3	.03	.13	.28	.23	.15	.08	.05	.03	.01	.01					
4	.01	.08	.23	.22	.17	.11	.07	.05	.03	.02	.01				
5	.01	.05	.16	.19	.16	.12	.09	.07	.05	.04	.03	.01			
6		.02	.10	.14	.14	.12	.11	.09	.08	.08	.07	.03	.01		
7		.01	.05	.08	.09	.10	.10	.10	.11	.12	.14	.08	.02		
8			.01	.03	.05	.06	.07	.09	.11	.15	.22	.16	.04	.01	
9				.01	.02	.03	.04	.06	.09	.14	.27	.24	.08	.01	
10						.01	.02	.03	.06	.12	.27	.31	.15	.03	
11							.01	.01	.03	.08	.23	.33	.23	.07	.01
12									.01	.03	.12	.25	.34	.22	.03
13										.01	.03	.08	.24	.45	.19
14												.01	.04	.25	.69

Figure B.0.15 – Overlapping matrix for water+toluene.

$\lambda$	0	1	2	3	4	5	6	7	8	9	10	11	12	13	14
0	.50	.37	.10	.02											
1	.29	.38	.23	.08	.02										
2	.08	.21	.33	.26	.10	.03	.01								
3	.02	.07	.24	.34	.22	.09	.02	.01							
4		.02	.13	.31	.29	.16	.07	.02	.01						
5		.01	.06	.22	.29	.20	.12	.06	.03	.01					
6			.02	.12	.21	.21	.17	.12	.08	.04	.02	.01			
7			.01	.04	.11	.14	.16	.16	.15	.11	.09	.04			
8				.01	.03	.06	.09	.13	.17	.17	.19	.14	.02		
9						.01	.03	.06	.11	.16	.26	.30	.06		
10							.01	.02	.05	.11	.25	.43	.13	.01	
11									.01	.05	.17	.48	.27	.02	
12										.01	.05	.29	.48	.15	.01
13												.03	.17	.58	.22
14													.01	.24	.75

Figure B.0.16 – Overlapping matrix for water+phenanthrene.

# APPENDIX C – Work Published in Scientific Conference



## PARAMETRIZAÇÃO E AVALIAÇÃO DO CAMPO DE FORÇA SAFT- $\gamma$ CG PARA SIMULAÇÃO MOLECULAR DE FENANTRENO

Isabela Q. Matos<sup>1</sup>, Charles R. A. Abreu<sup>1\*</sup>

<sup>1</sup> Escola de Química, Universidade Federal do Rio de Janeiro, Rio de Janeiro, RJ, Brasil

\*Autor para correspondência: abreu@eq.uffrj.br

O fenantreno é um hidrocarboneto policíclico aromático que pode ser usado para estudar moléculas mais complexas como os asfaltenos. Portanto, é interessante desenvolver campos de forças para simulação molecular eficientes computacionalmente que consigam descrever esses tipos de molécula. O campo de força SAFT- $\gamma$  CG, escolhido para o estudo, é do tipo *coarse-grained* e foi desenvolvido com base na equação de estado SAFT-VR Mie. Essa equação modela uma substância subdividindo sua estrutura em segmentos que interagem através de potencial de Mie. Os parâmetros desse campo de força para o fenantreno foram estimados e avaliados em relação à determinação de propriedades de equilíbrio líquido-vapor (ELV). A estratégia de estimação possui duas etapas. A primeira consiste em minimizar o erro quadrático entre a pressão de vapor calculada com a equação de estado (EdE) SAFT-VR Mie e os valores experimentais. Os parâmetros dessa minimização foram, então, usados no cálculo de ELV com o método de *Gibbs Ensemble Monte Carlo* com volume total constante (GEMC-NVT). A segunda etapa consistiu em estimar novamente os parâmetros através do método de mínimos quadrados envolvendo a pressão de vapor e a densidade de líquido saturado calculadas por Monte Carlo (MC) e as calculadas com a EdE SAFT-VR Mie. Essa segunda parte é necessária devido a aproximações teóricas que geram diferenças entre os resultados da simulação molecular e da EdE. Esse campo de força apresentou uma boa descrição da pressão de vapor do fenantreno com método de GEMC quando comparado com os dados experimentais. As densidades de líquido e vapor saturados e as propriedades críticas apresentaram resultados similares aos obtidos com o campo de força atômico TraPPE-EH, sendo que o SAFT- $\gamma$  CG exige menor esforço computacional. Para continuação do trabalho, pretende-se usar esses parâmetros para calcular a energia de solvatação do fenantreno, em diluição infinita, em tolueno e em solução tolueno + CO<sub>2</sub> com dinâmica molecular.

Palavras-chave: campo de força, SAFT- $\gamma$  CG, simulação molecular, fenantreno.

### Introdução

Os campos de força do tipo *coarse-grained* parametrizados a partir de propriedades experimentais são uma alternativa aos campos de força desenvolvidos com cálculos *ab initio* quando a escala das simulações moleculares precisa ser aumentada. O método *coarse-grained* consiste, basicamente, em dividir a substância em pseudo-átomos representativos de grupos de átomos. Normalmente, a parametrização do campo de força é feita a partir de informações obtidas em uma escala mais detalhada. Quando as informações utilizadas provêm do comportamento em uma escala maior, a estratégia para o modelo *coarse-grained* é dita ser do tipo *top down*. Um dos campos de força que possuem essa estratégia é o SAFT- $\gamma$  CG (Avendaño *et al.*, 2011), o qual foi desenvolvido com base na equação de estado (EdE) SAFT-VR Mie (Lafitte *et al.*, 2013). Esse modelo usa o potencial de Mie para descrever moléculas formadas por segmentos conectados. A vantagem de usar essa equação como base

para o campo de força é a sua capacidade de descrever bem as propriedades do fluido, incluindo derivadas de segunda ordem, de uma variedade de sistemas (Lafitte *et al.*, 2013). Com base nessas ideias, o presente trabalho teve como objetivo parametrizar o campo de força SAFT- $\gamma$  CG para o fenantreno, cuja estrutura é apresentada na Figura 1, utilizando dados de equilíbrio líquido-vapor e considerando que ele é formado por três segmentos esféricos. O fenantreno foi escolhido como forma de testar a capacidade de representação desse campo de força simplificado, já que sua parametrização para moléculas menores tem sido bem sucedida (Lafitte *et al.*, 2012). Outra razão para o estudo do fenantreno é o fato de ele servir como modelo simplificado para moléculas mais complexas, tais como os asfaltenos, já que possui uma estrutura de anéis policondensados e é solúvel em tolueno.

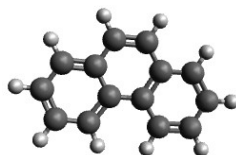


Figura1. Estrutura molecular do fenantreno.

## Metodologia

### *Estimação com a Equação de Estado SAFT-VR Mie*

A Ede SAFT-VR Mie descreve moléculas formadas por segmentos conectados e que interagem através do potencial de Mie, dado por:

$$U_{Mie}(r) = \varepsilon \frac{\lambda_r}{\lambda_r - \lambda_a} \left( \frac{\lambda_r}{\lambda_a} \right)^{\lambda_a/\lambda_r - \lambda_a} \left[ \left( \frac{\sigma}{r} \right)^{\lambda_r} - \left( \frac{\sigma}{r} \right)^{\lambda_a} \right] \quad (1)$$

em que  $\lambda_r$  é o expoente repulsivo,  $\lambda_a$  é o expoente atrativo,  $\sigma$  corresponde à distância entre os centros dos segmentos e  $\varepsilon$  é o parâmetro de energia do segmento. A energia livre de Helmholtz específica para a Ede SAFT-VR Mie para um fluido não-associativo é definida como

$$a = a^{IDEAL} + a^{MONO} + a^{CHAIN}, \quad (2)$$

em que  $a^{IDEAL}$  é a contribuição de gás ideal,  $a^{MONO}$  é contribuição dos monômeros (segmentos desconectados) e  $a^{CHAIN}$  é a contribuição relativa à formação das cadeias de segmentos. Para cadeias que possuem  $m_s$  segmentos do mesmo tipo tangencialmente ligados, a contribuição da cadeia é

$$a^{CHAIN} = -(m_s - 1) \ln g^{Mie}(\sigma), \quad (3)$$

onde  $\ln g^{Mie}(\sigma)$  é o valor da função de distribuição radial de pares para o fluido monomérico de referência (fluido de Mie). Devido à estrutura aromática do fenantreno, usou-se a seguinte expressão para anéis formados por  $m_s$  segmentos no lugar da contribuição de cadeia:

$$a^{RING} = -m_s \ln g^{Mie}(\sigma). \quad (4)$$

Essa substituição é feita porque a diferença entre uma molécula formada por cadeias e uma formada por anéis, tendo ambas o mesmo número de segmentos, é que a última possui uma ligação a mais (Lafitte *et al.*, 2012). Para o equacionamento completo da EdE, o leitor é referido ao artigo de Lafitte *et al.* (2013). Seguindo essa formulação, os parâmetros  $\varepsilon$ ,  $\lambda_r$  e  $\sigma$  foram estimados e os parâmetros  $m_s$  e  $\lambda_a$  foram fixados em 3 e 6, respectivamente. A razão para fixar o número de segmentos em três deve-se à própria estrutura do fenantreno, que consiste em três anéis aromáticos condensados. Já o parâmetro atrativo foi fixado no valor London para facilitar a estimação, já que é comprovada a alta correlação entre os parâmetros repulsivo e atrativo do potencial (Ramrattan *et al.*, 2015). A minimização foi feita através do método PSO (*Particle Swarm Optimization*) e com apenas dados de pressão de vapor, por uma questão de indisponibilidade de dados experimentais de densidade do fenantreno como líquido saturado. A função objetivo possui a seguinte forma:

$$F_{\text{exp}}(\sigma^{SAFT}, \varepsilon^{SAFT}, \lambda_r^{SAFT}) = \sum_{i=1}^{N_p} \left( \frac{P_v^{\text{exp}}(T_i) - P_v^{SAFT}(T_i)}{P_v^{\text{exp}}(T_i)} \right)^2 \quad (5)$$

em que  $N_p$  corresponde ao número de pontos experimentais,  $P_v^{\text{exp}}$  aos pontos de pressão de vapor experimental (Mortimer e Murphy, 1923) e  $P_v^{SAFT}$  à pressão de vapor calculada com a EdE SAFT-VR Mie. Esse cálculo de equilíbrio foi feito usando como base a rotina do ponto de bolha proposta por Smith *et al.* (2007).

#### *Cálculo com o Método “Gibbs Ensemble Monte Carlo” (GEMC)*

Os parâmetros estimados com equação SAFT-VR Mie foram usados para realizar simulações no GEMC (Panagiotopoulos, 1987) com o simulador CASSANDRA (Shah e Maginn, 2011). O método de GEMC foi desenvolvido com o intuito de estudar a coexistência entre fases através da simulação simultânea de duas caixas com condições de contorno periódicas e que trocam moléculas, energia e volume entre si, mas de forma a manter o volume total constante. O equilíbrio entre elas é obtido através de passos de Monte Carlo (MC) que incluem o deslocamento aleatório das moléculas, mudança de volume e transferências aleatórias de moléculas entre as caixas. Para sistemas com apenas um componente, os cálculos são realizados mantendo-se o volume e o número de partículas total constantes (NVT), mas de maneira a permitir a variação de volume ( $V = V^{liq} + V^{vap}$ ) e partículas ( $N = N^{liq} + N^{vap}$ ) dentro de cada caixa. Essas simulações no GEMC-NVT foram feitas inserindo-se aleatoriamente 400 moléculas na caixa líquida e 100 moléculas na caixa vapor. As densidades iniciais das caixas foram escolhidas ajustando-as às densidades obtidas com a EdE SAFT-VR Mie, para evitar que todas as moléculas migrassem para uma única caixa ao longo da simulação. A simulação consistiu em, no mínimo, 10000 ciclos de equilibração e 100000 ciclos de produção, sendo que cada ciclo de MC corresponde a 1000 tentativas de rotação, 1000 de translação, 100 de inserção, 100 de exclusão e 10 de variação de volume. A distância de corte usada foi igual a quatro vezes o valor do diâmetro do segmento estimado e as interações de van der Waals foram calculadas através do potencial Mie com correção de longa distância (*tail correction*). As propriedades densidade de vapor ( $\rho_{vap}$ ), densidade de líquido ( $\rho_{liq}$ ) e pressão ( $P_v^{sim}$ ) foram amostradas a cada 100 ciclos de MC e essas amostragens foram divididas em cinco blocos para os cálculos da média e do desvio padrão. Os resultados

obtidos nessas simulações foram usados para estimar coeficientes de correção para os parâmetros conformacionais do campo de força ( $c_\sigma$  e  $c_\epsilon$ ), que são relacionados aos parâmetros provenientes da EdE SAFT-VR Mie através de parâmetros oriundos de ajuste,

$$\sigma^{ajuste} = c_\sigma \sigma^{SAFT} \quad (6)$$

$$\epsilon^{ajuste} = c_\epsilon \epsilon^{SAFT} \quad (7)$$

Os parâmetros de ajuste são necessários porque as aproximações teóricas feitas na EdE geram discrepâncias entre os resultados da simulação molecular e os da EdE (Lafitte *et al.*, 2012). Por isso, a estimação desses parâmetros foi feita de maneira a diminuir as diferenças entre a pressão de vapor e a densidade de líquido saturado obtidas com a equação de estado e as obtidas via simulação molecular. A função objetivo, minimizada através do método PSO, possuiu a seguinte forma:

$$F_{sim}(c_\sigma, c_\epsilon) = \sum_{i=1}^{N_p} \left( \frac{P_v^{sim}(T_i, \sigma^{SAFT}, \epsilon^{SAFT}) - P_v^{SAFT}(T_i, \sigma^{ajuste}, \epsilon^{ajuste})}{P_v^{sim}(T_i, \sigma^{SAFT}, \epsilon^{SAFT})} \right)^2 + \sum_{i=1}^{N_p} \left( \frac{\rho_{liq}^{sim}(T_i, \sigma^{SAFT}, \epsilon^{SAFT}) - \rho_{liq}^{SAFT}(T_i, \sigma^{ajuste}, \epsilon^{ajuste})}{\rho_{liq}^{sim}(T_i, \sigma^{SAFT}, \epsilon^{SAFT})} \right)^2 \quad (8)$$

Com os parâmetros atrativo e repulsivo fixados nos valores encontrados com a EdE SAFT-VR Mie, o espaço paramétrico pode ser redefinido de maneira a se encontrar um conjunto de parâmetros refinado para o campo de força SAFT- $\gamma$  CG (Lafitte *et al.*, 2012), que são:

$$\sigma^{sim} = \sigma^{SAFT} / c_\sigma \quad (9)$$

$$\epsilon^{sim} = \epsilon^{SAFT} / c_\epsilon \quad (10)$$

As simulações pelo método GEMC-NVT foram refeitas seguindo-se a mesma metodologia e os resultados foram comparados com os dados de referência. A determinação do ponto crítico não foi realizada por meio do método GEMC-NVT, pois ele apresenta grandes flutuações perto do ponto crítico, que fazem as caixas de simulação mudarem de identidade durante a simulação. A temperatura crítica ( $T_c$ ) foi então ajustada através do método PSO com a seguinte equação:

$$(\rho_{liq} - \rho_{vap}) = A(T_c - T)^\eta \quad (11)$$

As densidades de líquido e vapor no equilíbrio na equação acima foram provenientes de simulações feitas em uma faixa de temperatura entre 476,75 e 825 K. O expoente crítico ( $\eta$ ) foi fixado no valor correspondente ao seu valor universal (0,325) (Hansen e McDonald, 2006) e a constante A foi determinada pelo ajuste. A densidade crítica ( $\rho_c$ ) foi obtida através da lei linear dos retângulos (Equação 12) na mesma faixa de temperatura usada para obter  $T_c$ .

$$\frac{(\rho_{liq} - \rho_{vap})}{2} = \rho_c + D(T_c - T) \quad (12)$$



A curva de coexistência líquido-vapor do campo de força SAFT- $\gamma$  CG foi comparada com os resultados disponíveis na literatura para o campo de força TraPPE-EH (Rai e Siepmann, 2013), e as demais propriedades foram avaliadas por comparação com dados experimentais (Mortimer e Murphy, 1923; Nelson e Senseman, 1922; Linstrom e Mallard, 2017). A equação de desvio relativo absoluto médio usada possui a seguinte forma:

$$\Delta X = \frac{1}{N_p} \sum_{i=1}^{N_p} \left| \frac{X_{i^{ref}} - X_{i^{calc}}}{X_{i^{ref}}} \right| 100\%, \quad (13)$$

$X^{ref}$  é o valor da propriedade de referência e  $X^{calc}$  é o valor da propriedade calculado.

## Resultados e Discussão

Os parâmetros do fenantreno com três segmentos para o campo de força SAFT- $\gamma$  CG estimados com a metodologia descrita estão expostos na Tabela 1.

Tabela 1. Parâmetros do campo de força SAFT- $\gamma$  CG para o fenantreno.

$\sigma^{sim} / \text{\AA}$	$(\varepsilon^{sim} / \kappa_b) / \text{K}$	$\lambda_r^{sim}$
4,008	529,646	14,339

A Figura 2 mostra a pressão de vapor do fenantreno em função de temperatura. O campo de força com parâmetros estimados conseguiu apresentar um comportamento similar ao observado nos dados experimentais, considerando a sua simplicidade e eficiência computacional. O valor da pressão de vapor para temperaturas mais próximas do ponto normal de ebulição foi subestimado, enquanto houve uma superestimação dos valores de pressão de vapor para temperaturas mais baixas. Esse mesmo comportamento e o desvio relativo da pressão de vapor, exposto na Tabela 2, foram similares aos resultados observados para os cálculos de propriedades de equilíbrio e transporte do dióxido de carbono e metano com o campo de força SAFT- $\gamma$  CG em trabalhos anteriores (Aimoli *et al.*, 2014; Aimoli, 2015). Observa-se, também, que os resultados obtidos ficaram próximos dos resultados do campo de força TraPPE-EH disponíveis na literatura, o que indica que a simplificação do modelo acarreta somente em pequenos desvios no cálculo da pressão de vapor. O desvio relativo médio está disponível na Tabela 2.

Tabela 2. Desvio relativo médio entre os resultados obtidos com o campo de força SAFT- $\gamma$  CG e os dados experimentais.

	$\Delta / \%$
$P_v$	9,01

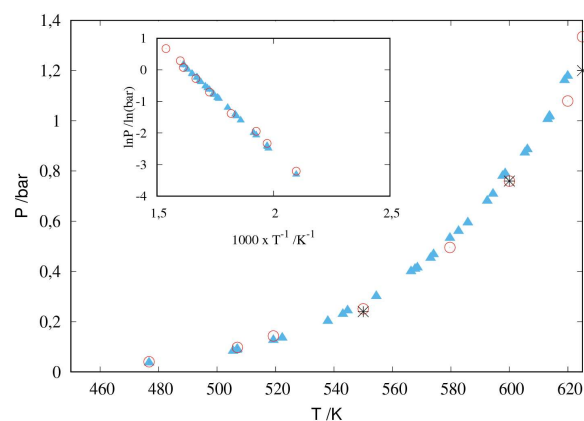


Figura 2. Pressão de vapor em função da temperatura calculada com o campo de força SAFT- $\gamma$  CG (círculos vermelhos), dados experimentais (triângulos azuis) e resultados do campo de força TraPPE-EH (asteriscos pretos). A figura inserida é o mesmo gráfico, porém no formato de Clausius-Clapeyron.

Na Figura 3, as curvas de densidade de líquido e vapor saturados obtidas para o campo de força SAFT- $\gamma$  CG foram comparadas com os dados disponíveis do TraPPE-EH. O campo de força estimado apresentou comportamento razoavelmente similar, mas com discrepâncias maiores do que aquelas observadas para os resultados de pressão de vapor. Adicionalmente, a densidade do fenantreno foi calculada fora do ELV no ensemble NPT-MC a uma temperatura de 298 K e a uma pressão de 1 bar como forma de comparar os resultados com o valor experimental disponível que é igual  $1180 \text{ kg/m}^3$  (Linstrom e Mallard, 2017). O campo de força TraPPE-EH forneceu um valor de densidade igual  $1110 \text{ kg/m}^3$  e o campo de força SAFT- $\gamma$  CG forneceu um valor igual a  $1455 \text{ kg/m}^3$ . Esses resultados mostram que o campo de força SAFT- $\gamma$  CG tem mais dificuldade em prever propriedades em estados diferentes daquele que foi estimado do que o TraPPE-EH por ser um modelo coarse-grained top down. Então, essa diferença na densidade pode ter sido causada pelo uso de apenas a pressão de vapor na estimação dos parâmetros da equação de estado tida como base.

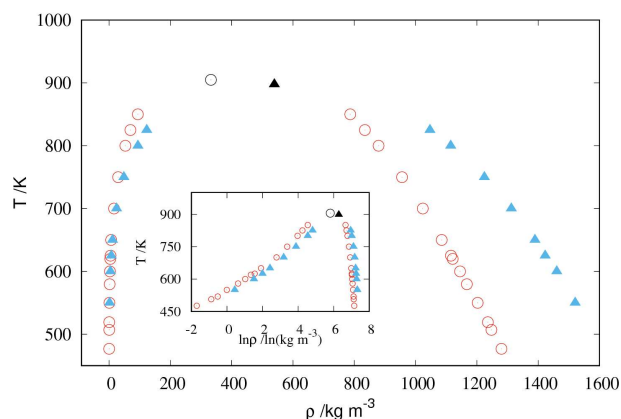


Figura 3. Curva de coexistência líquido vapor calculada com campo de força SAFT- $\gamma$  CG (círculos vermelhos) e com o campo de força TraPPE-EH (triângulos azuis). O círculo e o triângulo pretos representam as propriedades críticas calculadas com o ajuste.

Os desvios relativos da densidade de líquido e de vapor saturados e das propriedades críticas encontradas com o ajuste das Equações 12-13 estão resumidos na Tabela 3. Os desvios deixam clara a existência de uma diferença significativa para densidade no equilíbrio ocasionados pela diferença de rigor teórico entre os modelos. Essas discrepâncias talvez possam ser reduzidas com uso dos dados da densidade do campo de força TraPPE-EH para estimação inicial, o que permitiria um melhor ajuste do expoente atrativo do potencial de Mie. Já com relação à previsão da temperatura crítica, os resultados entre os campos de força foram mais próximos.

Tabela 3. Propriedades críticas e desvios relativos entre o campo de força SAFT- $\gamma$  CG e os dados de referência para o fenantreno.

$\Delta / \%$			
$T_c$	$\rho_c$	$\rho_{liq}$	$\rho_{vap}$
4,08	38,17	21,42	38,64

## Conclusão

O campo de força SAFT- $\gamma$  CG foi obtido para o fenantreno com uma metodologia em que se usa a equação de estado SAFT-VR Mie como base para parametrização desse campo de força. Os parâmetros encontrados foram avaliados através de cálculos das propriedades de equilíbrio com o método GEMC-NVT. Os resultados para pressão de vapor tiveram concordância com os dados experimentais e com o resultados da literatura obtidos para o campo de força atomístico TraPPE-EH. As densidades de líquido e vapor no equilíbrio apresentaram maiores desvios em relação ao TraPPE-EH do que a pressão de vapor. Isso mostra que a simplificação da molécula não representou uma grande perda na representação da pressão de vapor do fenantreno e que esse modelo de campo de força pode ser uma alternativa a modelos atomísticos. Com esse campo de força avaliado, pretende-se fazer cálculos de energia de solvatação do fenantreno em tolueno e em soluções tolueno+CO<sub>2</sub> utilizando-se dinâmica molecular.

## Referências Bibliográficas

- Aimoli, C.G.; Maginn, E.J.; Abreu, C.R.A. Transport properties of carbon dioxide and methane from molecular dynamics simulations. *J. Chem. Phys.*, 141 (2014), 134101.
- Aimoli, C.G. Thermodynamic and Transport Properties of Methane and Carbon Dioxide: A Molecular Simulation Study; D.Sc Thesis, School of Chemical Engineering, University of Campina, 2015.
- Avendaño, C.; Lafitte, T.; Galindo, A.; Adjiman, C.S.; Jackson, G.; Müller, E.A. SAFT- $\gamma$  Force Field for the Simulation of Molecular Fluids. 1. A Single-Site Coarse Grained Model of Carbon Dioxide. *J. Phys. Chem. B*, 115 (2011), 11154–11169.
- Hansen, J.P.; McDonald, I.R. *Theory of Simple Liquids*. Academic Press, Amsterdam, 2006.
- Lafitte, T.; Avendaño, C.; Papaioannou, V.; Galindo, A.; Adjiman, C.S.; Jackson, G.; Müller, E.A. SAFT- $\gamma$  force field for the simulation of molecular fluids: 3. Coarse-grained models of benzene and hetero-group models of n-decylbenzene. *Mol. Phys.*, 110 (2012), 1189–1203.
- Lafitte, T.; Apostolou, A.; Avendaño, C.; Galindo, A.; Adjiman, C.S.; Müller, E.A.; Jackson, G. Accurate statistical associating fluid theory for chain molecules formed from Mie segments. *J. Chem. Phys.*, 139 (2013), 154504.
- Linstrom, P.J.; Mallard, W.G. NIST Chemistry WebBook, NIST Standard Reference Database Number 69. Disponível em: <<http://webbook.nist.gov>>. Acesso em: 12 abr. 2017.
- Panagiotopoulos, A.Z. Direct determination of phase coexistence properties of fluids using Monte Carlo simulation in a new ensemble. *Mol. Phys.*, 61 (1987), 813–826.
- Mortimer, S.M.; Murphy, R.V. The Vapor Pressures of Some Substances Found in Coal Tar. *Ind. Eng. Chem. Res.*, 14 (1923), 1140-1142.
- Nelson, O.A.; Senseman, C.E. Vapor Pressure Determinations on Naphthalene, Anthracene, Phenanthrene, and Anthraquinone between Their Melting and Boiling Points. *J. Ind. Eng. Chem.*, 14 (1922), 58-62.
- Rai, N.; Siepmann, J.I. Transferable potentials for phase equilibria. 10. Explicit-hydrogen description of substituted benzenes and polycyclic aromatic compounds. *J. Phys. Chem. B*, 117 (2013), 273-288.
- Ramrattan, N.; Avendaño, C.; Müller, E.; Galindo, A. A corresponding-states framework for the description of the Mie family of intermolecular potentials. *Mol. Phys.*, 113 (2015), 1–16.
- Shah, J.R.; Maginn, E.J. A general and efficient Monte Carlo method for sampling intramolecular degrees of freedom of branched and cyclic molecules. *J. Chem. Phys.*, 135 (2011), 134121.
- Smith, J.M.; Van Ness, H.C.; Abbot, M. M. *Introdução à Termodinâmica da Engenharia Química*. LTC, Rio de Janeiro, 2007.

# APPENDIX D – Paper for Publication in Scientific Journal